

## **Final Report for ICAT Grant 07-4**

### **Grant Title: Demonstration of Particulate Matter (PM) Sensor in Post-DPF Environment**

Grantee  
Honeywell ACS Laboratories  
12001 Highway 55  
Plymouth, MN 55441

May 5, 2010

“Conducted under a grant by the California Air Resources Board  
of the California Environmental Protection Agency”

“The statements and conclusions in this report are those of the grantee and not necessarily those of the California Air Resources Board. The mention of commercial products, their source, or their use in connection with material reported herein is not to be construed as actual or implied endorsement of such products.”

## **Acknowledgments**

Honeywell would like to acknowledge the following participants in the program:

Professor David Kittelson, Adam Ragatz, Win Watts, and Darrick Zarling of the University of Minnesota. Their engine and particle monitoring expertise provided the backbone of the work on this project.

Greg Hampson, ENSYSENG, provided valuable insight to the PM assessment through his work with the PM sensor data analysis and the development of different analysis techniques.

The members of the PM sensor team, Pete Reutiman, Fouad Nusseibeh, Ryan Becker, and Nick Moelders, for their great effort in gathering information on the PM sensor and making the changes needed to improve the operation of the sensor.

Finally, Honeywell would like to acknowledge Steve Church and Mike McCarthy for their many helpful suggestions during the course of this program.

## Table of Contents

Section	Page
Acknowledgments .....	ii
List of Figures .....	iv
List of Tables .....	vi
List of Acronyms .....	vii
Abstract .....	viii
Executive Summary .....	ix
1. Introduction .....	1
2. Innovative Technology .....	1
3. ICAT Project .....	2
4. Status of the Technology .....	2
4.1 Description of PM Sensor, Electronics, and Signal Processing .....	2
4.1.1 Probe Fabrication and Mechanical Configuration .....	2
4.1.2 Electrical Configuration .....	5
4.1.3 Software and Signal Processing .....	8
4.2 Description of Engine, Aftertreatment Systems, Instrumentation, and Measurement Techniques .....	11
4.2.1 Engine and Exhaust Aftertreatment Systems .....	11
4.2.2 Particle and Mass Concentrations Instrumentation and Calibration .....	12
4.2.2.1 Particle Counters .....	12
4.2.2.2 Particle Size Distribution .....	12
4.2.2.3 Mass Measurement .....	12
4.2.2.4 Electrometer-Based Instruments .....	12
4.2.2.5 Supplemental Emissions Test .....	13
4.2.2.6 Gas Measurement .....	13
4.2.2.7 Calibration and Quality Assurance Procedures of Particle and Mass Concentrations Instrumentation .....	14
4.2.3 Calibration of On-Engine Experimental Setup using Particle and Mass Concentration Instrumentation .....	19
4.2.3.1 Post DPF in Steady State Speed and Constant Load .....	19
4.2.3.2 Post DPF in Steady State and Transient Speed While Under Constant Load .....	22
4.2.3.3 Using Bypass Configuration in Steady State Speed and Constant Load .....	23
4.2.3.4 DPF Failure Mechanisms and Experimental Simulation .....	27
4.3 On-Engine PM Sensor Measurements, Analysis and Results .....	32
4.3.1 Experimental issues during on-engine PM Sensor Testing .....	32
4.3.1.1 Deere Dynamometer Failure and Change to Isuzu Engine and Dynamometer .....	33
4.3.1.2 Vibration-Induced and Ground-Coupled Noise .....	33
4.3.2 In Pre- and Post-DPF Configuration Under Functional DPF Conditions .....	35
4.3.3 In Bypass Configuration .....	36
4.3.4 In Post-DPF Configuration Under Failing DPF Conditions .....	41
4.3.4.1 Results of DPF Failure Testing .....	41
4.3.4.2 Charge Measurements .....	42
4.3.5 Summary of Advanced Frequency Analysis of PM Sensor Data for OBD Diagnostics .....	47
4.4 Conclusions .....	48
4.4.1 Recommendations and Next Steps .....	50
4.5 Commercialization .....	51
5. Appendix .....	52
5.1.1 Summary of Advanced Frequency Analysis of PM Sensor Data for OBD Diagnostics .....	52
5.1.2 Test Data Overview .....	52
5.1.3 PM Signal Overview .....	52
5.1.3.1 Downstream/Post-DPF Sensor .....	53
References and Notes .....	70

## List of Figures

Figure	Page
2-1 (a) PM sensor (left) (b) Sensor installed in the pre-DPF environment (right) .....	1
4-1 Shielded version of PM sensor .....	3
4-2 New shielding configuration for PM sensor probe .....	4
4-3 PM sensor with associated electronics .....	4
4-4 Output signal from testing the original system using controlled input source .....	5
4-5 First- and second-stage electronics block diagram .....	6
4-6 Probe with separated preamplifier .....	6
4-7 Complete hardware system, including the PM sensor .....	7
4-8 Output signal from system testing using controlled input source .....	7
4-9 PM sensor processing electronics .....	8
4-10 Data logging schematic for probes using new and old amplifier boxes .....	8
4-11 Software interface for raw data collection of four PM sensors simultaneously .....	9
4-12 Processed data part of the software interface .....	10
4-13 User interface FFT window .....	10
4-14 (a) Unprocessed and (b) processed data from an engine run at 1400 RPM and 350 Nm load ....	11
4-15 Sampling system schematic showing location of PM sensors upstream and downstream of DPF .....	15
4-16 Comparison of the SMPS and ELPI using 100 ppm polydisperse DOS aerosol. Error bars are standard deviations. ....	15
4-17 DOS aerosol size distribution used for the CPC vs. electrometer comparison prior to passage through the DMA column .....	16
4-18 Instrument performance with DOS aerosol concentration $< 10^4$ part/cm <sup>3</sup> and with larger particles .....	17
4-19 Instrument performance with DOS aerosol concentration $> 10^4$ part/cm <sup>3</sup> and with larger particles .....	17
4-20 Electrometer current distribution by stage for the DLP .....	18
4-21 Number size distributions from the SMPS and EEPS .....	22
4-22 EEPS, AVL, and Honeywell PM sensor response during engine speed ramp conducted at constant 250 Nm torque .....	23
4-23 Backpressure testing schematic .....	24
4-24 Instrumentation configuration for downstream sampling .....	25
4-25 Test engine, DPF configuration with bypass, and PM sensor locations .....	25
4-26 SMPS and EEPS size distributions for varying levels of bypass valve opening .....	26
4-27 Mass concentration as a function of bypass of valve opening .....	27
4-28 Brake-specific mass emissions as a function of bypass of valve opening .....	27
4-29 Thermal separation .....	28
4-30 Ring cracking failure .....	28
4-31 Small and large end cap cracking for catastrophic failure .....	29
4-32 Flow path in Donaldson DPF .....	30
4-33 Drilling holes .....	31
4-34 Hole patterns .....	31
4-35 1800 milled holes .....	32
4-36 Mass concentration .....	33
4-37 Accelerometer and Honeywell sensor response with Kistler charge amp at 1400 RPM and 50 Nm .....	34
4-38 Honeywell sensor suspended in exhaust .....	35
4-39 Mass concentration for bypass exhaust vs. upstream of DPF .....	35
4-40 Comparison of PM sensor output signal from sequential frequency data .....	36
4-41 PM sensor response compared to mass concentration .....	37
4-42 Sensor response compared to OBD levels .....	38
4-43 Comparison of initial charge measurements with PM sensor output .....	39
4-44 Average mass concentration as a function of bypass opening .....	40
4-45 PM sensor response downstream of DPF for different loading conditions .....	40

4-46	PM sensor and mass concentration during bypass operation.....	41
4-47	Brake-specific mass concentration as a function of DPF failure degree .....	42
4-48	Charge fraction.....	43
4-49	Net charge for both bypass and DPF measurements.....	44
4-50	Initial comparison of mass concentration with DPF failure mode .....	45
4-51	Comparison of PM sensor with bypass opening.....	45
4-52	PM sensor response with OBD concentration .....	46
4-53	Indication of PM sensor response change using different engine .....	47
5-1	Sensor configuration relative to DPF for Isuzu engine .....	53
5-2	PM signal (ch4 #40) for 900 holes 10-8-09 with 1x, 2x, 3x ECF wave overlay including reference lines at 0.265 (green) and -0.285 (pink). .....	53
5-3	Histogram of the probability (y axis) of a particular voltage from Ch4 – post-DPF sensor 10-8-09 900 holes. Note the “discrete” rather than continuous nature of the probability distribution.....	54
5-4	Side-by-side comparison of the post-DPF PM sensor signal and the synthesized cosine function with 1x,2x, 3x ECF wave. ....	55
5-5	Spectral analysis of the PM sensor signal downstream of the DPF.....	55
5-6	Cumulative spectral energy graph: post-DPF 10-8-09, 900 holes PM sensor (red), synthesized function (blue) .....	56
5-7	Engine-out PM signal (Ch3 Probe 40) 900 holes .....	57
5-8	Voltage probability distribution for Ch3 Probe 40 - pre-DPF, 900 holes.....	57
5-9	Frequency spectrum pre-DPF, Ch3 Probe 40 900 holes.....	58
5-10	Cumulative Spectral Energy pre-DPF, Ch3 Probe 40 900 holes, 10-8-09 .....	58
5-11	Direct comparison of the pre-DPF (red) Ch3 and post-DPF (blue) Ch4 for 900 holes, 10-8-09. The reference signal with only 1xECF is shown in yellow. ....	59
5-12	Side-by-side comparison with zoom of Ch4-Probe 405 post-DPF sensor and Ch3-Probe 40 pre-DPF sensor for 900 holes.....	59
5-13	Zoomed in overlay of Ch3 (pre-DPF, red) on Ch4 (post-DPF, black) showing the wider distribution of the pre-DPF sensor and the higher probability of lower deviation (large bars close to zero).....	60
5-14	FFT for Ch4 downstream—intervals 2 and 3.....	60
5-15	FFT for Ch3 upstream—intervals 2 and 3.....	61
5-16	Comparison of ensemble-smoothed FFTs for Ch3 and Ch4 (intervals 2 and 3) with engine cycle frequency and its multiples (green).....	61
5-17	Spectral energy for pre-DPF and post-DPF spectra.....	62
5-18	Cumulative Deviation vs. time for the post-DPF sensor—900 holes, Ch3 .....	63
5-19	Comparison of Cumulative Deviation for the pre-DPF sensor (red) and the post-DPF sensor (blue) .....	64
5-20	Spectral energy for pre-DPF and post-DPF spectra of the ensemble averages .....	65
5-21	For 1800 hole case: time trace of upstream (Ch3 blue) and downstream (Ch4 orange) with synthesized function (yellow) .....	66
5-22	For 1800 hole case: Cumulative Deviation pre-DPF slope (red/orange 49.9) is differentiable from post-DPF slope (blue 35.4).....	67
5-23	Frequency spectrum for two intervals of the post-DPF sensor trace, each 4 sec .....	67
5-24	Frequency spectrum for two intervals of the pre-DPF sensor trace, each 4 sec.....	68
5-25	Direct comparison of ensemble-averaged post-DPF (blue) and pre-DPF (red) spectra with synthesized ECF function (green spikes) .....	68
5-26	Direct comparison ensemble-averaged post-DPF (blue), pre-DPF (red), and synthesized ECF (green) spectral energy.....	69
5-27	Sensor configuration—Deere Engine 9/24/09 (only post-DPF sensors shown).....	69
5-28	Time trace of sensor #40, for 300 hole DPF failure test .....	70
5-29	Cumulative deviation showing slope of 132.4 volts per second for sensor #40, for 300 hole DPF failure test .....	70
5-30	Probability distribution for time trace, sensor #40.....	71
5-31	Spectral distribution showing lowest frequency harmonics at 1x, 2x, 3x ECF for sensor #40 for 300 hole DPF failure test .....	71
5-32	Spectral energy distribution: strong staircase steps evident at 1x, 3x, 4x, 5x, 6x ECF .....	71

## List of Tables

Table	Page
4-1 Engine conditions and summary dilution tunnel data.....	20
4-2 Estimates of mass obtained from the SMPS, EEPS, AVL, and filter samples.....	20
4-3 Particle number and length data obtained from the SMPS, EEPS, and EAD.....	20
4-4 Volume concentrations calculated from SMPS and EEPS size distributions .....	21

## List of Acronyms

ACS – Automation and Controls Solutions  
A/D – Analog to Digital  
ARB – Air Research Board  
AVL – Particle Mass Monitor, manufactured by AVL LIST  
CARB – California Air Research Board  
CPC – Condensation particle counters  
DMA – Differential Mobility Analyzer  
DOC – Diesel Oxidation Catalyst  
DOE – Department of Energy  
DOS – Dioctyl Sebacate  
DPF – Diesel Particulate Filter  
DR – Dilution Ratio  
EAD – Electrical Aerosol Detector  
ECF – engine cycle frequency  
EEPS – Engine Exhaust Particle Sizer  
ELPI – Electrical Low Pressure Impactor  
EPA – Environmental Protection Agency  
GUI – Graphical User Interface  
FFT – Fast Fourier Transform  
HEPA – High-Efficiency Particulate Air  
HD OBD – Heavy-Duty OnBoard Diagnostics  
ICAT – Innovative Clean Air Technologies  
NO – Nitric Oxide  
NO<sub>x</sub> – Oxides of Nitrogen  
NSAM – Nanoparticle Surface Area Monitor  
OBD – OnBoard Diagnostics  
OEM – Original Equipment Manufacturer  
PM – Particulate Mass/Matter  
PSL – Polystyrene Latex  
RMS – Root Mean Square  
RPM – Revolution per Minute  
USB – Universal Serial Bus  
ULSD – Ultra-Low Sulfur Diesel  
U of M – University of Minnesota  
SET – Supplemental Emissions Test  
SMPS – Scanning Mobility Particle Sizer  
TL – Transfer Line  
TSI – Thermal Systems, Inc.

## **Abstract**

The use of after-treatment and engine control systems for diesel engines to achieve low emissions has created a need for functional measurement systems to verify correct operational performance during vehicle operation and to provide an unambiguous indication if onboard diagnostic (OBD) levels are exceeded.

The purpose of this program was to reconfigure the Honeywell particulate mass (PM) sensor concept from its previous configuration as a sensor for measuring the particle concentration directly out of the engine, to a mass concentration sensor for operation in the post-diesel particulate filter (DPF) environment of a diesel engine's aftertreatment system. Under the California Air Resources Board (CARB)-sponsored Innovative Clean Air Technologies (ICAT) Grant program, Honeywell tested and demonstrated the operation of the PM sensor in the post-DPF environment and assessed its ability to detect low particle concentrations downstream of the DPF. A key goal of the program was to determine if the particulate matter (PM) sensor could measure particulate matter levels below the OBD threshold of 0.03 g/bhp-hr. Particle and charge measurements in the post-DPF environment were conducted during this program to correlate with the response of the PM sensor.

The PM sensor was found to detect particle mass concentrations at levels below 0.03 g/bhp-hr. The sensor was also shown to withstand the harsh conditions in this environment, such as high temperature. However, intrinsic vibration of the exhaust system during operation of the diesel engine was found to affect the sensor response and limit the signal-to-noise ratio of the sensor's output, thus minimizing the effectiveness of a single sensor directly downstream of the DPF.

Data analysis indicates that modifications to the signal processing algorithm may improve the detection of a DPF failure either if a single PM sensor is used in conjunction with other engine parameters or if a second PM sensor is used to measure the mass concentration upstream of the DPF.



## Executive Summary

OBD requirements state that original equipment manufacturers (OEMs) of diesel engines must ensure that the emission control system is functioning properly and that failure in the system can be detected prior to the actual emissions levels exceeding the OBD threshold. For the 2013 model year, the interim PM threshold for a malfunctioning DPF is set at 5x the certification standard of 0.01 g/bhp-hr or 0.05 g/bhp-hr. The purpose of the multiplier is to avoid false positives and to account for variation in vehicles as well as some deterioration of the system over time. However, the interim multiplier on PM at 5x is very high compared to typical NO<sub>x</sub> thresholds for other emission controls, which are 2x to 3x. Further, the Air Resources Board (ARB) heavy-duty on-board diagnostic (HD OBD) regulation has established a final PM threshold of 0.03 g/bhp-hr (or 3x) to begin phase-in on the 2013 model year and to apply to all heavy-duty engines in the 2016 model year. Currently, indirect-pressure-differential-sensor-based OBD algorithms are the best monitoring technology available, but there is significant concern that this technology will be insufficient to reach the final thresholds. A direct PM measurement by a PM sensor would be a more definitive way to accomplish DPF monitoring for OBD compliance and is one of the technologies cited by ARB as a likely way to meet the final thresholds.

Without a new direct sensing technology such as the PM sensor proposed in this project, particulate matter exhaust emissions for any one vehicle will be difficult to assess, which limits ARB's confidence that vehicles in operation are not only compliant but also as clean as desired. The intent of the PM sensor program was to validate the feasibility of direct measurement of the PM levels in the exhaust systems of diesel engines at the levels anticipated for both healthy and malfunctioning DPFs.

The PM sensor is an electrically isolated probe installed in the engine's exhaust system. Measurements were made in the post-DPF environment with both a functioning and a malfunctioning DPF. During the tests, particle and charge concentrations were also measured, along with engine parameters, to determine how particle charge correlates with output of the PM sensor. Since the PM sensor uses charge induction to obtain a response to the exhaust particles, the measurement of very small currents is required. This in turn imposes stringent specifications and performance requirements on the sensor's preamplifiers. Electronic signal conditioning was used to reduce noise impacts due to engine and exhaust system vibrations and electronic parasitic effects.

Testing was conducted on-engine at the University of Minnesota (U of M) throughout the program. Part of this testing involved simulating progressive failure levels of a DPF while measuring PM sensor response downstream of the DPF. Simulated failure was conducted by drilling out a specific number of end caps (e.g., 100, 300).

A functional DPF was installed in the exhaust system of one of the U of M's diesel engines along with a series of PM sensors and calibrated laboratory instrumentation. Measurements were taken to ensure that the DPF was functioning properly and to provide correlation of the laboratory instrumentation with the particle mass concentration in the exhaust. The test results provided an initial look at the sensitivity of the PM sensor under low particle load conditions.

In addition, the PM sensor was installed on a heavy-duty diesel truck exhaust system and driven on-road for one week to assess the sensor's mechanical ability to withstand realistic environmental conditions. No effects due to mechanical degradation were found during the post-test assessment. The on-road test only evaluated the mechanical integrity of the sensor. As there was no option to place the sensor in the post-DPF environment, the sensor was mounted in an engine-out location.

Once the sensor baseline was established with the functional DPF in the test cell, and prior to destructive modification of the DPF, testing was done to establish whether the PM sensor could respond over the range of particle concentrations corresponding with the OBD limits. This stage of testing proceeded using a variable bypass exhaust system in parallel with the DPF. Tests were conducted over a range of bypass conditions, and the PM sensor signal response indicated detection of low particulate matter concentration levels with good correlation to both particle mass and charge concentration measurements made with the laboratory instrumentation.

Testing was then conducted to simulate a failed DPF by drilling sections of holes into the channel ends at the downstream face of the DPF. The number of sections was progressively increased to emulate higher degrees of degradation. With each subsequent test, the number of holes drilled was determined based on the ability of the laboratory instrumentation to measure a change from the previous test. Initially, the mass and PM sensor response measured an orderly increase in response. During the middle stages of the testing, however, the engine-dyno system itself experienced a catastrophic failure. This necessitated both changing engine types and making modifications to the exhaust system.

With the new engine and exhaust connected to the DPF test system, the new engine operational mode was noticeably different from the initial test engine while maintaining the same particle mass concentration output as seen for the previous engine. With the same particle mass concentration entering the DPF, a similar particle size distribution, and a comparable charge concentration, testing continued by increasing the number of failed sections to the DPF. On the new platform, the PM sensor signal response did not behave as expected. In fact, the sensor had a reduced signal response to an increasing mass concentration. At this point, the sensor and the system were evaluated to determine the root cause for this changed response. Vibration analysis indicated a difference in the vibration frequency spectrum between engines. Root cause of the changed PM sensor response is still undetermined, although it is believed that the modified vibration spectrum may play a significant role.

The goal of demonstrating a PM sensor with accurate correlation to the particle mass concentration downstream of a DPF system was not achieved during this program. Temporal (time-based) and spectral (frequency-based) analysis of the PM sensor data in both pre-DPF and post-DPF positions have indicated significant unknown factors that affect the PM sensor reading. The inability to resolve these issues precludes a comprehensive calibration for the PM sensor output with the measured particulate matter input. Indications are that calibrating a single PM sensor to provide a sensor reading correlated directly to absolute PM levels remains very challenging, and significant effort would be required to incorporate into a calibration equation all the known and unknown factors that influence the charge-based reading of the PM sensor.

A potential solution resides with utilization of two PM sensors to make a differential measurement of particulate matter levels upstream and downstream of a DPF. By using two sensors, a “DPF effectiveness” can be determined by subtraction or division of the post-DPF signal and the pre-DPF signal. This approach has a reasonable chance of accommodating the many possible changes in the PM signal that might be encountered. Both sensors would be exposed to effects of particular engine or operation conditions. Comparison of the two sensors’ outputs would eliminate effects outside of the DPF itself. In this case, the pre-DPF signal then acts as a floating reference. Two methods for relative comparison are presented in this report: one time-based and the other frequency-based. Preliminary analysis suggests both methods may be promising for providing a quantitative measure of DPF. The post-DPF sensor signal can be qualitatively and quantitatively distinguished from the pre-DPF sensor signal, and thus a relative PM sensor approach holds promise as an OBD sensor solution for detecting DPF failures.

## 1. Introduction

Honeywell proposed to conduct a demonstration proving the viability of using our particulate mass (PM) sensor in the post-DPF environment under actual engine conditions to discern between a functioning and a malfunctioning DPF. This technology is anticipated to provide CARB with confidence that PM emissions control systems of 2010+ certified heavy-duty on-road diesel vehicles are functioning as intended. This technology will serve as one element of California's meeting its clean air targets and could prove important for the ARB in evaluating the effectiveness of the OBD criteria for meeting emissions targets in all 2013 vehicles on the road.

The deliverables for this program include the data generated from the measurements made on-engine during testing and a final report based on the analysis of this testing of the PM sensor in the post-DPF environment for use in an OBD monitor of the DPF.

This report is the final element of ICAT grant 07-4, which was to provide a demonstration of a PM sensor with capabilities of sensing mass concentration downstream of a DPF filter and thus a determination of the state of the DPF.

## 2. Innovative Technology

The intent of the PM sensor demonstration program was to reconfigure the particulate mass sensor concept for operation in the post-DPF environment of the after-treatment system for diesel engines. The sensor had been utilized in the exhaust downstream of the engine and in the environment between a DOC and DPF. This environment proved to have too much variation in signal for an accurate determination of the particle mass in the exhaust stream. For this project, the sensor was to have the capability of determining particle mass concentration in the post-DPF environment and of detecting the failure of the DPF to maintain the OBD criteria for emissions. Since particle characteristics in this environment are only somewhat understood, and since the detection mechanism of the PM sensor requires a better understanding of the charge nature of these particles to be developed, Honeywell was to evaluate these sensors in this application. One variation of the PM sensor is shown in Figure 2-1a. Figure 2-1b shows an installation of the sensor in the pre-DPF environment.



**Figure 2-1. (a) PM sensor (left) (b) Sensor installed in the pre-DPF environment (right)**

The PM sensor operates under the basic premise of measuring the charge on particles inherent from the combustion process in the cylinder. The combustion process has been shown to electrically charge particulate effluents.<sup>1,2</sup> It has also been shown that these charges are representative of mass of particulates in the exhaust stream<sup>3,4</sup> and can create a signal in the PM sensor that is related to the mass of carbon particles in the exhaust stream. The PM sensor has

been tested on-engine upstream of the DPF, and the test results indicate that the sensor has a proportional response to DPF loading rate. This proportionality was determined by weighing the loaded DPFs to determine the amount of soot collected. Subsequent analysis of the data indicates that an accuracy of about 10% can be achieved with the PM sensor.

The challenges for this program were to show that the PM sensor, which has demonstrated the capability of particulate mass detection in the pre-DPF environment for DPF loading, will function at the low particle mass levels found in the post-DPF environment and that the sensor is capable of also indicating when the PM level exceeds the OBD threshold.

### **3. ICAT Project**

The intent of the project was to demonstrate that the Honeywell PM sensor will be able to detect particle mass concentrations at the output of a failing DPF down to the limit of 0.03 g/bhp-hr. The initial plan was to modify the sensor, electronics, and signal processing system that was used for detecting the mass concentration in the raw engine exhaust and provide a system that would be sensitive enough to be used downstream of the DPF to provide an OBD signal determining DPF failure. Measurements were also to be made on the actual mass and charge concentrations to verify that the sensor was actually responding to particulate material that was passing through the DPF. During these measurements, a quantification of failure of the DPF was to be done and compared to the PM sensor signal to show signal changes at each step of failure.

The project has actually reduced the noise in the PM sensor response but has not shown that a single sensor in the post-DPF environment can effectively determine DPF failure.

### **4. Status of the Technology**

Based on the testing conducted, the sensor does have the capability of functioning in the harsh exhaust environment, and the probe appears to have reasonable lifetime; however, a single sensor technology does not yet appear ready for installation into a production diesel exhaust aftertreatment system. The results of the project have led to recommendations on how this technology could be utilized for OBD detection, but further testing is needed to resolve the vibration issues and the change in PM sensor levels when changing to a different engine.

#### **4.1 Description of PM Sensor, Electronics, and Signal Processing**

##### ***4.1.1 Probe Fabrication and Mechanical Configuration***

To prepare for PM testing in the OBD environment, new probes were fabricated under a Honeywell program prior to the start of the CARB project. The probes were configured to have a grounded electrically insulating shell around the exposed portion of the probe for improved shielding from noise. The final PM sensor design used in the project is shown in Figure 4-1.



**Figure 4-1. Shielded version of PM sensor**

Once the assembly of the probes was completed, they were evaluated to determine the correct operating performance of the probe. The probes had been previously tested on-engine (as indicated in Figure 2-1b) and were found to provide an appropriate signal level, but were rather noisy when used upstream of an exhaust treatment system. Since the testing environment in the exhaust has high temperatures and the probe itself has a low thermal conductivity, the length of the cabling connecting the probe to the amplifier electronics was dimensioned to prevent the high exhaust temperatures from reaching the electronics; however, the operation of the initial on-engine probes experienced a large vibration signal during engine operation as well as other noise pick-up from the environment. The vibration was found to induce electronic noise in the cable due to a piezoelectric effect. In addition, spurious electric field noise was induced from charged objects approaching the cable.

During subsequent testing, a different shielding method was conceived and adapted for the PM sensor that was presumed to provide a much reduced noise level in the signal (see Figure 4-2). This adaptation was fabricated and tested on-engine for noise response. Initial testing seemed to indicate that the improved shielding and shorter connection length reduced the noise substantially. The PM sensor system with the probe and amplification electronics is shown in Figure 4-3.

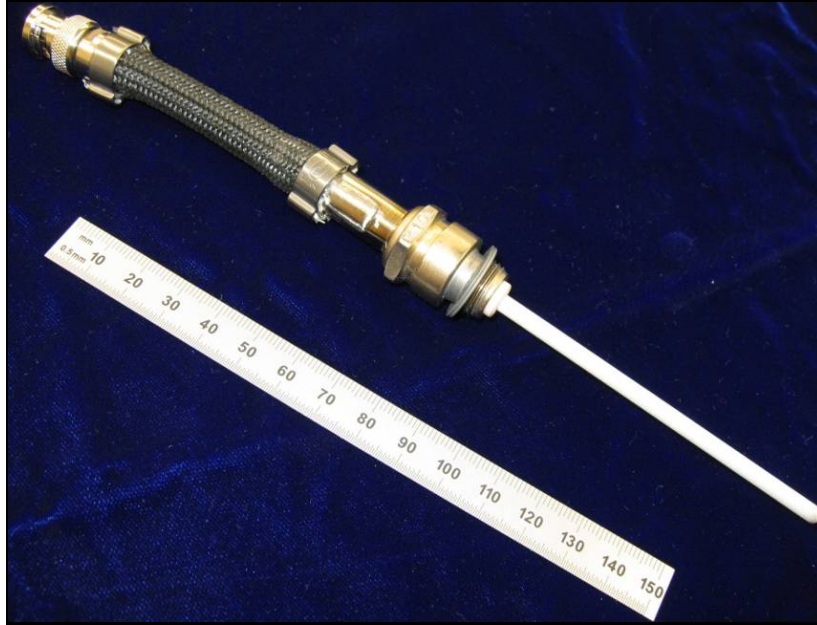


**Figure 4-2. New shielding configuration for PM sensor probe**



**Figure 4-3. PM sensor with associated electronics**

Tests for probe response and electronics were conducted using a non-engine laboratory setup. The tests evaluated the conductivity of the probe, the gross integrity of the outer shielding layer, and the operation of the associated electronics.

The new PM sensor probes were also tested for uniformity of coating to ensure that electrical characteristics would be similar among the probes within a fabrication category. This testing was done to determine the optimum electrical isolation coating thickness on the probe, which was established at 0.002 to 0.004 in.



### 4.1.2 Electrical Configuration

Charge concentrations generated by the combustion process in a diesel engine are very small; these charges are usually located on the carbon exhaust particulates mainly in the accumulation mode. As the charges pass by the PM sensor, they induce an electric field, which is picked up by the sensor. This very small signal requires a very high-gain, low-noise amplifier, and in addition, the front end of the system must be highly shielded. This will allow measuring these low-level signals in such a harsh noise environment.

The original electronics used with the PM sensor were designed for a much larger signal from the charge concentrations present in the pre-DPF location. Thus, the earlier probes were not as extensively shielded and were not found to be sensitive enough for the post-DPF application. Figure 4-4 shows the output response of the system with an input signal of 200 pA at 5Hz. Because of the system's low sensitivity and lack of shielding, the output signal shown has an excessive level of noise and most of that noise is at 60 Hz. A new amplification system was designed to improve the sensitivity and performance of the sensor used for engine testing in this project.

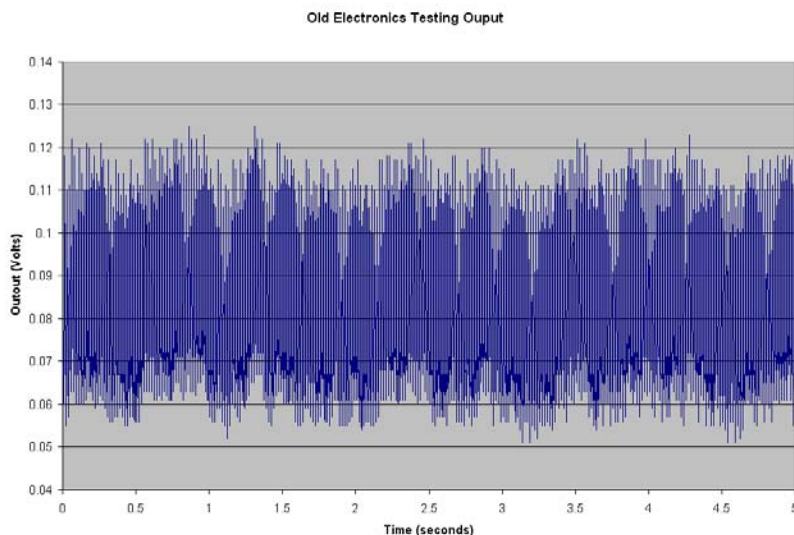


**Figure 4-4. Output signal from testing the original system using controlled input source**

Figure 4-5 shows the block diagram for the electronic circuits. For conducting the laboratory tests, two sensors were connected to a single microcontroller. This allowed easier comparison of the data taken from these two sensors. The system is divided into two stages: a first stage or front end, which is physically small in size (the preamplifier shown in Figure 4-6 is about 1-1/2 in. x 1-1/2 in. x 1/2 in.) and close to the sensor, and a second stage or back end, which is larger and needs to be located away from the exhaust system and the engine vibrations. The first stage/front end consists of a very-high-gain, low-noise charge amplifier and a voltage amplifier with DC restoration to eliminate any DC drift. Since the signal/charge from the sensor is very small, the charge amplifier will be located as close as possible to the sensor to maximize the charge collection. Also, by minimizing the cable length, the noise pickup by the sensor cable will be reduced as well. An issue arises since the short cable minimizes noise but also allows more heat to conduct to the electronics package.

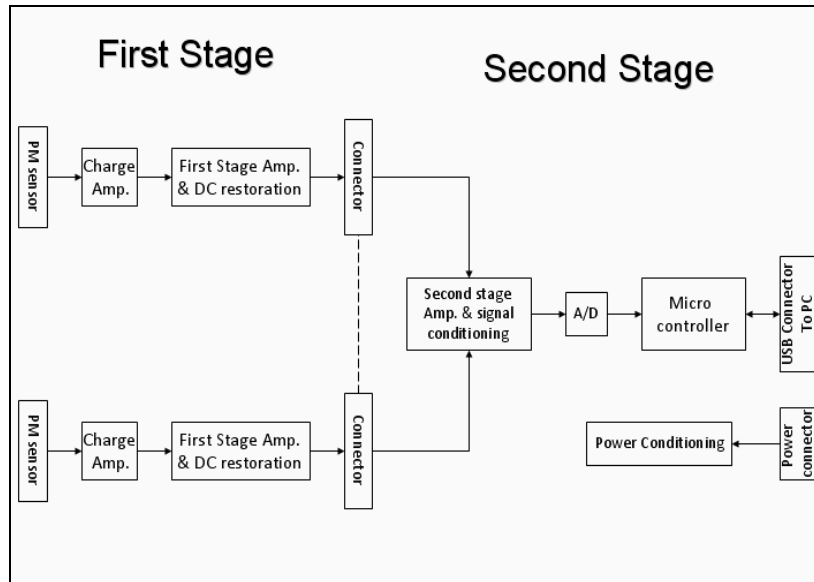


**Figure 4-5. First- and second-stage electronics block diagram**

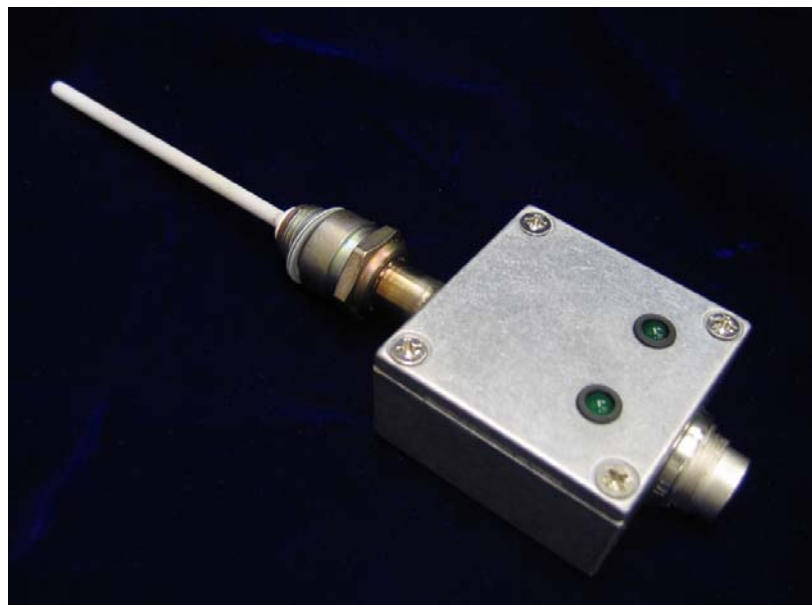


**Figure 4-6. Probe with separated preamplifier**

The second stage is connected to the first by a long cable, to locate it away from the exhaust and sensor. Because of the hardware size, it is difficult to mechanically support the second stage box while it is close to the exhaust system. Placing the second stage close to the data collecting PC is more practical, and will make it easier to operate.

In the second stage the signal is conditioned, that is, amplified and level shifted, digitized using a 16-bit A/D converter, and then sent to a personal computer (PC) through a universal serial bus (USB) connection for data recording and processing. Each second stage unit is capable of collecting and processing data from two sensors simultaneously.



The complete hardware, probe, and electronics are shown in Figure 4-7. To determine the appropriate amplifier gains, the system was tested with a controlled signal from a function generator. Figure 4-8 shows the output response for an input signal of 200 pA at 5 Hz.

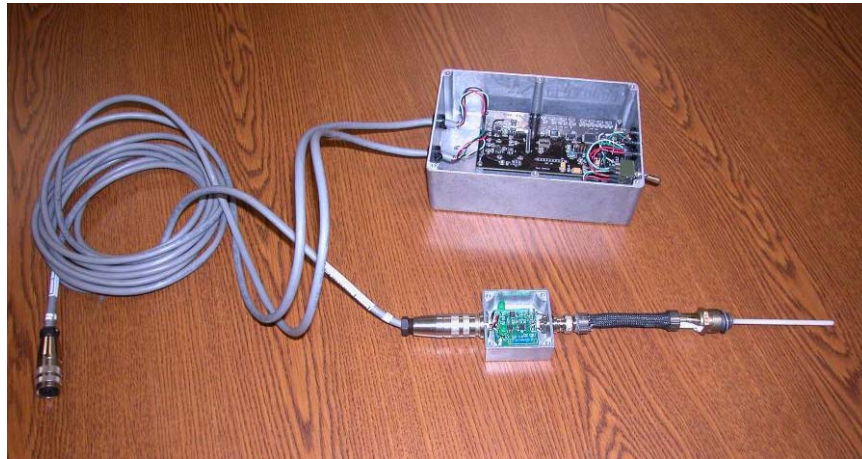


**Figure 4-7. Complete hardware system, including the PM sensor**

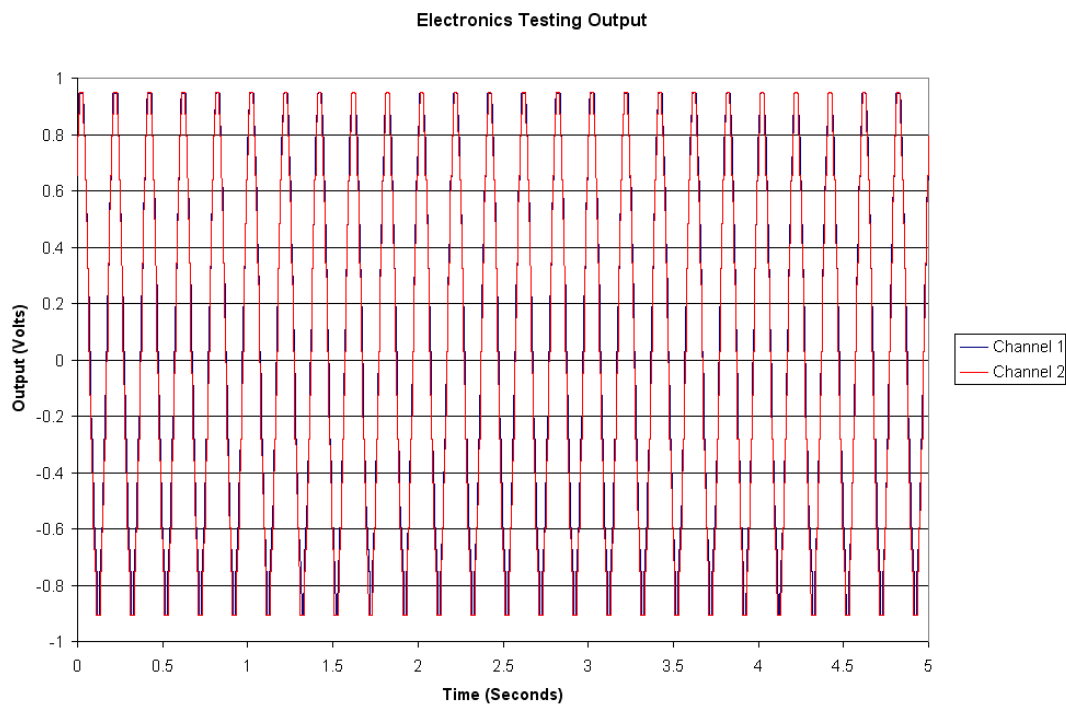


**Figure 4-8. Output signal from system testing using controlled input source**

Four front end amplifiers were built and tested to allow for collecting data from four PM sensors at four exhaust locations simultaneously. The system was installed on the engine at the University of Minnesota and tested. The test included the maximum and minimum engine load and speed conditions, and the amplifier gains were adjusted to accommodate the engine output dynamic range. The complete schematic for signal processing is shown in Figure 4-9. The connections between the probe, electronics, A/D converters, and computer are shown in Figure 4-10.

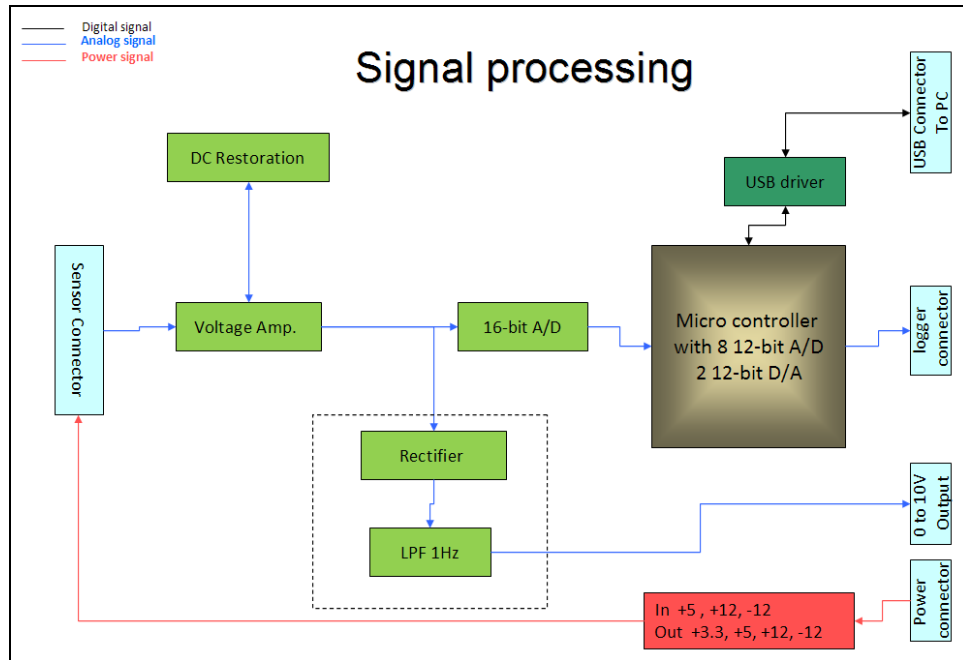


Figure 4-9. PM sensor processing electronics

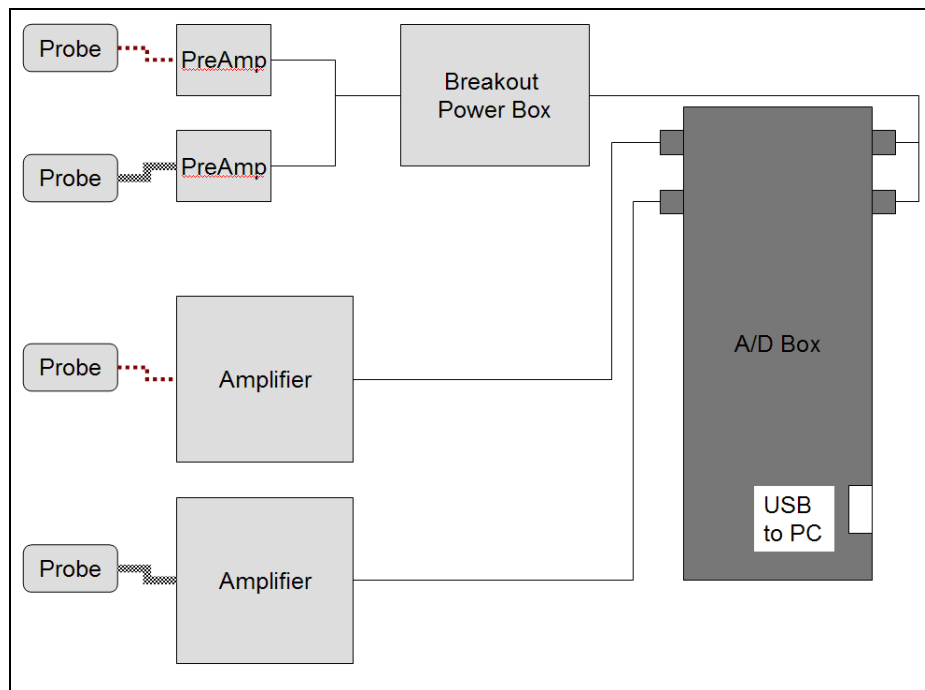


Figure 4-10. Data logging schematic for probes using new and old amplifier boxes

### 4.1.3 Software and Signal Processing

Original signal extraction for the PM sensor, when placed in the engine-out environment, was based on using a 20 – 50 Hz window in the frequency domain of the sensor. This band was initially chosen to provide a rapid method of processing to allow the very fast time response of the sensor to be utilized. The frequency range was also selected to keep the signal being processed above the DC signal levels and also to avoid the 60 Hz ground loop noise. Using

this technique, good correlation was seen between the sensor signal and the mass concentration; but there were still, what was considered then, minor noise problems.

When the sensor was targeted for the post-DPF environment, the signal-noise issue with the sensor became more pronounced. It was felt that to improve on the signal-to-noise ratio when the sensor was placed in the post-DPF environment, both electronics and signal processing modifications had to be made. Initially, the frequency domain was widened from about 2 Hz up to around 200 Hz. At this time, only signal conditioning over a 1 second period was conducted for comparison with the mass concentration. When the signal-to-noise ratio was still found to be large, additional noise and vibration measurements were made that provided insight into the noise found in the sensor signal. These tests are described in section 4.3.1.2.

To control the data collection on the PM sensor, a graphical user interface (GUI) was developed for the LabView™ package collecting the data. The GUI included run control and some signal processing to reduce the noise and the file size of the data collected. The raw data is usually collected at 1000 samples/sec. Preprocessing the data on the fly will help in the final data analysis through reduction in processing time. This eventually will be made part of the hardware electronics interfacing with the PM sensor.

Figure 4-11 shows the “Raw Data” tab of the GUI. The raw data are plotted in real time for four PM sensors simultaneously; this allows monitoring any changes in the data or engine status. The data can also be saved for further analysis and comparison with previous or future runs and different running conditions.

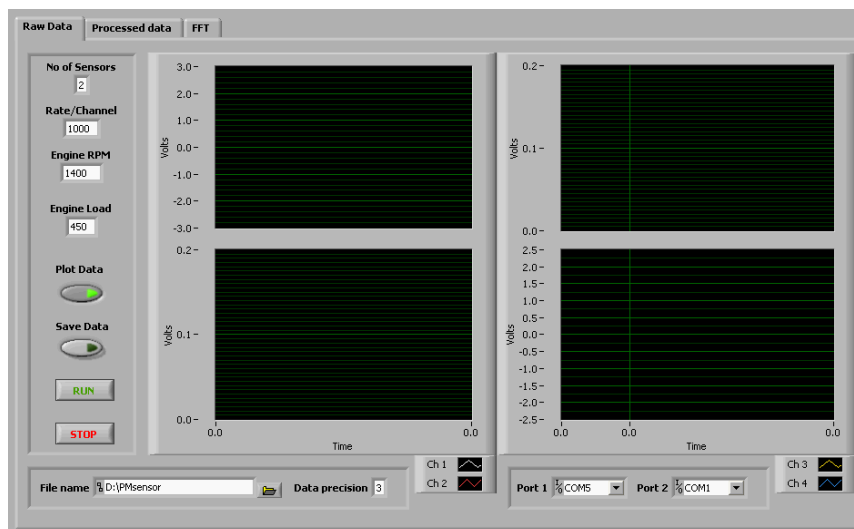


**Figure 4-11. Software interface for raw data collection of four PM sensors simultaneously**

The “Processed data” tab, which is shown in Figure 4-12, shows the control and plots of the processed data of the same four sensors. The user also has the option of filtering the signal, reducing the noise effect.

Finally, the user can monitor the frequency components for the same four sensors in the “FFT” tab, shown in Figure 4-13. This helps understand the sensor response by correlating the engine RPM to the strength of different frequencies in the signal.

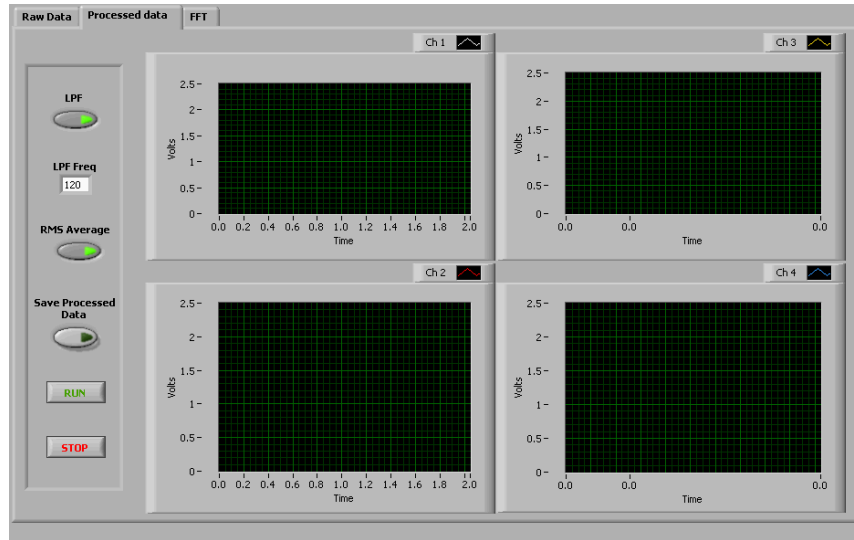


**Figure 4-12. Processed data part of the software interface**

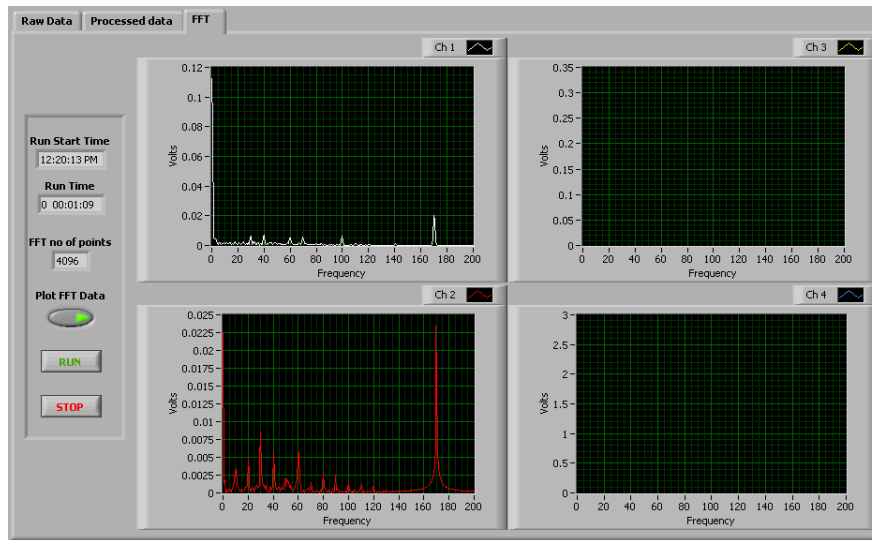


**Figure 4-13. User interface FFT window**

The first step in processing the signal is removing the DC component. This is done in the hardware through the DC restoration circuit. In the software, the signal is rectified to be all positive signals. A low-pass filter, if needed, can be activated to remove any high-frequency components above a selected undesired frequency in the signal. Finally, the root mean square (RMS) of the signal is calculated and plotted and/or saved to a file at a rate of 1 sample/sec, significantly reducing the size of the data files.

Figure 4-14(a) and Figure 4-14 (b) show an example of an unprocessed and a processed signal for one of the engine runs. The data clearly shows the benefit of pre-processing the signal, which helps to reduce the size of the data files for storage and final analysis of the PM sensor response. Different time scales are presented to indicate the differences in both the short duration variance and the longer time scale variance of the signal.

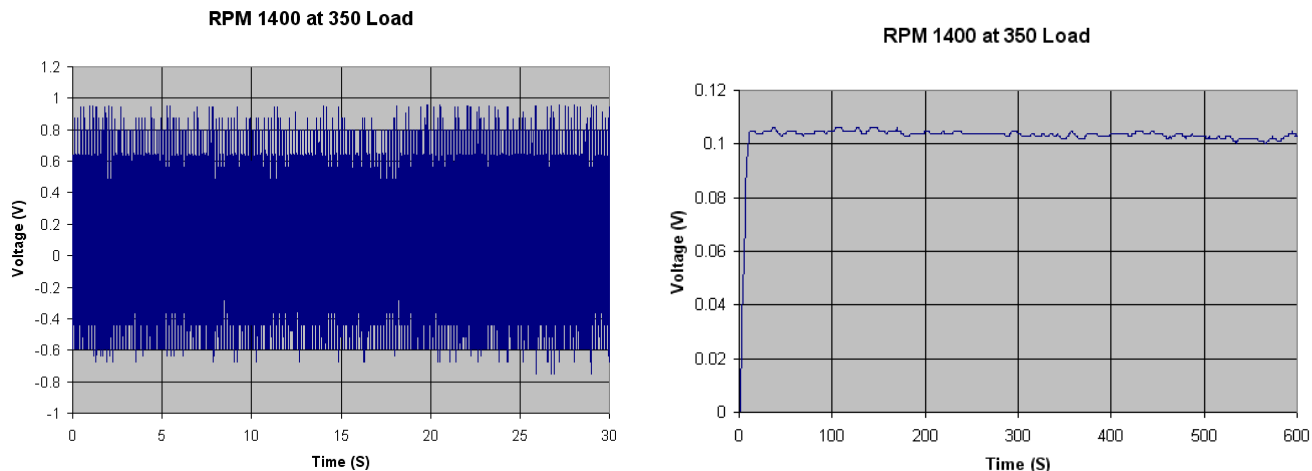


**Figure 4-14. (a) Unprocessed and (b) processed data from an engine run at 1400 RPM and 350 Nm load**

## **4.2 Description of Engine, Aftertreatment Systems, Instrumentation, and Measurement Techniques**

The following sections of this report describe in detail the on-engine experimental setups and calibration procedures used to establish repeatable and reproducible experimental conditions for the following PM sensor measurements.

### **4.2.1 Engine and Exhaust Aftertreatment Systems**

The first test engine was a 4-cylinder, 4.5-L, 129-kW (173 hp) at 2400 RPM, model year 2005 Deere 4045H. The engine was turbocharged, aftercooled with common rail fuel injection, and had EPA tier 2 approval for off-highway applications. Exhaust gas recirculation was not set up on this engine. The API-CJ-4 engine oil was recommended for use with exhaust filtration devices. The oil was broken-in for about 10 hr at various engine load and speed conditions. The engine was equipped with a Donaldson crankcase filtration system and filtered crankcase fumes were vented to the atmosphere rather than introduced back into the engine. The engine was fueled with ultra-low (6 ppm S) sulfur diesel (ULSD) fuel and operated on an Eddy current dynamometer test stand.

The second test engine was a 4-cylinder 5.2-L, 142-kW (190 hp) at 2600 RPM, model year 2005 Isuzu 4HK1-TC. The engine was turbocharged, aftercooled with common rail fuel injection, and meets EPA requirements for model year 2004 heavy-duty truck engines for on-road applications. Exhaust gas recirculation was connected and controlled by the stock engine control module. API-CJ-4 engine oil was used and broken in for approximately 10 hr before testing began. The engine was fueled with ultra-low sulfur diesel purchased from a local gas station.

Honeywell supplied one new Donaldson catalyzed filter (part # 226355-016-190; 26.7 x 35.6 cm). It was used with an existing Donaldson style 3 aftertreatment system that included a catalyzed pre-filter (part # P229063) and two end cones. The new filter replaced a similar filter that had been used by the U of M for another project. The exhaust filtration system was modular in design and allowed for swapping in and out of the individual sections.

## **4.2.2 Particle and Mass Concentrations Instrumentation and Calibration**

### **4.2.2.1 Particle Counters**

Condensation particle counters (CPCs) are used to determine the aerosol particle number concentration (part/cm<sup>3</sup>). A Thermal Systems, Inc. TSI 3025A and 3010 butanol-based CPCs were used during this investigation. They differ primarily in the particle size range counted and the upper limit concentration. The 3025A covers the range from 2.5 nm to 1000 nm in diameter up to a concentration of 10<sup>5</sup> part/cm<sup>3</sup>. The 3010 CPC covers the range of 10 nm to 1000 nm in diameter up to a concentration of 10<sup>4</sup> part/cm<sup>3</sup>. Either instrument can be used with the scanning mobility particle sizer discussed below. The principle of operation is that condensation of a liquid such as butanol on particles grows them to an optically detectable size by an optical particle counter.

### **4.2.2.2 Particle Size Distribution**

Aerosol size distributions were determined using a TSI Scanning Mobility Particle Sizer (SMPS™), a TSI 3090 Engine Exhaust Particle Sizer (EEPS™), and a Dekati Electrical Low Pressure Impactor (ELPI™). The SMPS consists of a control platform, a long column Differential Mobility Analyzer (DMA), and a 3025A Condensation Particle Counter (CPC). The SMPS is configured to size particles from about 8 nm to 300 nm with a response time of 90 sec, and the CPC is operated in the high-flow mode. The EEPS sizes particles from 5.6 to 560 nm with a 1-sec response time and a 10-L/min flow rate. Both the EEPS and SMPS classify particle size using electrical mobility, but the SMPS counts particles using the CPC while the EEPS uses a series of electrometers to determine the size distribution. The ELPI combines three technologies to determine the aerosol size distribution. Aerosol enters the ELPI at 10 L/min, passing by a unipolar corona charger prior to entering a 12-stage cascade impactor. The size distribution is determined either by an array of electrometers or by gravimetric analysis of the individual impaction stage substrates and final filter. Normally, particles are sized from 30 nm to 10 µm, but inclusion of the filter stage in place of stage 12 lowers the particle size range to 7 nm. Electrometer response time is < 5 sec.

### **4.2.2.3 Mass Measurement**

Mass measurement was done using an AVL Micro Soot Sensor, Model 483, that relies on the photoacoustic measurement method. Diesel exhaust contains strongly absorbing soot particulates that are exposed to modulated light. The periodical warming and cooling of the black carbon particles and the resulting expansion and contraction of the carrier gas results in a sound wave that is detected by means of microphones. The AVL sensor has a range of detection from 1 µg/m<sup>3</sup> to < 50 mg/m<sup>3</sup> ± 10 µg/m<sup>3</sup> with a drift of 10 µg/m<sup>3</sup>/hr of operation. Data are subjected to 1-sec smoothing prior to being recorded. The AVL sensor has its own dilutor capable of about 20:1 dilution.

### **4.2.2.4 Electrometer-Based Instruments**

The TSI model 3068A Aerosol Electrometer is designed to measure the net charge on aerosol particles in the size range of 2 nm to 5 µm. It consists of a current sensor, an absolute filter mounted on a Teflon insulator within a metal housing, and a solid state electrometer operational amplifier. The current sensor collects particles in the sampled air by the process of filtration, charges on the particles are measured, and the net electrical current is displayed in picoamperes. This instrument has not been previously used to evaluate the net particle charge in past Honeywell soot sensor studies conducted at the U of M. This instrument was used heavily during the instrument comparison portion of the project.

In prior studies of the soot sensor, the TSI Model 3070A Electrical Aerosol Detector (EAD) was used to measure the total aerosol length (mm/cm<sup>3</sup>) concentration of exhaust aerosol. Aerosol

length can be thought of as number concentration times average diameter, or simply as  $d_1$  weighting. This measurement falls between number concentration ( $d_0$ ) and surface area ( $d_2$ ). Particles are measured in the size range of 10 nm to 1.0  $\mu\text{m}$  over a wide range of concentration (0.01  $\text{mm}/\text{cm}^3$  to  $2.5 \times 10^3 \text{ mm}/\text{cm}^3$  or 0.002 pA to 400 pA). For monodisperse, 50-nm particles, this range corresponds to  $2 \times 10^2$  to  $5 \times 10^7 \text{ part}/\text{cm}^3$ .

The operating principle of the Model 3070A Electrical Aerosol Detector is based on diffusion charging of sampled particles, followed by detection of the aerosol using an electrometer. Aerosol enters the instrument at 2.5 L/min. The flow is split, with 1 L/min passing through a filter and an ionizer and 1.5 L/min being measured as aerosol flow. The flows are recombined in a mixing chamber where aerosol particles are charged by diffusion. The charged aerosol passes through an ion trap to remove excess ions. The aerosol then moves on to an aerosol electrometer for charge measurement. In the electrometer, current is passed from the particles to a conductive filter and measured by a very sensitive amplifier. A microprocessor controls the instrument flows and measures various operational parameters. The display is updated once per second and outputs are updated as fast as 3.75 times per second. With the diffusion charger and ion trap turned off, the instrument acts as an electrometer and can determine total net charge on the particles. This is the configuration used in the current investigation. The EAD was used during the instrument comparison portion of the project and during transient studies.

The working principle of the TSI Model 3550 Nanoparticle Surface Area Monitor (NSAM) is similar to the EAD but measures nanoparticle surface area ( $\mu\text{m}^2/\text{cm}^3$ ). Similar to the EAD, the operating principle of the NSAM is based on diffusion charging of sampled particles followed by detection of the aerosol using an electrometer. Aerosol enters the instrument at 2.5 L/min. The flow is split, with 1 L/min passing through a filter and an ionizer and 1.5 L/min being measured as aerosol flow. The flows are recombined in a mixing chamber where aerosol particles are charged by diffusion. The charged aerosol passes through a trap to remove excess ions and the desired amount of small particles. The voltage applied to the trap determines the amount of particles removed along with the ions. The aerosol then moves on to an aerosol electrometer for charge measurement. In the electrometer, current is passed from the particles to a conductive filter and measured by a very sensitive amplifier. The dynamic range of the instrument is 0 to 10,000  $\mu\text{m}^2/\text{cm}^3$ . It is sensitive to particles as small as 10 nm, and data are collected every second. With the diffusion charger and ion trap turned off, the instrument acts as an electrometer and can determine total net charge on the particles. This was the configuration used in the current investigation. For purposes of this investigation, the EAD and NSAM are interchangeable. The NSAM was used during the instrument comparison portion of the project.

#### **4.2.2.5 Supplemental Emissions Test**

Progress was made on the preparation for conducting the Supplemental Emissions Test (SET), which involves 13 steady state test conditions. A modified SET test was being prepared that would not include the full load condition because of limitations of the dynamometer and engine configurations. The test would have required a repeatable transient ramp from one condition to the next over a 20-sec period. The engine was configured to have the throttle controlled by the LabView data acquisition software. This SET testing with the PM sensors was not completed during this study.

#### **4.2.2.6 Gas Measurement**

The total dilution ratio (DR) was determined by measuring the raw exhaust NO concentration and the NO concentration in the diluted sample. NO was used due to previous experience with dilution instrumentation and the availability of instrumentation to the project. Raw exhaust was transferred to a CAI gas analyzer using a heated line. Dilute NO measurements were made with

a Horiba CLA-510SS. The gas analyzers were zeroed and spanned daily to ensure an accurate measurement.

#### **4.2.2.7 Calibration and Quality Assurance Procedures of Particle and Mass Concentrations Instrumentation**

The quality assurance procedures were developed during previous projects<sup>5</sup> funded by the Coordinating Research Council<sup>6</sup> and DOE.<sup>7</sup> These procedures are summarized below.

In the past, compressed air used for dilution and cooling of the exhaust has been dried and filtered for particulate matter prior to making aerosol measurements. Since the condition of the compressed air is especially important when measuring low aerosol number and mass concentrations, as might be expected after a DPF, a Donaldson pressure swing adsorption system that has been designed to provide high-purity compressed air was used by the U of M during these measurements. This system dries the air stream, removing particles and organic material by sequential passage of the dilution air stream through driers, filters, and scrubbers.

The particle instrumentation described above was first evaluated using an atomized solution of dioctyl sebacate and isopropyl alcohol. This polydisperse aerosol was then dried using a charcoal diffusion drier and diluted with cleaned compressed air before being distributed to the instruments for comparison. Engine testing was not conducted until all instrumentation showed satisfactory results during this comparison. In some cases, this meant rigorous cleaning or replacement of fouled components.

During engine testing, a HEPA filter was used at the beginning of each test to ensure that the system was leak free. Gas analyzers were zeroed and spanned at the beginning of each test to ensure proper reading and compensate for small day-to-day variations.

**Dilution and Sampling System**—Measurements were made using a two-stage ejector dilutor system. This system is similar to those described previously<sup>8</sup> and extensively evaluated during the Coordinating Research Council (CRC) E-43 project.<sup>9</sup> Exhaust enters the system through a 2-cm-long, 0.25-cm-diameter stainless sampling probe immersed in the exhaust flow, and passes through a short section (6.35 cm) of stainless steel tubing referred to as the transfer line (TL). An Air-Vac TD 260-air ejector pump with a critical flow orifice provided the first stage of dilution. The system was designed to give a primary DR ranging from 5 to 25:1 with a regulated, total dilute exhaust mixture flow rate of 100 L/min. It was critical that the orifice not be allowed to plug with soot as this increases the DR and affects the resulting measurements. Ultra-clean compressed air was provided by the Donaldson system. Diluted aerosol then passed into a water-jacketed residence time chamber with internal flow distribution cone. The chamber was designed for a residence time of 1 sec at 100 L/min. Residence time chamber temperature was kept at  $47 \pm 5$  °C.

Pressure and temperatures were measured in the residence time chamber as well as in the exhaust. Temperature in the chamber was measured using a type K thermocouple. After the residence time, chamber secondary dilution took place using another TD 110 air ejector. Figure 4-15 is a schematic of the entire sampling system with instrumentation. Note that the TL is not shown in the schematic to illustrate the point that the tunnel may be placed up- or downstream of the exhaust filtration system.



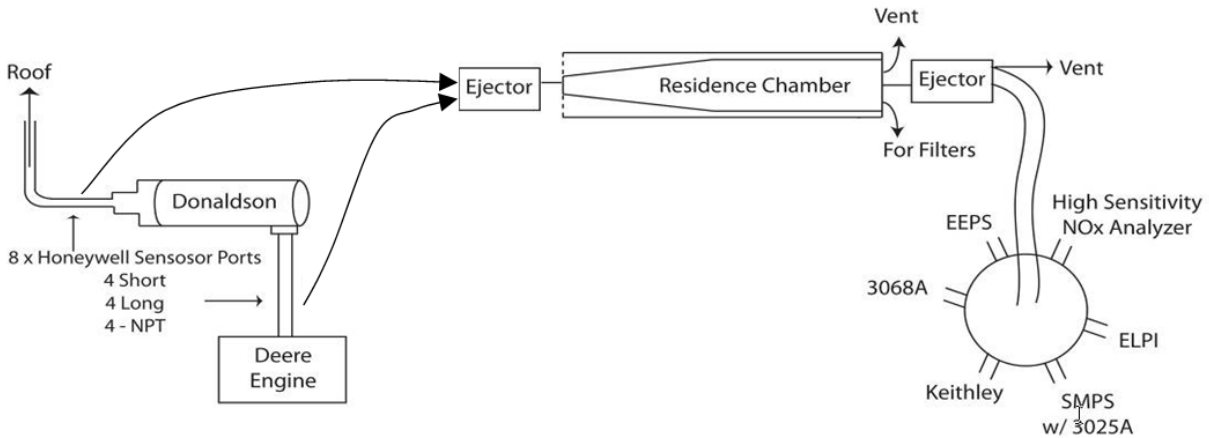


**Figure 4-15. Sampling system schematic showing location of PM sensors upstream and downstream of DPF**

A series of tests was conducted using dioctyl sebacate (DOS) aerosol to evaluate the performance of the particle sizing and aerosol instruments with electrometers. In the first test, 100 ppm DOS diluted in isopropyl alcohol was aerosolized using the nebulizer and distributed to the ELPI and SMPS using a sampling manifold to determine how the ELPI and SMPS size distributions compared. The test was conducted after sequential cleanings of the ELPI with organic solvents to ensure optimal performance. Figure 4-16 shows the results of the comparison, and the agreement is excellent.

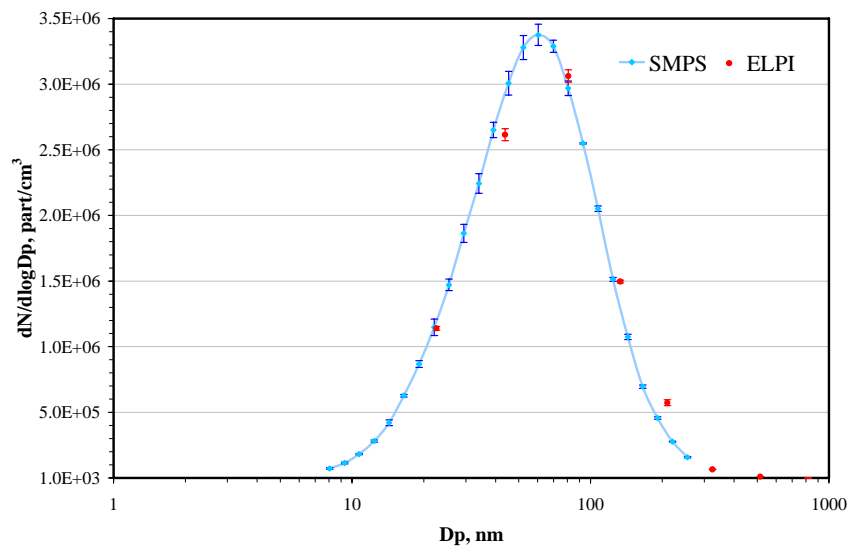


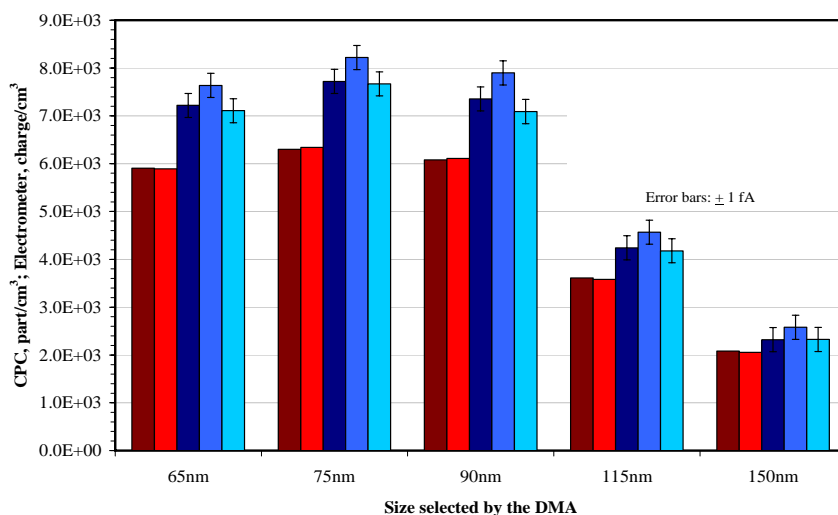
**Figure 4-16. Comparison of the SMPS and ELPI using 100 ppm polydisperse DOS aerosol. Error bars are standard deviations.**

A second series of tests was conducted using 100 ppm DOS aerosol to evaluate the performance of the electrometer-based instruments. In these tests the performance of the 3025A and 3010 CPCs were compared, and the performance of the 3068A, EAD, and NSAM were compared. The DOS aerosol was passed through a differential mobility analyzer (DMA), and by controlling the voltage placed on the DMA column a given particle size was selected. In this case, tests were conducted to measure the charge on a predetermined range of particle sizes (65, 75, 90, 115, and 150 nm). Nearly all of the particles leaving the DMA were found to have either a +1 or -1 net charge. (As particles become larger, more particles will be multiple

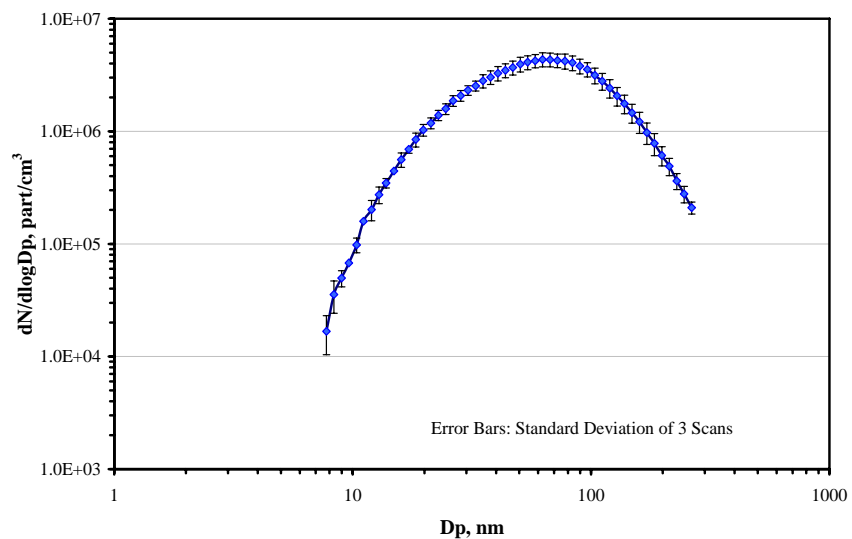
charges.) A similar procedure was used to calibrate the CPCs, but rather than use a polydisperse aerosol like DOS, polystyrene latex (PSL) monodisperse aerosol was used to minimize the number of particles with multiple charges. In the first test, the aerosol was diluted using ultra-pure dilution air and the DR was determined by the 3010 CPC's upper limit of  $10^4$  part/cm<sup>3</sup>. In the second test, a lower dilution ratio was used to increase the particle number concentration and optimize the performance of the NSAM, EAD, and 3068A electrometers.

Figure 4-17 shows the DOS aerosol size distribution that was used prior to neutralization and passage through the DMA column. Figure 4-18 shows the instrument performance when the particle number concentration was  $< 10^4$  part/cm<sup>3</sup>.

For all sizes in Figure 4-18, the particle number concentration agreement between the two CPCs was excellent. Electrometer agreement was also very good. A repeat of the test at higher particle number concentration confirmed the initial result and is shown in Figure 4-19. In addition to a higher concentration of particles, the DMA was used to select larger particles, thus reducing the number of multiply charged particles. Any multiply charged particles that make it through the DMA are counted as one particle in the CPC and as multiple particles in the electrometer, resulting in a higher reading from the electrometer. In this test, the ELPI was included because the concentrations were sufficiently high to allow the ELPI electrometer measurements to be meaningful with the charger turned off. In this configuration, the ELPI was used as a size-selective electrometer. The total current registered by the ELPI is shown in Figure 4-20. The NSAM was excluded because of its overall similarity to the EAD.



**Figure 4-17. DOS aerosol size distribution used for the CPC vs. electrometer comparison prior to passage through the DMA column**



**Figure 4-18. Instrument performance with DOS aerosol concentration  $< 10^4$  part/cm<sup>3</sup> and with larger particles**

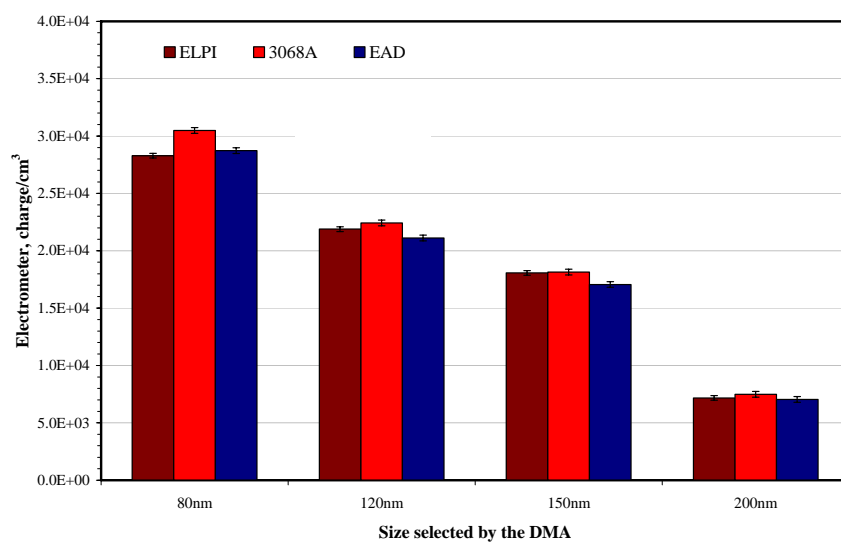


**Figure 4-19. Instrument performance with DOS aerosol concentration  $> 10^4$  part/cm<sup>3</sup> and with larger particles**

Figure 4-20 shows the electrometer current distributions measured by each stage of the ELPI for the 80-, 120-, 150-, 200-, and 317-nm particles with the charger off.

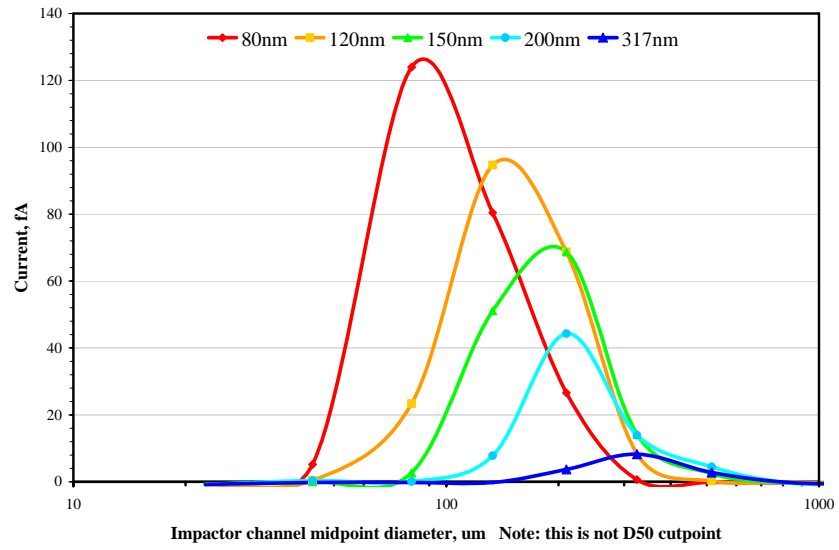


**Figure 4-20. Electrometer current distribution by stage for the DLP**

### **4.2.3 Calibration of On-Engine Experimental Setup using Particle and Mass Concentration Instrumentation**

To provide the information to relate the PM sensor signal to mass concentration, baseline testing was needed using the engine exhaust. Of the instrumentation that was calibrated, the SMPS and the EEPS were continued to track alongside the AVL instrument. This still allowed the evaluation of the exhaust particle distributions for size and also could provide a check on the AVL during the testing. The key correlation for the PM sensor was ultimately a comparison to the mass concentration provided by the AVL instrumentation.

The continued use of the SMPS and EEPS equipment was also needed since measurements were being conducted both for charge as a function of particle size as well as the total charge of the exhaust.

The complete experimental setup then contained measurement points upstream of the DPF system, a DPF that could be modified to simulate different failure levels, and a bypass configuration for the initial determination that the PM sensors can respond to much lower concentrations. From past experimentation, the sensor has only been exposed to full exhaust levels at different engine operating modes. It was necessary to also determine how the sensor would respond to different exhaust concentrations during the same engine operation mode. It was felt that a bypass system would provide this information more easily than repeated failing of several DPFs.

Once the bypass testing had provided information on the viability of the PM sensor under lower particle concentrations, the DPF failure testing could proceed.

#### **4.2.3.1 Post DPF in Steady State Speed and Constant Load**

The initial series of tests was conducted in the pre-DPF environment to provide the correlation information between the particle instrumentation and the mass concentration. In addition, PM testing was done initially to assess the response of the initial preamp system to higher concentrations and as a precursor to achieving a more sensitive preamplifier. During these tests, particulate matter data was collected upstream of the DPF using the SMPS, EEPS, and EAD. The dilution ratio for this was determined through gas measurements. Table 4-1 shows the engine conditions, averages, and standard deviations for dilution tunnel parameters, including the raw and diluted NO concentrations, the dilution ratios, and the tunnel temperatures for each engine condition. Each condition was preceded by a 15-min stabilization period before sampling began.

Estimated mass data from the EEPS, SMPS, and AVL are shown in Table 4-2. AVL data were collected for the conditions shown but were collected during a different time period than the SMPS and EEPS data. In addition, gravimetric data collected during another project for some of the same engine conditions are also shown. Particle number concentration data calculated from the SMPS and EEPS, along with length data from the EAD, are shown in Table 4-3. Table 4-4 shows the calculated SMPS and EEPS volume data.

**Table 4-1. Engine conditions and summary dilution tunnel data**

Condition	Raw NO, ppm		Dilute NO, ppm		Dilution ratio		Tunnel temp, C	
	Avg	Std	Avg	Std	Avg	Std	Avg	Std
1400 RPM 450 Nm	705	2.5	2.88	0.04	245	3.93	47.3	0.16
1400 RPM 250 Nm	503	2.3	2.21	0.03	228	2.36	47.5	0.12
1400 RPM 100 Nm	290	1.0	1.31	0.01	221	1.39	47.4	0.15
1400 RPM 50 Nm	210	1.1	0.96	0.01	220	2.57	47.4	0.45
2400 RPM 450 Nm	434	2.1	1.95	0.01	222	1.64	47.0	0.16
2400 RPM 250 Nm	303	2.1	1.33	0.01	227	1.95	47.2	0.13
2400 RPM 100 Nm	188	0.7	0.83	0.01	226	1.95	47.2	0.18
2400 RPM 50 Nm	250	1.5	1.16	0.01	215	1.69	47.1	0.42
1000 RPM 250 Nm	854	2.6	3.60	0.02	237	1.39	47.0	0.15
1000 RPM 100 Nm	331	2.2	1.46	0.01	227	1.62	47.8	0.27
1000 RPM 50 Nm	250	1.5	1.16	0.01	215	1.69	47.1	0.42

**Table 4-2. Estimates of mass obtained from the SMPS, EEPS, AVL, and filter samples<sup>10</sup>**

Condition	SMPS, mg/m <sup>3</sup>		EEPS, mg/m <sup>3</sup>		AVL, mg/m <sup>3</sup>		NIOSH filter, mg/m <sup>3</sup>	
	Avg	Std	Avg	Std	Avg	Std	Avg	Std
1400 RPM 450 Nm	13.28	1.13	11.08	0.53	18.18	1.16	17.26	1.52
1400 RPM 250 Nm	11.50	1.12	8.84	0.29	10.79	0.59	10.55	1.17
1400 RPM 100 Nm	10.27	0.98	8.13	0.22	8.45	0.36	5.57	1.52
1400 RPM 50 Nm	4.78	0.56	3.66	0.12	3.58	0.19	3.24	0.5
2400 RPM 100 Nm	22.64	1.19	15.93	0.35	16.05	0.55		
2400 RPM 50 Nm	10.56	0.75	7.58	0.18	6.16	0.21		
1000 RPM 250 Nm	10.23	0.98	9.64	0.44	11.84	0.64		
1000 RPM 100 Nm	17.69	1.23	15.18	0.51	18.67	1.01		
1000 RPM 50 Nm	5.91	0.66	4.74	0.19	5.26	0.35		

**Table 4-3. Particle number and length data obtained from the SMPS, EEPS, and EAD**

Condition	SMPS, part/cm <sup>3</sup>		EEPS, part/cm <sup>3</sup>		EAD, mm/cm <sup>3</sup>	
	Avg	Std	Avg	Std	Avg	Std
1400 RPM 450 Nm	3.53E+07	3.07E+06	3.66E+07	2.00E+04	431	14.8
1400 RPM 250 Nm	3.85E+07	2.94E+06	3.85E+07	8.53E+03	414	9.5
1400 RPM 100 Nm	4.22E+07	3.73E+06	3.98E+07	5.92E+03	405	7.7
1400 RPM 50 Nm	3.82E+07	4.69E+06	3.23E+07	2.84E+04	213	7.8
2400 RPM 450 Nm	4.96E+07	4.03E+06	4.64E+07	8.67E+03	460	11.4
2400 RPM 250 Nm	1.06E+08	4.23E+06	1.06E+08	1.39E+04	1093	17.1
2400 RPM 100 Nm	1.09E+08	4.77E+06	1.05E+08	1.19E+04	1010	14.4
2400 RPM 50 Nm	6.50E+07	3.90E+06	5.99E+07	7.08E+03	182	5.2
1000 RPM 250 Nm	1.92E+07	2.25E+06	2.23E+07	3.42E+03	293	9.6
1000 RPM 100 Nm	3.05E+07	2.36E+06	3.74E+07	6.25E+03	496	12.5
1000 RPM 50 Nm	1.84E+07	2.44E+06	1.82E+07	3.73E+03	182	5.2

**Table 4-4. Volume concentrations calculated from SMPS and EEPS size distributions**

Condition	SMPS, $\mu\text{m}^3/\text{cm}^3$		EEPS, $\mu\text{m}^3/\text{cm}^3$	
	Avg	Std	Avg	Std
1400 RPM 450 Nm	1.33E+04	1.13E+03	1.11E+04	5.33E+02
1400 RPM 250 Nm	1.15E+04	1.12E+03	8.84E+03	2.89E+02
1400 RPM 100 Nm	1.03E+04	9.79E+02	8.13E+03	2.21E+02
1400 RPM 50 Nm	4.78E+03	5.56E+02	3.66E+03	1.18E+02
2400 RPM 450 Nm	1.15E+04	1.19E+03	9.23E+03	3.10E+02
2400 RPM 250 Nm	2.85E+04	1.33E+03	2.00E+04	4.49E+02
2400 RPM 100 Nm	2.26E+04	1.19E+03	1.59E+04	3.52E+02
2400 RPM 50 Nm	1.06E+04	7.52E+02	7.58E+03	1.81E+02
1000 RPM 250 Nm	1.02E+04	9.80E+02	9.64E+03	4.42E+02
1000 RPM 100 Nm	1.77E+04	1.23E+03	1.52E+04	5.12E+02
1000 RPM 50 Nm	5.91E+03	6.57E+02	4.74E+03	1.87E+02

In Table 4-3, mass was estimated for the SMPS and EEPS from total particle volume and assuming a particle density of  $1 \text{ g/cm}^3$ ; 2400 RPM 450 and 250 Nm data are not shown because the backpressure upstream of the filter exceeded the AVL maximum backpressure for the instrument configuration that was used. A backpressure reduction module purchased with the AVL instrument was used in subsequent testing. At 1000 RPM, torques greater than 250 Nm, NO exceeded the 1000 ppm limit of the raw exhaust NOx gas analyzer, so this condition was not evaluated.

Figure 4-21 shows number size distributions from the SMPS and EEPS at two extreme conditions: 1400 RPM 50 and 450 Nm. At the tail of the accumulation mode, the EEPS drops off more rapidly than the SMPS. This phenomenon occurs because agglomerates pick up more charge in the charging section of the EEPS than a comparably sized spherical particle. This gives the particle a higher electrical mobility, which causes it to be classified as a smaller size. Consequences of the overcharging of agglomerates are:

- A higher peak concentration between 60 and 100 nm compared to the SMPS resulting from the overly charged particles registering in a smaller size bin, and
- The EEPS size distribution sloping more steeply than the SMPS as the particle size increases past 100 nm.

This has been observed previously,<sup>11</sup> and manufacturer TSI is working on an EEPS modification to correct this problem.

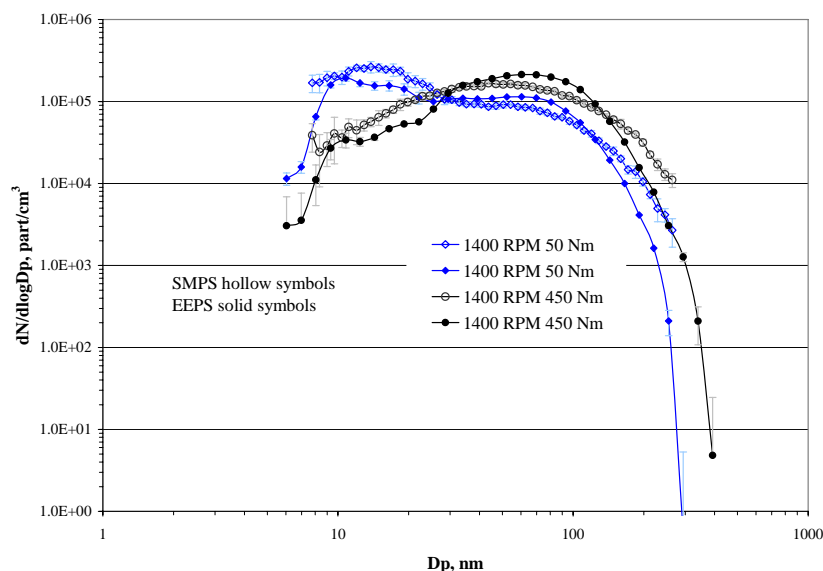


**Figure 4-21. Number size distributions from the SMPS and EEPS**

#### **4.2.3.2 Post DPF in Steady State and Transient Speed While Under Constant Load**

The engine was configured so fueling could be controlled with an analog input. This was done by installing a USB-6008 module and using National Instruments' LabView™ software to configure the USB module to continuously ramp the engine speed while under constant load. A torque of 250 Nm was chosen because it was the maximum torque that could be achieved at all desired speeds. The engine speed was ramped at a constant rate of 2 RPM/sec from 900 to 2400 RPM, the rated engine speed, and then back to 900 RPM.

Emissions were measured using the EEPS, AVL, and Honeywell sensor. The instantaneous dilution ratios were determined from raw and dilute NO measurements.

Figure 4-22 summarizes the results. The notations "UP" and "DOWN" correspond to increasing speed ramp and decreasing speed ramp. These data are then laid on top of each other by plotting response against engine speed. The EEPS and AVL are in good agreement, regardless of whether the engine speed is increasing or decreasing, and show a clear trend. However, the PM sensor shows a repeatable trend that does not appear to track with the other instruments.

To examine the more transient nature of the PM sensor, data was also logged directly from the sensor and preamplifier so that the unprocessed sensor information could be examined. This signal could then be logged on an engine cycle basis and could ultimately be used to determine the nature of the individual cylinder exhaust. Data were collected using a Kistler charge amplifier and analyzed by calculating the root mean square (RMS) voltage of the output. Using the PM sensor in conjunction with a commercially available Kistler preamplifier allowed the team to gather data independent of the Honeywell embedded electronics and to analyze the raw signal response to changing engine speed without any embedded filtering. Passive electronic filters or digital filtering may be able to make the response of the Honeywell sensor more specific to particulate matter and is under investigation.



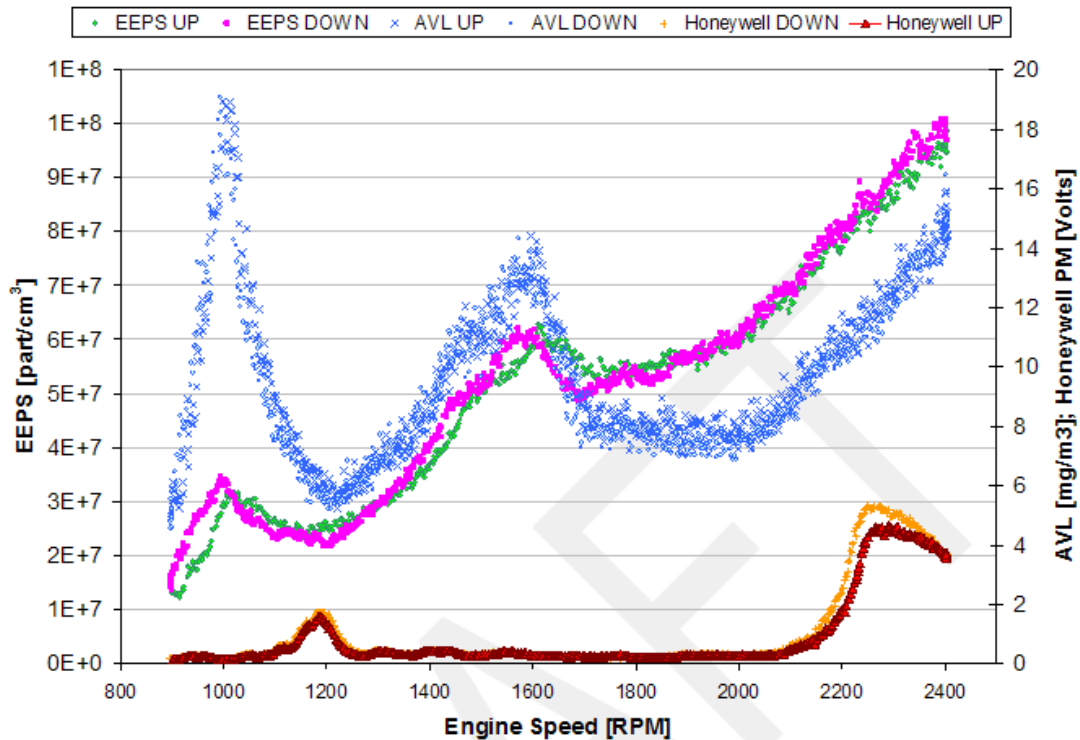


**Figure 4-22. EEPS, AVL, and Honeywell PM sensor response during engine speed ramp conducted at constant 250 Nm torque**

Throughout the engine speed spectrum, a number of peaks and valleys were observed by the EEPS and AVL indicating high or low concentrations in particle mass or number concentration. Although these features roughly lined up, the ratio of EEPS number concentration to AVL mass concentration varied. At 1000 RPM, the measured EEPS size distribution had a large accumulation mode with a mean size just above 70 nm. At speeds above 2000 RPM, the mean particle diameter shifted closer to 50 nm. This can be interpreted as a larger number to volume ratio for higher engine speeds and a lower number to volume ratio at 1000 RPM, with 250 Nm of torque. Particle diameter and surface area will have weightings that fall between particle number and particle volume. Tracking these weightings will provide insight into the relationship between the particle characteristics and the charge associated with the particles. For the PM sensor, there would be a closer correlation with the mass, concentration which itself correlates with a volume weighting.

The unfiltered PM sensor response with a Kistler charge amplifier does not appear to track with either of the particle instruments. Cause for the lack of correlation between the particle instruments and the PM sensor is unknown, but mechanical vibration was suspected and further investigate in Section 4.3.1.2.

#### **4.2.3.3 Using Bypass Configuration in Steady State Speed and Constant Load**

A major goal of this research program was to verify that the Honeywell PM sensor could detect a failed DPF. Given the limited number of DPFs available for testing, it was desirable to try to simulate a DPF failure without immediately breaking a DPF. Therefore, tests were conducted using a 1-1/2-in. NPT exhaust bypass pipe and gate valve to simulate a “leaking filter” as shown in Figure 4-23. The hope was that this simulation would enable a better calculation of how many holes or how much DPF surface area needed to be broken before failure occurred. In this case, failure was defined as surpassing the OBD threshold level of 0.030 g/bhp-hr.

With the DPF and bypass valve installed, upstream emissions were monitored as the valve was opened to determine the effects on upstream emissions. The bypass was expected to cause a decrease in engine backpressure, which could change engine-out emissions, but the valve had a negligible effect on upstream emissions even though it had a considerable effect on engine backpressure. Instruments were then moved downstream of the DPF and data were collected with the bypass valve at 0%, 25%, 50%, and 100% of the turns for a fully opened valve.

**Backpressure Testing**—A 4.5-L John Deere 4045 engine was used for backpressure testing (Figure 4-23). The engine was operated at 2400 RPM and 100 Nm on #2 ULSD diesel fuel (containing 5% biodiesel), a condition that maximized engine exhaust flow. Exhaust pressure and temperature were measured after the engine turbocharger. The dilution system was described previously. The bypass was a 1-1/2-in. NPT pipe and gate valve. The open area of the valve was determined through a relationship between the number of turns to open the gate valve and the open area of the valve (there is a nonlinear relationship between the open area and the number of turns). As the valve was opened, the change in area decreased with the increased number of turns. Figure 4-23 shows the sampling configuration and bypass location.

Testing began with a 15-min warm-up to bring up engine temperatures followed by 15 min at high load to regenerate the Donaldson DPF. After warm-up, the engine was adjusted to the test condition and allowed to stabilize for another 30 min before sampling began. Stabilization time was determined by continuously monitoring EEPS, AVL, and NO concentrations as well as all temperatures and pressures; sampling was started once all values had reached steady state. Figure 4-24 shows the addition of the PM sensor sampling points to the DPF system as well as the relationship of these sampling points to the bypass and DPF systems. The different sensor locations allowed conditions at several locations upstream and downstream of the DPF to be assessed as well as the ability to examine multiple sensors. Figure 4-25 shows the complete system on the engine in the test cell.

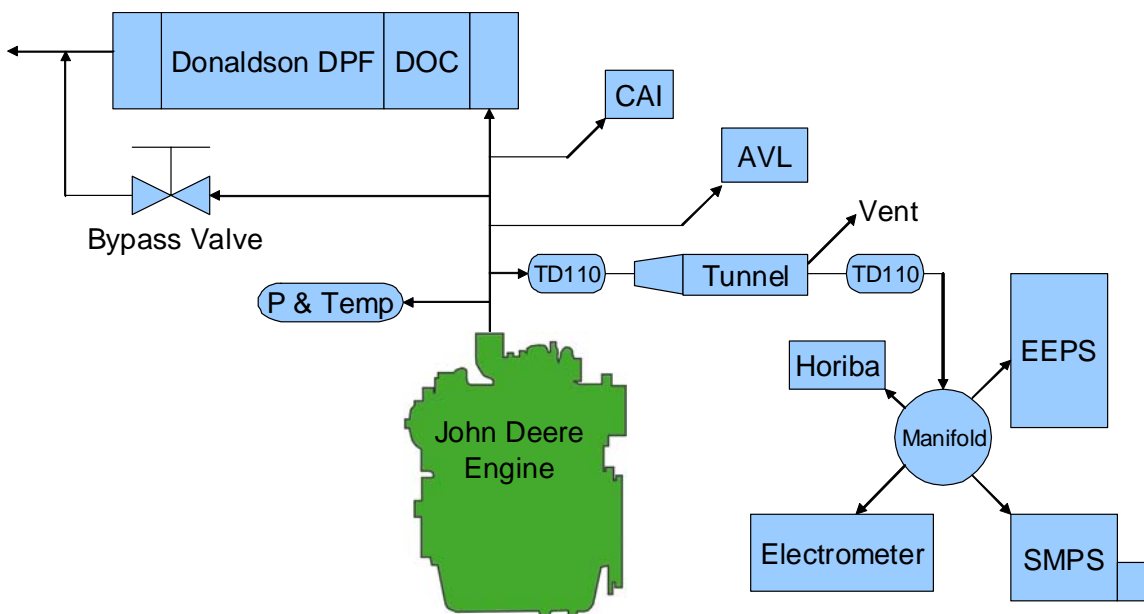
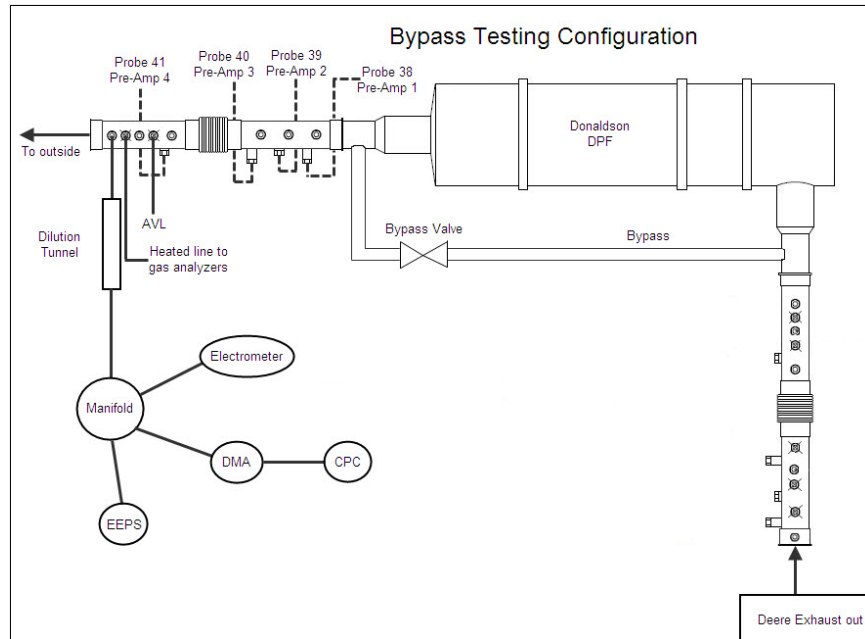


Figure 4-23. Backpressure testing schematic



**Figure 4-24. Instrumentation configuration for downstream sampling**



**Figure 4-25. Test engine, DPF configuration with bypass, and PM sensor locations**

**Results From Bypass Valve Testing**—Figure 4-26 shows the SMPS and EEPS number weighted size distributions as a function of bypass valve opening with standard deviations. The engine was operating at a mid-load condition of 1400 RPM and 350 Nm of torque. As expected, the size of the accumulation mode increased with increased valve open position, i.e., larger leak. At the tail of the accumulation mode, the EEPS drops off more rapidly than the SMPS. This phenomenon occurs because agglomerates pick up more charge in the charging section of the EEPS than a comparably sized spherical particle. This gives the particle a higher electrical mobility, which causes it to be classified as a smaller size. This results in the EEPS size distribution dropping off faster than that of the SMPS, as well as a high peak concentration due to the overly charged particles registering in a smaller size bin. As noted earlier, this has been observed previously,<sup>12</sup> and TSI is working on a modification to the EEPS algorithm to correct this problem.

As the bypass valve is closed, the shape of the size distribution remains essentially the same but the magnitude is reduced as expected. The only exception to this interpretation occurs when the valve is “fully closed” (0% open). In this position, the majority of PM is coming through the trap rather than the valve, and there appears to be a small nucleation mode tail around 10 nm. The instrumentation related root causes for this occurrence are discussed earlier in Section 4.2.3.1.

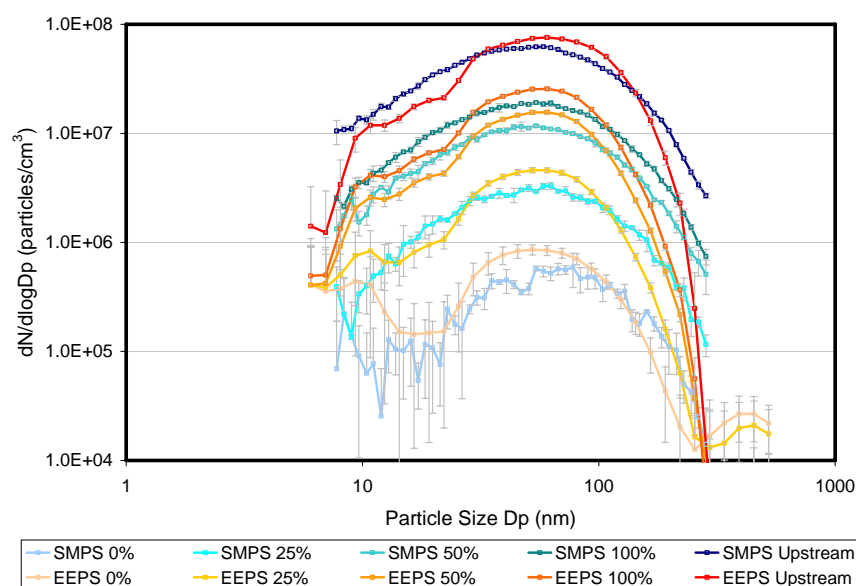


**Figure 4-26. SMPS and EEPS size distributions for varying levels of bypass valve opening**

Figure 4-27 and Figure 4-28 show mass concentration and brake-specific mass concentration as measured by the AVL and calculated from the EEPS and SMPS data. As expected, concentrations decreased as the valve was closed. SMPS mass concentrations were derived from the size distribution and an assumed density of  $1\text{g/cm}^3$  for particles less than 50 nm and a density of  $(50/D_p)^{0.6}$  for particles larger than 50 nm. This density and size relationship has been reported previously.<sup>13</sup> EEPS mass concentrations were determined assuming a constant density of  $1\text{g/cm}^3$ ; because of the misclassification of particles due to overcharging of large agglomerates, discussed earlier, the particle density and size relationship is not as simple. For purposes of this research, the AVL instrument was purchased and is considered to be the best indicator of real-time mass concentration. As shown in Figure 4-27 and Figure 4-28, the SMPS and EEPS track the AVL measurements, but there are significant differences in the average concentrations. It is believed that these differences are due to the fact that each instrument uses

different assumptions and algorithms to estimate mass concentration. Without having a specific EEPS transfer function for number concentration to mass concentration and with the SMPS' limited response time, the AVL, with a response time of 1 second and ability to detect down to  $1 \times 10^{-6}$  g/m<sup>3</sup>, was deemed to be the most responsive instrument for correlating measured mass concentration to the PM sensor signal.

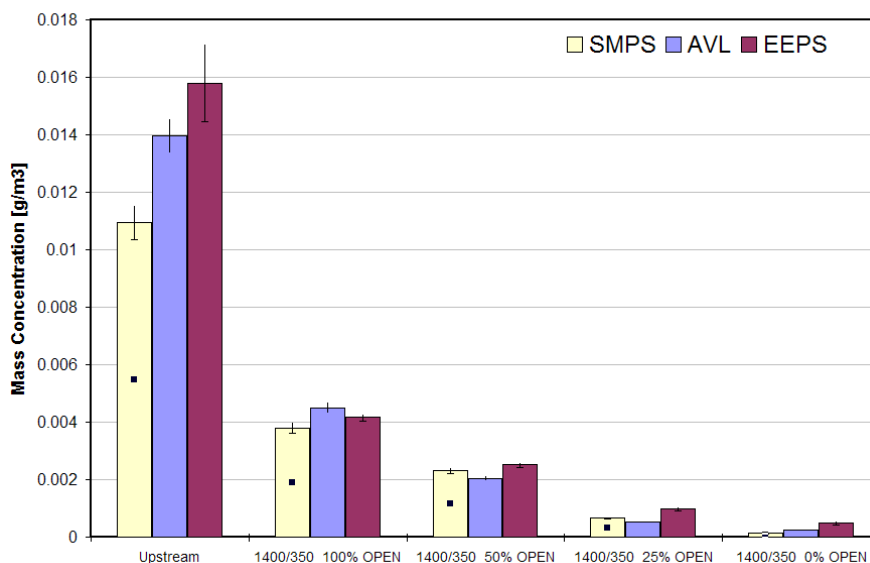


Figure 4-27. Mass concentration as a function of bypass of valve opening

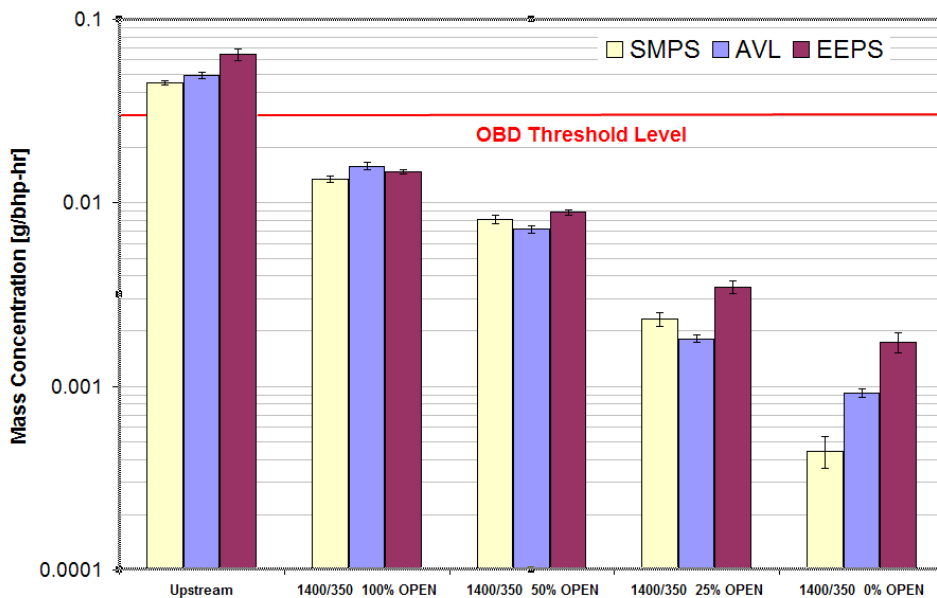
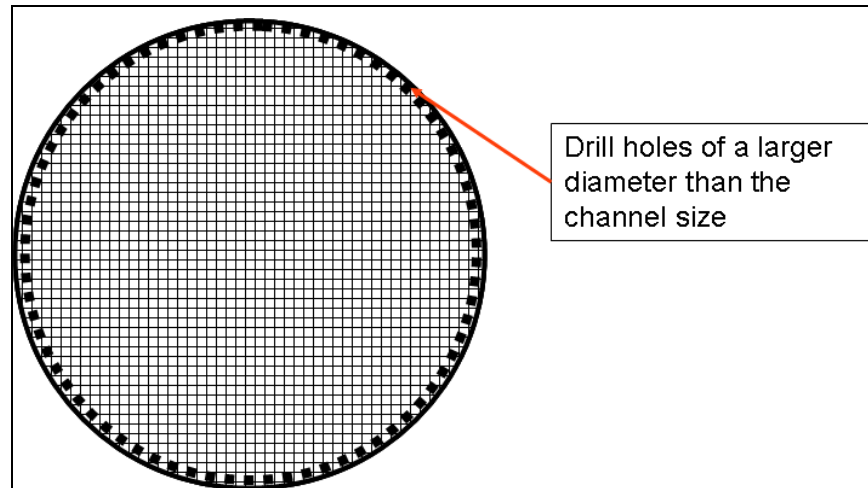


Figure 4-28. Brake-specific mass emissions as a function of bypass of valve opening

#### 4.2.3.4 DPF Failure Mechanisms and Experimental Simulation

**DPF Failure Mechanisms**—There are three basic DPF failure mechanisms: thermal separation, ring cracking, and failure of the DPF during catastrophic regeneration. These failure mechanisms were evaluated to determine how each could be emulated under laboratory test conditions.

For the thermal separation, penetrations were made around the perimeter of the DPF, allowing exhaust to bypass the DPF. This was done by drilling around the periphery of the DPF with a drill that is larger than channel size, thus emulating the separation, as shown in Figure 4-29. There might have been an issue here if these holes had to be resealed to use this DPF in a second failure mode.



**Figure 4-29. Thermal separation**

To emulate the ring cracking, a hole was drilled into the can and then a transverse hole was drilled into the DPF, as shown in Figure 4-30. The hole in the can could be sealed and the tests for failure conducted. The same issue in failure mode 1 (i.e., resealing) also needed to be addressed.

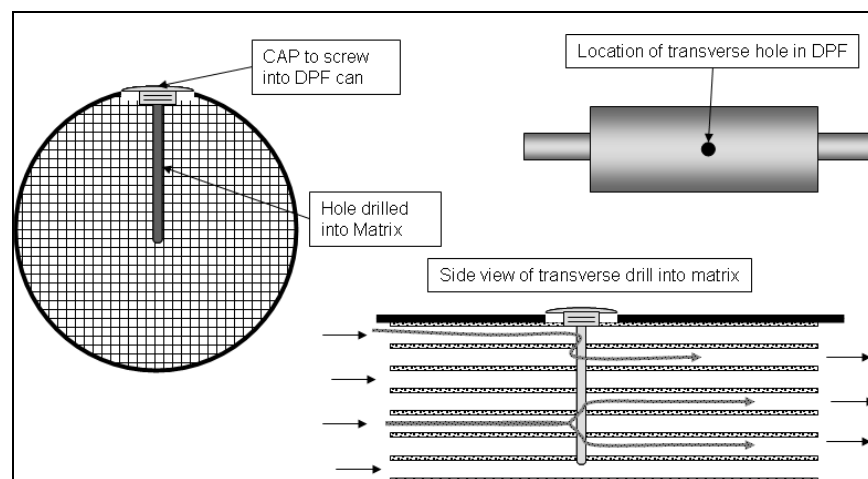


**Figure 4-30. Ring cracking failure**

The catastrophic failure of a DPF could be emulated by drilling holes in a subset of the DPF's end caps, as shown in Figure 4-31. These holes could be of a diameter smaller than the diameter of the DPF channel for the initial testing and then could be re-drilled to the diameter of the channel for additional tests.



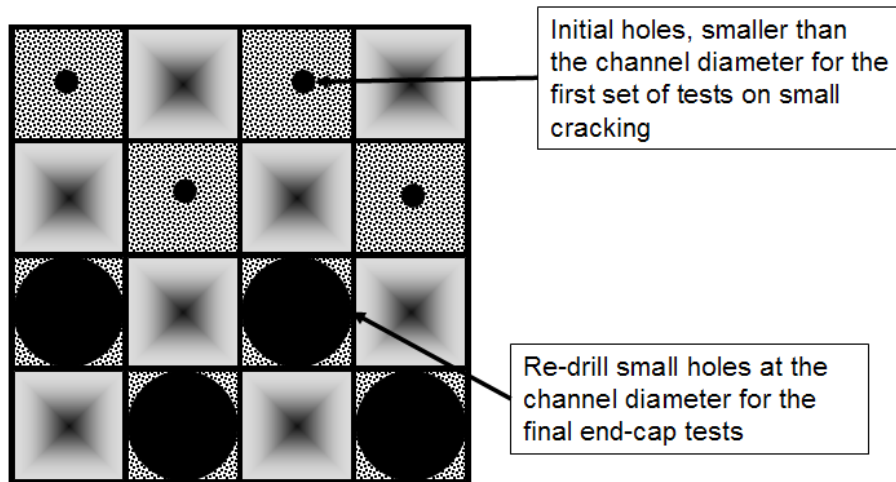


**Figure 4-31. Small and large end cap cracking for catastrophic failure**

From a review of field information and literature on these failure modes, the priority for DPF failing mechanisms was deemed to be:

- i. Thermal separation or cracking
- ii. Ring cracking
- iii. Small and large end-cap cracking or catastrophic cracking

Simulating thermal cracking of the DPF required that a number of holes be drilled around a part of the DPF core perimeter, a difficult process within the confines of the DPF can. Thus, we decided to emulate small end-cap cracks. This resulted in an increasing number of sections of holes in the downstream surface area of the DPF.

The failure mode of large end-cap cracks was to be conducted after analyzing the test results from drilling small holes in the end caps. This testing would have generated a larger penetration of particles, but was not completed in this program due to time and effort lost as breakdown of the Deere Engine occurred and transfer to the Isuzu engine was required.

To simulate the ring crack mode, it was thought of drilling through the can into the DPF core and, through a series of these drill holes, attempting to emulate a crack within the core of the DPF. To achieve this mode, the can would have to be modified to allow the addition of drill holes. This type of resealing of the can would be time-intensive for determining different failure modes, and thus we determined that emulating this failure mode could not be conducted within this program.

**DPF Failure Simulation**—Donaldson DPF failure was simulated first by drilling a series of holes in the end cap and then later by milling out a large section of the end cap that would emulate catastrophic end cap failure in the system. Since the initial intent of failing the DPF was to attain a DPF condition beyond the levels required for the OBD threshold and the initial failures up to 600 holes did not provide those levels of failure. The reason for milling out a large section of the DPF was that it made an easier method for opening those core elements. Even with many channels drilled out, the DPF still had a high degree of removal efficiency. Therefore, the decision was made to mill a relatively large area of the end cap. After each level of failure, the filter was reinstalled and PM emissions downstream of the DPF were evaluated. These results were then compared to testing conducted with the exhaust bypass valve to determine whether the sensor could distinguish 0.010 g/bhp-hr of PM from background noise.

A cutaway showing the internal flow path through a section of the Donaldson DPF is shown in Figure 4-32. The DPF has 100 cells per square inch (15.5 cells/cm<sup>2</sup>) with a 0.017-in. (0.43 mm) wall thickness. Therefore, the open area of any given cell is a square with a side length of 0.083 in. (2.1 mm). Each cell is 14 in. long (35.6 cm).

The DPF was failed by drilling out end caps on the outlet side of the filter. This allows some of the exhaust to enter the filter through an open channel and exit the filter through a hole in the end cap on the opposite end. A sufficiently small, 0.0625-in. drill bit was chosen to fail the end caps in order to minimize damage to the filter wall. The holes were drilled by hand using a cordless drill. This process is shown in Figure 4-33.

Failure started in the center and then moved outward. Figure 4-34 shows the hole patterns that were drilled. Emission testing downstream of the Donaldson DPF was conducted with 0, 100, 200, 300, 600, and 900 holes. For the final failure it was decided that 1800 end caps would be milled off which included all end caps which originally had holes. The result of this milling process is shown in Figure 4-35.

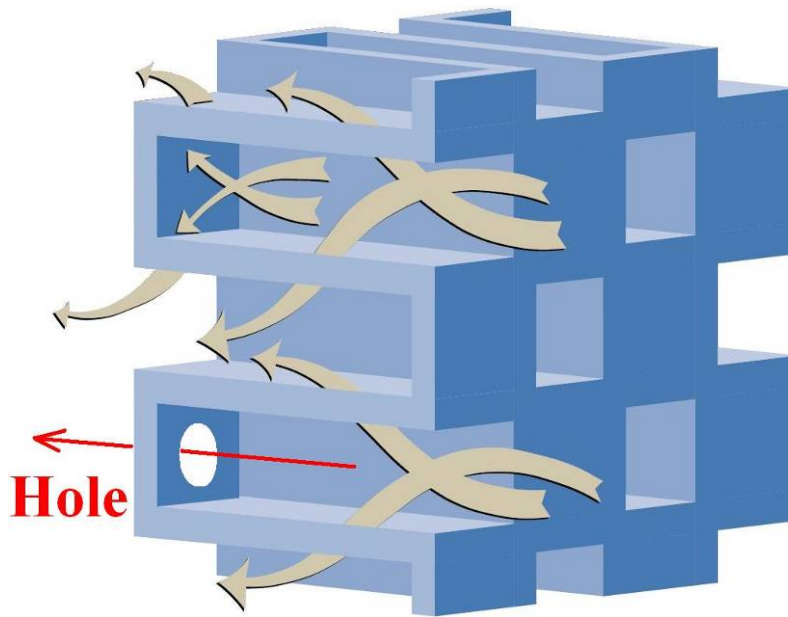
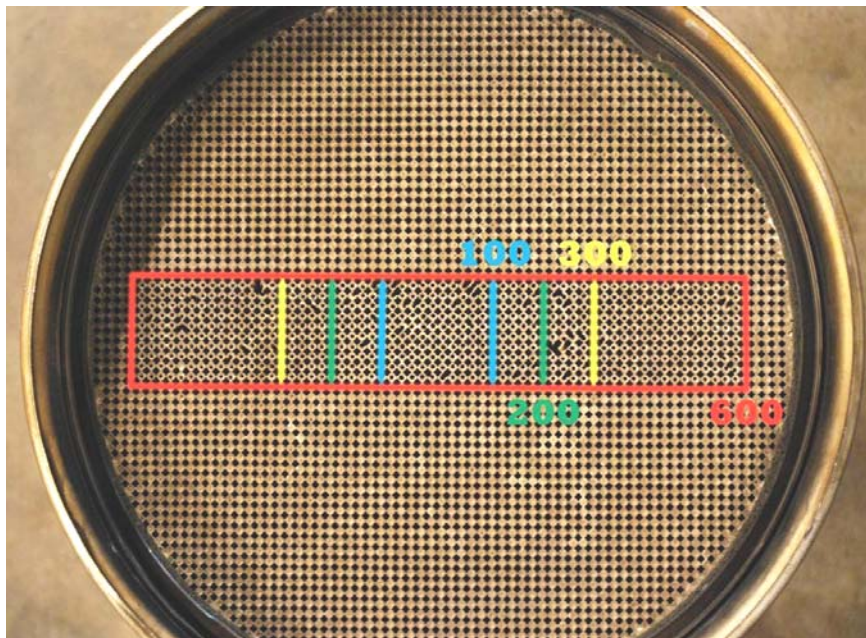


Figure 4-32. Flow path in Donaldson DPF<sup>14</sup>





**Figure 4-33. Drilling holes**



**Figure 4-34. Hole patterns**



**Figure 4-35. 1800 milled holes**

**Setup for Testing the Failed DPF**—PM emissions testing downstream of the failed DPF was conducted in the same manner as testing done downstream of the filter and bypass valve. However, testing began on the 4.5-L John Deere engine but was subsequently moved to the 5.2-L Isuzu engine due to a malfunction within the John Deere dynamometer that rendered it inoperable. The Isuzu engine is a more modern on-road engine with lower engine-out particle emissions than the Deere at a similar engine condition. To better simulate the emissions from the Deere engine, the intake airflow was throttled (restricted), causing the engine to run closer to stoichiometric conditions and resulting in increased PM emissions. The throttle was adjusted so the AVL measurement upstream of the filter was similar to that seen on the John Deere engine before the dynamometer failure ( $\sim 14 \text{ mg/m}^3$ ). Conditions of 0, 100, 200, 300, and 600 drilled holes were tested with the John Deere engine, while conditions of 900 holes and 1800 milled end caps had to be tested with the Isuzu engine. PM emissions were monitored using the SMPS, AVL, EEPS, and gravimetric filters. SMPS and EEPS mass concentrations were derived as discussed in Section 4.2.3.3. Gravimetric filter samples were collected on 47 mm Teflon filters at a flow rate of 72 LPM. Filters were weighed using a Cahn Microbalance, and values reported are the averages and standard deviations of four filters.

## **4.3 On-Engine PM Sensor Measurements, Analysis and Results**

### **4.3.1 *Experimental issues during on-engine PM Sensor Testing***

Initial testing during the program had discovered that there was a problem with using short lengths of BNC cabling between the sensor probe and the preamplifier. Signal noise was being generated during operational vibration and thus a switch to shorter lengths of triaxial cable was made. Testing indicated that there was a reduction in the noise, but when particle mass concentrations were sufficiently small and the amplifier gain had to be increased, the signal to noise levels were not much improved. To reduce this component of the signal noise as well as to eliminate any electronic noise pickup from the connectors, testing was done to determine if

the preamplifier could be integrated directly with the probe. The results of the testing found that temperatures at the interior of the preamplifier box were sufficiently low and thus testing was done on an integrated probe-preamplifier unit. This seemed to greatly improve the PM signals.

#### 4.3.1.1 Deere Dynamometer Failure and Change to Isuzu Engine and Dynamometer

Tests were conducted on two different engines due to the failure of the dynamometer on the first engine. This occurred after 600 holes had been drilled into the DPF during the tests conducted on the first engine. With the loss of the dynamometer, this first engine could no longer be used for testing. A second engine was then adapted for the DPF testing. This new engine had a different dynamometer and exhaust system. The exhaust run from the new engine to the DPF system was much longer with a more flexible exhaust pipe. The initial tests results indicated a marked difference in the PM sensor response. Although this was a different type of engine, the engine was adjusted so that the output particle mass was about the same as for the first engine. This was verified through comparison of the exhaust particle concentrations. The results of these measurements are shown in Figure 4-36.

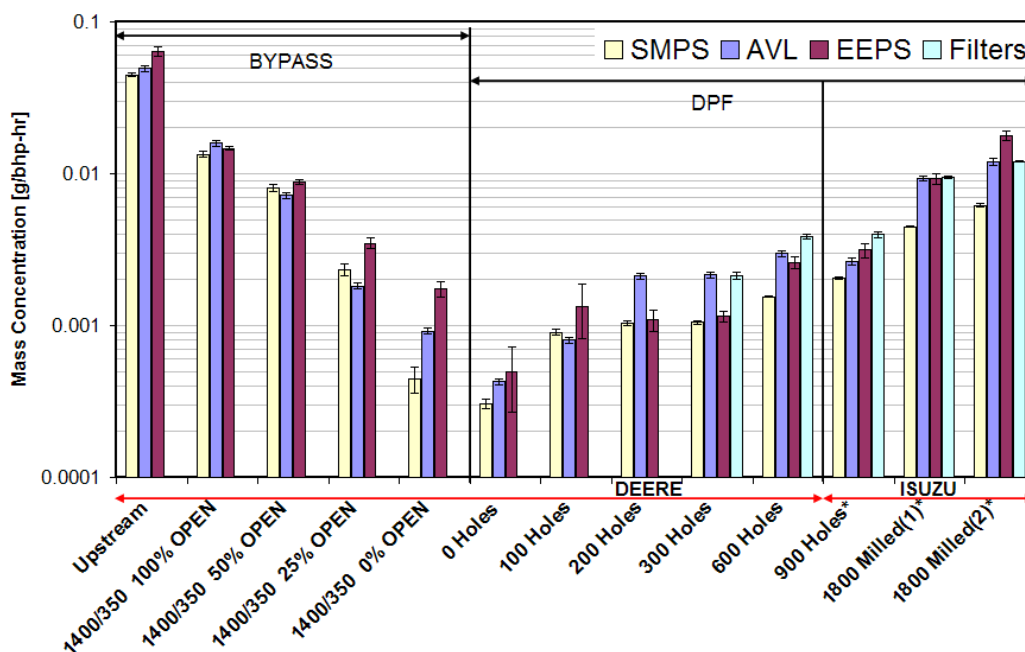
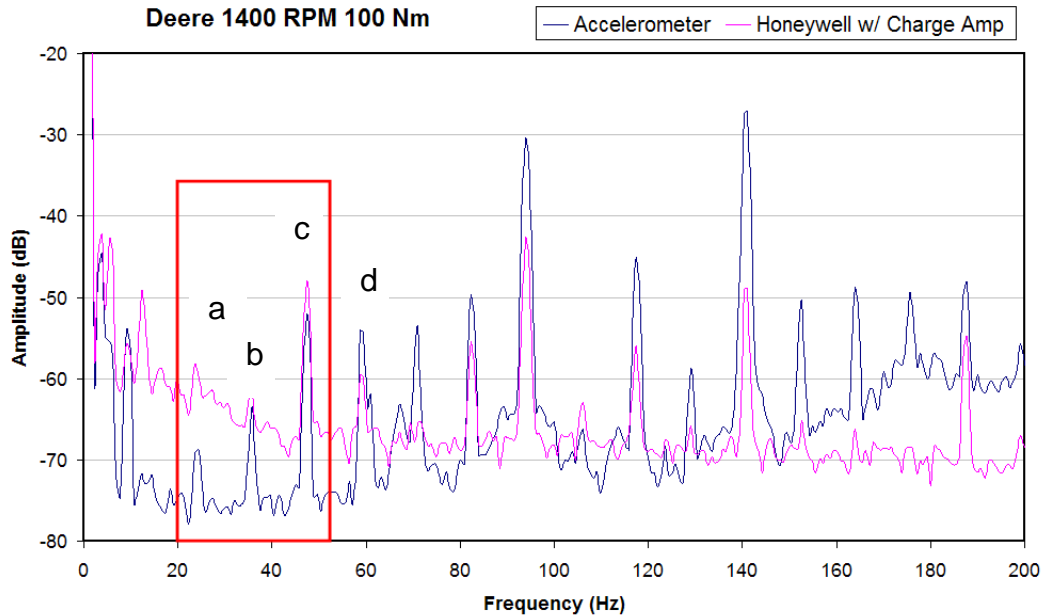


Figure 4-36. Mass concentration

#### 4.3.1.2 Vibration-Induced and Ground-Coupled Noise

Tests using an accelerometer and the PM sensor in combination with a Kistler charge amplifier were conducted for a number of engine load and speed combinations. Figure 4-37 shows the results at 1400 RPM and 100 Nm. Data were logged for both sensors at 2 kHz, and a fast Fourier transform (FFT) was used to convert these data to frequency domain.





**Figure 4-37. Accelerometer and Honeywell sensor response with Kistler charge amp at 1400 RPM and 50 Nm**

In the frequency band of interest between 20 to 50 Hz, the firing frequency at 46.7 Hz, labeled (c) in the Figure 4-37, is clearly visible. This is intrinsic due to an engine speed of 1400 RPM for the 4-cylinder Deere. Unfortunately, additional vibration peaks at frequencies such as 35 Hz and 23.8 Hz, labeled (b) and (a), are also present in frequency band of interest resulting in large variances in the PM sensor signal. In addition, 60 Hz ground loop noise is identified as peak (d) in Figure 4-37, appearing on purpose outside the frequency band of interest. It was evident that interference from mechanical vibration may have been modifying the signal that was expected from each individual exhaust event.

In an attempt to remove the vibration components of the signal, another test was conducted where the sensor was held in the exhaust without touching the exhaust pipe. This created a small exhaust leak at the port where the sensor was usually attached to the exhaust pipe. Backpressure from the exhaust system kept the flow of exhaust outward and over the sensor. Figure 4-38 shows the response of the PM sensor, which was suspended in the exhaust stream and then screwed into the exhaust saddle, making the usual sound mechanical connection. Data were collected using a Kistler charge amplifier, and logging of the output was triggered by an encoder on the engine, which gave a pulse every 0.5 crank angle degree.

Data are shown in Figure 4-38 for 720 crank angle degrees, one engine cycle. The decision to determine the cylinder effects by crank angle was made because of how the data logging was triggered and also because this indicated one complete engine cycle. During this engine cycle, four exhaust events occurred, one for each cylinder. When the sensor was not rigidly connected to the exhaust pipe, these four exhaust events were clearly visible; however, once the sensor was connected, this signal was masked by a much larger, seemingly sinusoidal noise signal. Removal of the vibration component of the signal could be done either through signal processing or by redesigning the sensor and mount to reduce the response to mechanical vibration. The initial design focused on the reduction in the vibration component of the signal through electronics and signal processing, as we believed this held more promise than trying to eliminate the vibration through the sensor mount.

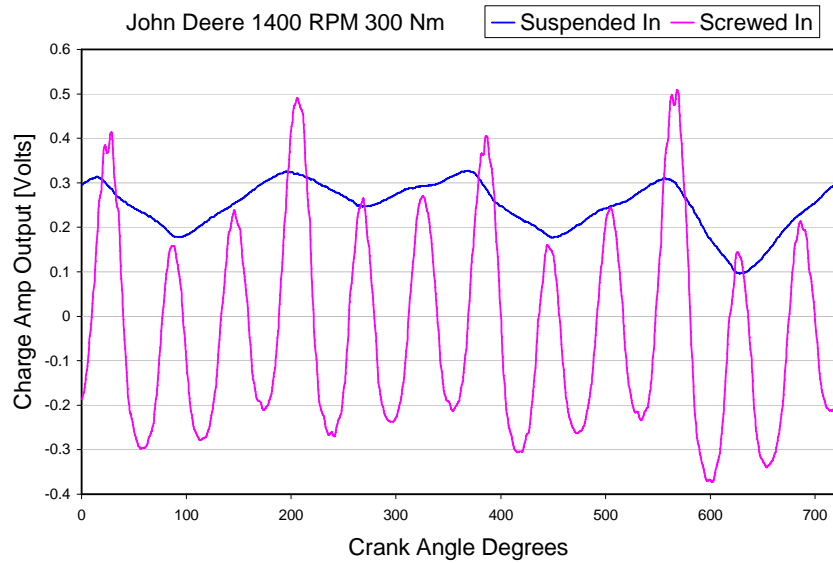


**Figure 4-38. Honeywell sensor suspended in exhaust**

#### **4.3.2 In Pre- and Post-DPF Configuration Under Functional DPF Conditions**

To assess how the amount of post-DPF bypass mass concentration compared to the upstream concentration, the initial post-DPF mass concentration data, which are taken on the Deere engine, were compared to data taken earlier. This comparison is shown in Figure 4-39. Initial indications are that 30% of the upstream mass concentration can be made to bypass the DPF through the added bypass channel.

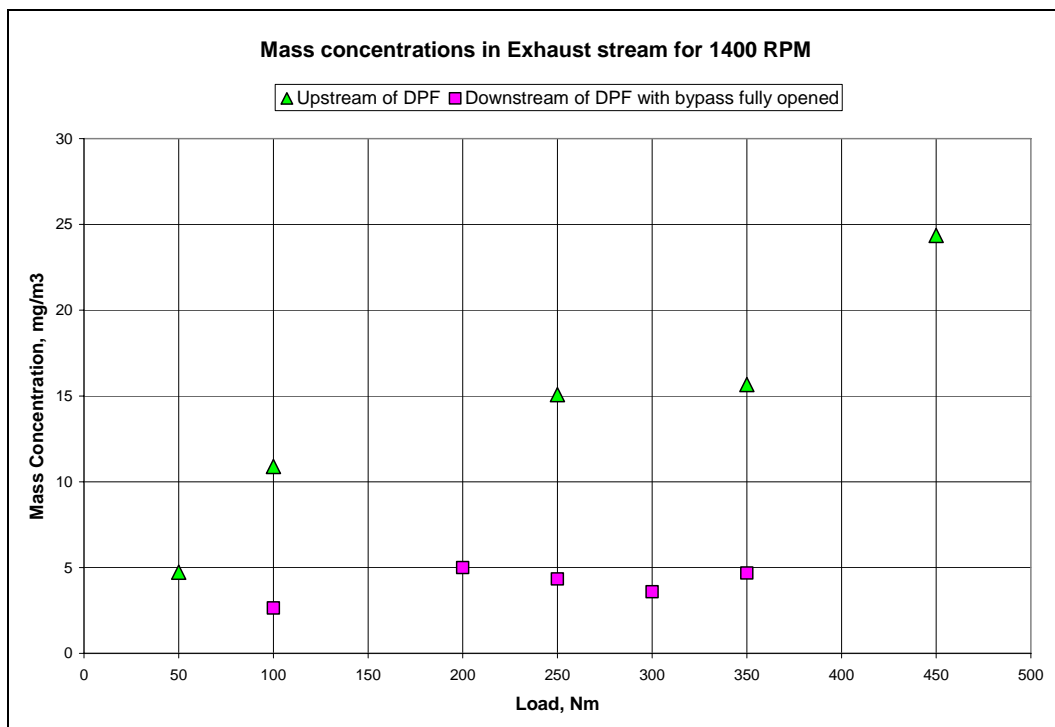


**Figure 4-39. Mass concentration for bypass exhaust vs. upstream of DPF**

To verify the correct operation of the PM sensor during testing, analysis was conducted to determine why the signal varied during testing. A frequency analysis of the output signal revealed the presence of noise at higher frequencies than expected. This appeared to indicate the pickup of vibration noise. This was a possible explanation for the increase in PM sensor amplitude obtained during the probe-check tests. To minimize some of the frequency effects, the output data from the sensors were analyzed at periods of minimums in the FFT response. The frequencies considered were in the range of 20 – 50 Hz and the analysis did not include the frequency peaks found at the engine response frequency or multiples of that frequency. Several series of data at these frequency bands were averaged over 100 sequential samples and displayed as a function of load. This was also compared with the mass concentration measured during this period. The results were plotted against engine load at a constant speed (see Figure 4-40). The resulting plot shows that the mass concentration varies as might be expected during these load changes, but the analyzed PM sensor output still had considerable variance in the PM sensor signal. This method of analysis indicates that there is still considerable sensor noise between the FFT peaks in the range.

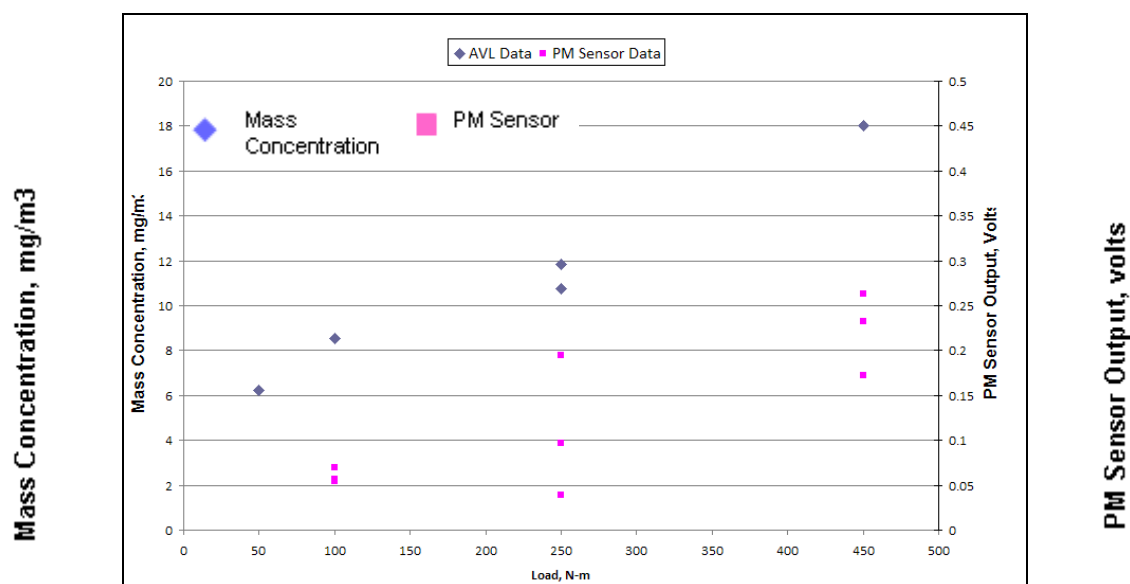


Figure 4-40. Comparison of PM sensor output signal from sequential frequency data

### 4.3.3 In Bypass Configuration

This section describes the Deere on-engine PM sensor measurements, analysis, and results in bypass configuration before failing the DPF system. Prior to performing the actual measurements, calibration of particle and mass concentration instrumentation as well as calibration of the experimental bypass setup was performed as described in Section 4.2.2 and 4.2.3.3, respectively. A schematic and picture of the experimental setup are shown in Figure 4-24 and Figure 4-25, respectively.

An initial comparison between the mass concentration and the PM sensor response is shown in Figure 4-41. Four sensors were run under multiple tests and compared with the mass concentration readings from the AVL PM emission measurement equipment. For the most part, the PM sensors appeared to be providing a good correlation with the mass concentration and the noise levels (taken as standard deviation) appeared to indicate a smaller signal-to-noise level than initially seen using the preliminary electronics and connections described in section

1.1. The output signal shown for the PM sensors is in volts. Note the difference between the output signals for the four sensors, which may be caused by variations in the probes or may be produced by variations in the flow as it enters downstream of the DPF.

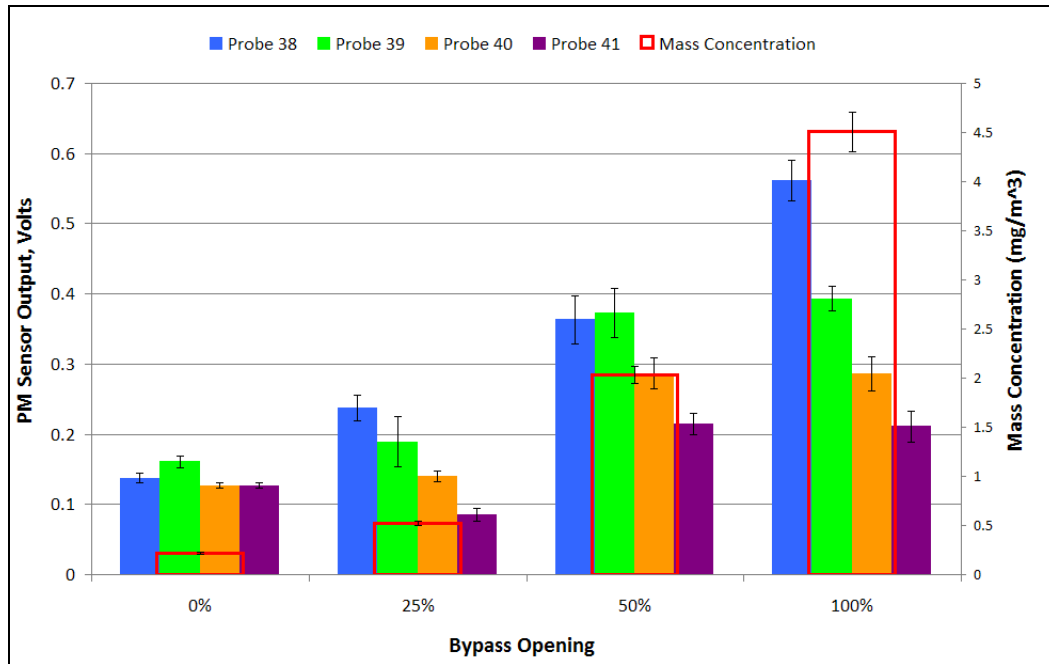


**Figure 4-41. PM sensor response compared to mass concentration**

To correlate the PM sensor with the OBD requirements, the PM sensor levels are also shown in Figure 4-42 with the g/bhp-hr levels. The data in Figure 4-42 indicate that the average sensor readings show changes as the bypass is opened and that these changes occur for levels that are lower than the OBD threshold of 0.03 g/bhp-hr.

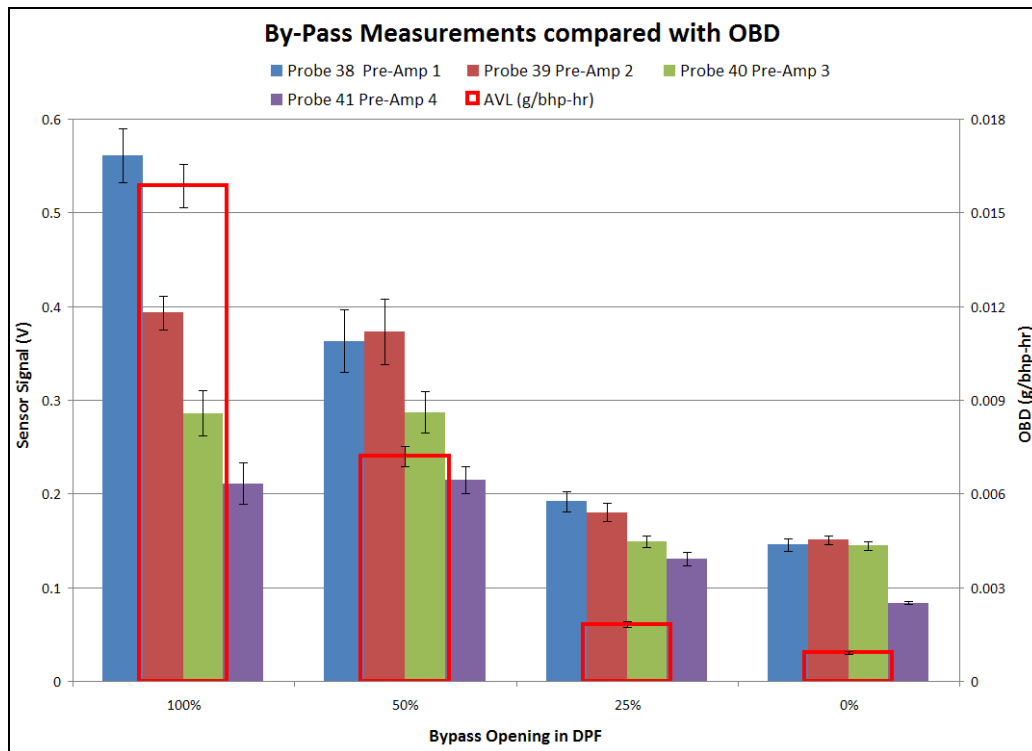


**Figure 4-42. Sensor response compared to OBD levels**

To measure the particle charge levels at the sensor location, electrometer measurements were initially made. Figure 4-43 shows the correlation of the raw output of these measurements with the PM sensor output. At the 25% opening of the bypass a negative value of the average charge concentration was determined. An examination of the variance in the charge measurements indicated that the charge concentration would be within the trend seen for the bypass opening. Additional testing at this condition would have to be conducted to determine the reason for the large variance seen. The lack of precise data at this measurement point probably does not affect the conclusions drawn in this project but suggests a need to further refine the charge per particle in the exhaust and determine if there was any impact from small variations in the engine operation.



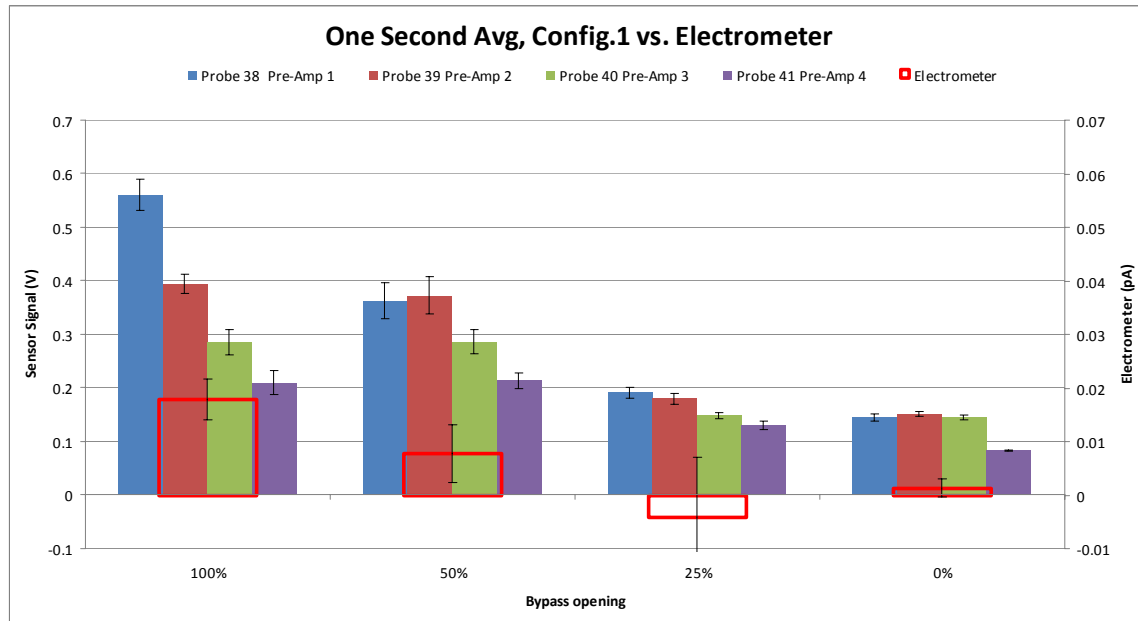


**Figure 4-43. Comparison of initial charge measurements with PM sensor output**

The opening of the bypass valve is related to the mass concentration downstream of the DPF. It is also important to understand how the bypass mass concentration is related to the OBD exhaust standards. Figure 4-44 indicates how the mass concentration relates to the opening of the valve at two different engine speed/load points. The variance is also shown for the initial data.

Figure 4-45 shows the response of one of the PM sensors as a function of different engine loads for the bypass valve open and closed. The bypass valve was open 100% during the tests utilizing the bypass system. Figure 4-46 indicates the PM sensor output in volts compared against the mass concentration as measured by the AVL for different openings of the valve (shown as number of turns open in the figure). The higher soot-producing engine condition indicated a response to the increased particle mass, but only when the concentration level was high (in this case, over nine turns for the valve), as shown in Figure 4-46. The lower soot-producing engine condition of 100 Nm showed almost no PM response above the baseline level. The amplifiers used in gathering the data were set based on the mass concentrations found upstream of the DPF, and the amplification factor needs to be reset for the low concentration range. These initial data were used to reestablish the amplification for conditions downstream of the DPF.

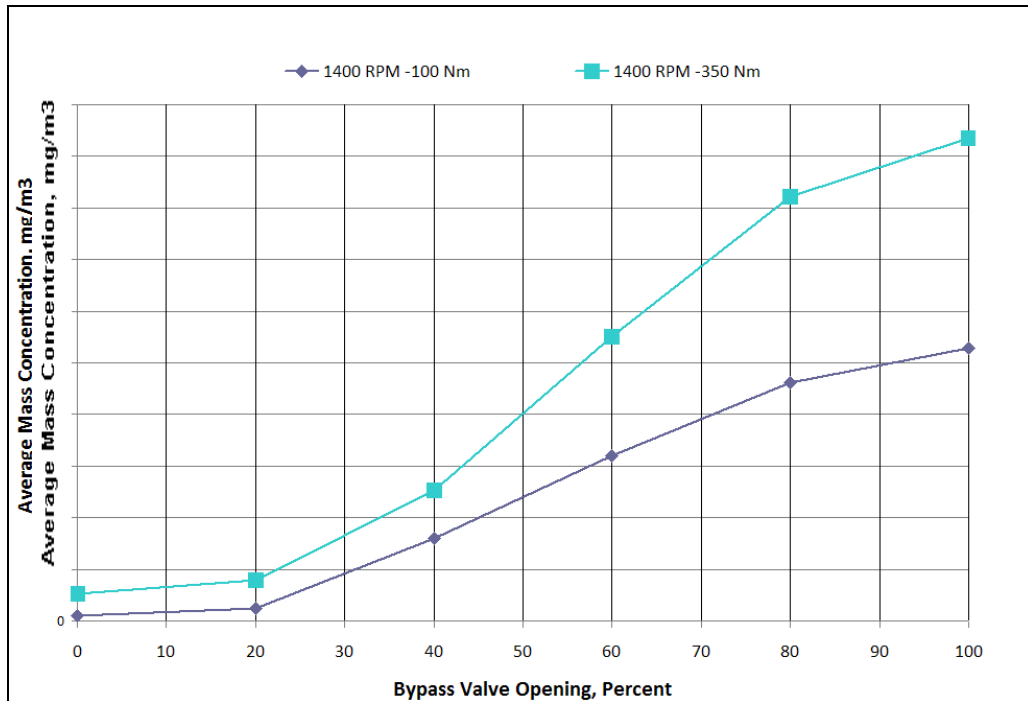


Figure 4-44. Average mass concentration as a function of bypass opening

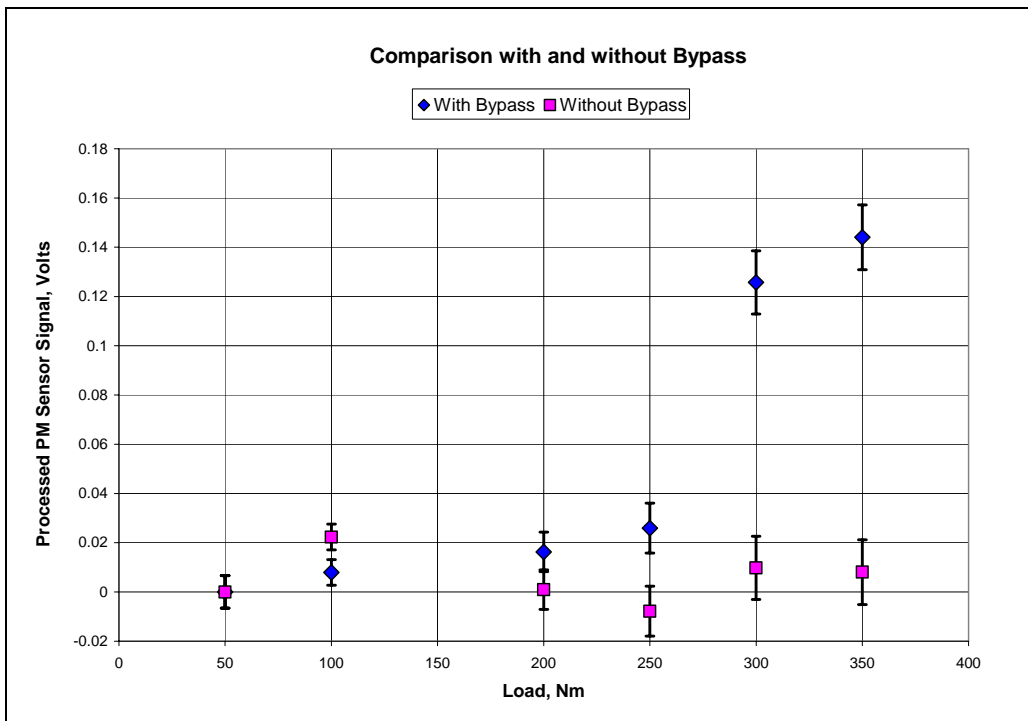
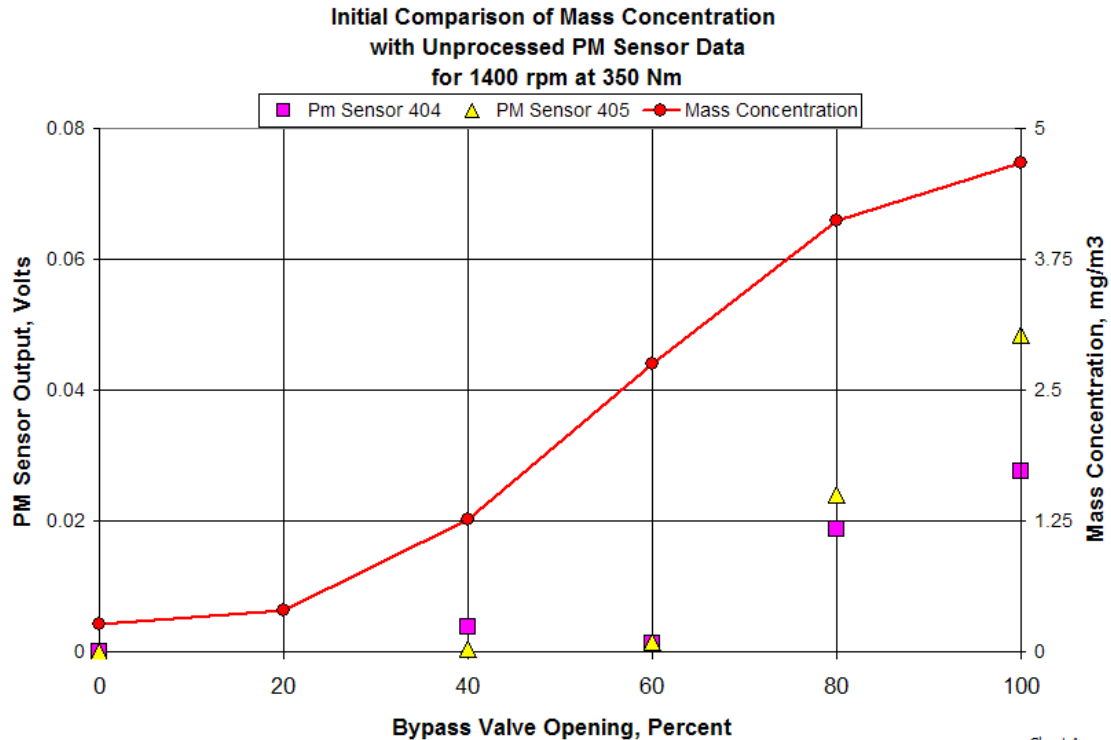


Figure 4-45. PM sensor response downstream of DPF for different loading conditions



**Figure 4-46. PM sensor and mass concentration during bypass operation**

#### **4.3.4 In Post-DPF Configuration Under Failing DPF Conditions**

PM testing was conducted in post-DPF configuration in which the DPF was progressively failed by drilling through the downstream face of the DPF. These measurements were supported by the Deere engine, particle, and charge measurements in the post-DPF environment. Charge/particle measurements were made to assist in determining if the PM sensor was actually responding to charged particles in the post-DPF environment (i.e., that the PM sensor measurements were due to the charge associated with the particles passing through the DPF). Measurements were conducted on a functioning DPF with a goal of failing that DPF to a level near the OBD threshold of 0.03 g/bhp-hr. The rationalization for setting this goal is that the failure technique should produce downstream particle concentrations below the 3x certification level to determine if the sensor can robustly discern various levels of degradation leading up to the OBD threshold.

The configuration of the PM sensors and the particle, charge, and engine monitoring equipment for making these PM measurements is identical to the bypass configuration described in Section 4.2.3.3 except that the bypass valve was closed. Figure 4-24 shows the probe configuration and the location of the probes within the exhaust system. Section 4.2.3.4 describes DPF failure modes and experimental simulation of a failing DPF. Measurements of the exhaust particle properties were used to determine the effectiveness of the PM sensor response for each of the selected DPF failure modes. In addition, data from the tests were used to determine the particle charge characteristics and mass concentration of diesel exhaust particles.

##### **4.3.4.1 Results of DPF Failure Testing**

Figure 4-47 shows brake-specific mass concentrations downstream of the filter as a function of degree of DPF failure i.e. number of holes. The DPF was failed until the same range of outlet concentrations as with the bypass valve was covered, which is also shown Figure 4-47. Milled 1

and 2 correspond to two different levels of engine throttling (i.e., upstream concentration with the same number of holes). Discrepancy between 0% valve opening tests and a fully functional DPF is attributed to potential valve leakage. The gate valve had a metal-on-metal seal to tolerate the extreme temperatures in the exhaust. For the DPF testing, the bypass valve was closed. The bypass pipe was left in place so that the flow conditions downstream of the DPF would remain the same. Initially, without the bypass in place, the unmodified DPF had a removal efficiency for both mass and number of greater than 99% removal. The same particulate levels as 100% valve opening were not reached until 1800 end caps were milled off of the filter. This corresponded to an open area of 12.4 in.<sup>2</sup> (80 cm<sup>2</sup>). The cross section of the valve at 100% opening only has an open area of 1.77 in.<sup>2</sup> (11.4 cm<sup>2</sup>). This was partially because the exhaust flow going through the failed DPF goes through a diesel oxidation catalyst (DOC) that is upstream of the filter, and flow going through the bypass valve does not. The DOC removes a portion of the volatile hydrocarbons in the exhaust stream but leaves the elemental carbon mostly unaffected; however, a major contributor to this discrepancy is that the open area of the failed filter is made up of a large number of narrow long channels. Even though the failed channels are open on both ends, they still promote wall flow by having a relatively large pressure drop due to their geometry.

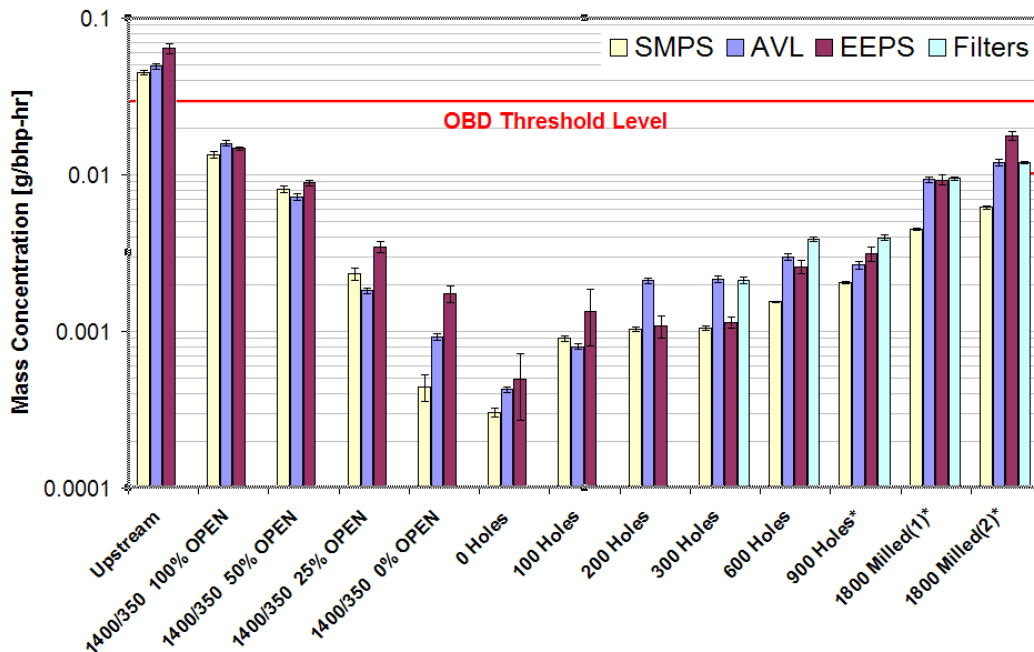


**Figure 4-47. Brake-specific mass concentration as a function of DPF failure degree**

The current PM mass emission standard for an on-road heavy-duty diesel engine is 0.010 g/bhp-hr. This threshold is crossed between 50% and 100% valve opening and 1800 milled holes from throttling position 1 to 2. For the failed DPF, the AVL and gravimetric filter samples are considered the standard and showed excellent agreement.

#### 4.3.4.2 Charge Measurements

During testing on the Deere engine of the failed DPF, charge measurements were made to better understand the nature of the particles penetrating through the failed DPF. Figure 4-48 shows the measured charge fraction and Boltzmann equilibrium for a number of conditions. This measurement was made by putting an electrostatic precipitator before the SMPS. Three scans were taken with the voltage off, and then the voltage was turned on to 7 kV, removing all charged particles and allowing only the neutral particles to pass through. An additional three

scans were taken, and by subtraction, the fraction of particles of a particular size carrying a charge could be found. The electrostatic precipitator removed charged particles regardless of polarity. The center rod was held at +7 kV and the outside was grounded so positively charged particles were lost to the outside wall and negatively charged particles were lost to the center rod. This measurement became increasingly difficult at low concentrations and was the reason for large error bars on the 300 holes case. For all other cases shown, the charged fraction fell between Boltzmann equilibrium at 1000 K and 1500 K.

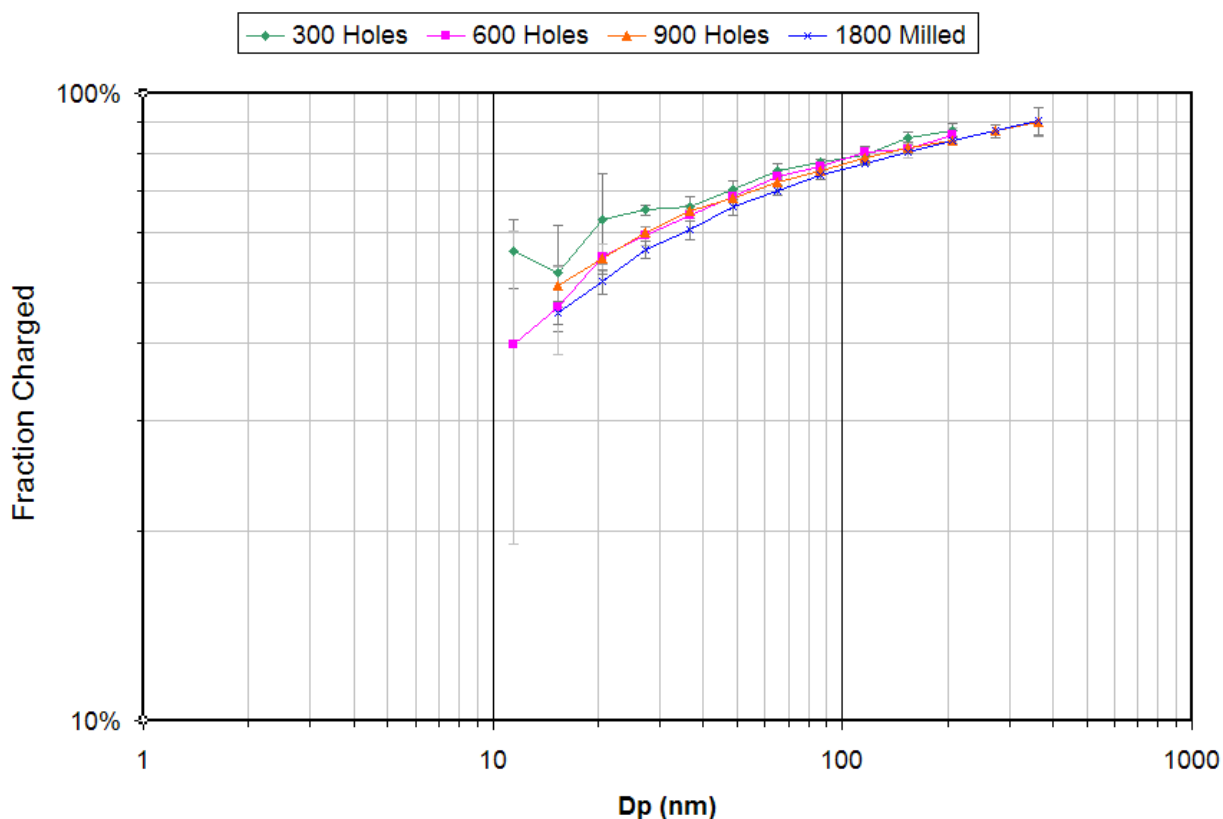


**Figure 4-48. Charge fraction**

Figure 4-49 shows the net charge of the aerosol sample after dilution. The net charge is basically the total charge for the particles being sampled. A near-zero net charge meant the number of positive charges and negative charges were balanced. A positive value is indicated by a higher number of positive charges. (An aerosol can have a high charged fraction and still be net neutral.) Figure 4-48 and Figure 4-49 show that as the DPF was being failed, the fraction of particles carrying some degree of charge stayed relatively constant but the net charge increased. An insert into Figure 4-49 provides a more detailed examination of the net charge levels for the modified DPF only.

There appears to be a large difference between the net charge downstream of the modified DPF and that seen downstream of the bypass. This aspect of the data has not been completely evaluated yet, but one explanation could be the removal of charged material on the grounded surfaces of the valve and surrounding pipe in the bypass through charge deposition mechanisms on the grounded surfaces.

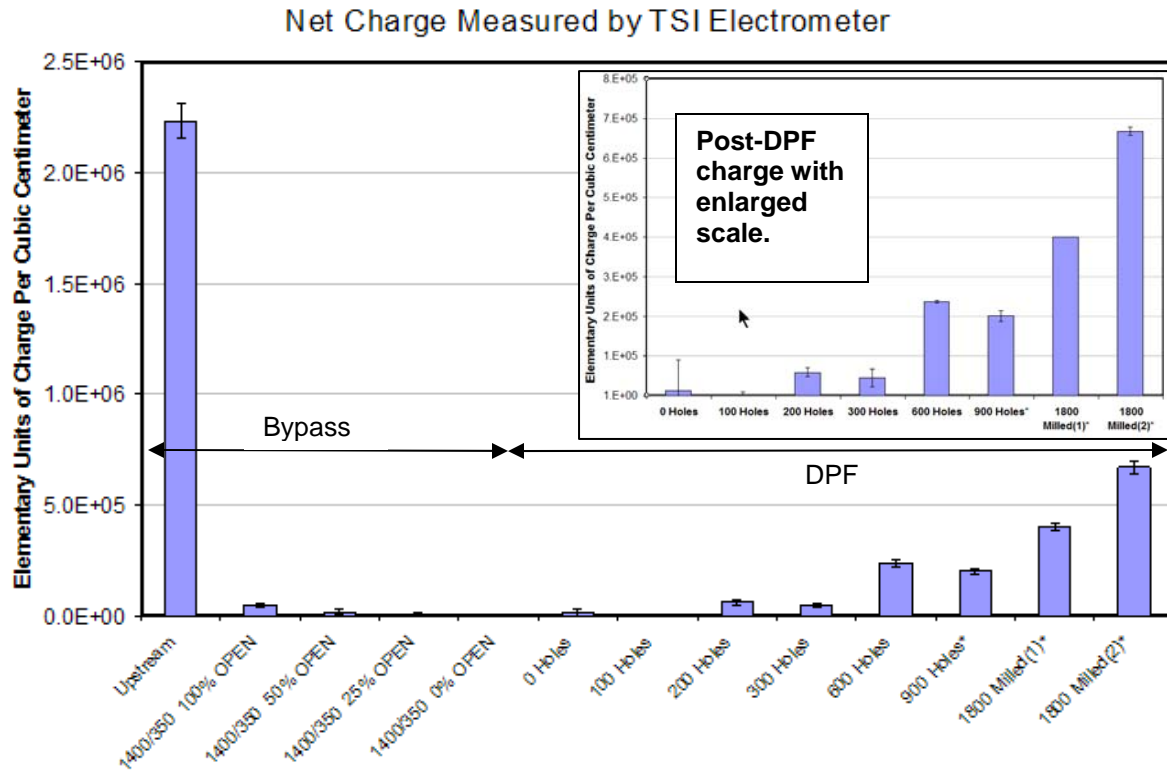


**Figure 4-49. Net charge for both bypass and DPF measurements**

Initial results of DPF failure tests were evaluated against mass concentration, as shown in Figure 4-50. Data from the two probes shown indicate increased signal due to the DPF failure, but there appeared to be little change in the particle mass concentration between the 200 hole failure and the 300 hole failure. In addition, the response of the PM sensor was compared to the results of the previously conducted bypass testing shown in Figure 4-51. The mass concentration and correlation to the PM sensor appeared to be similar between these two methods.

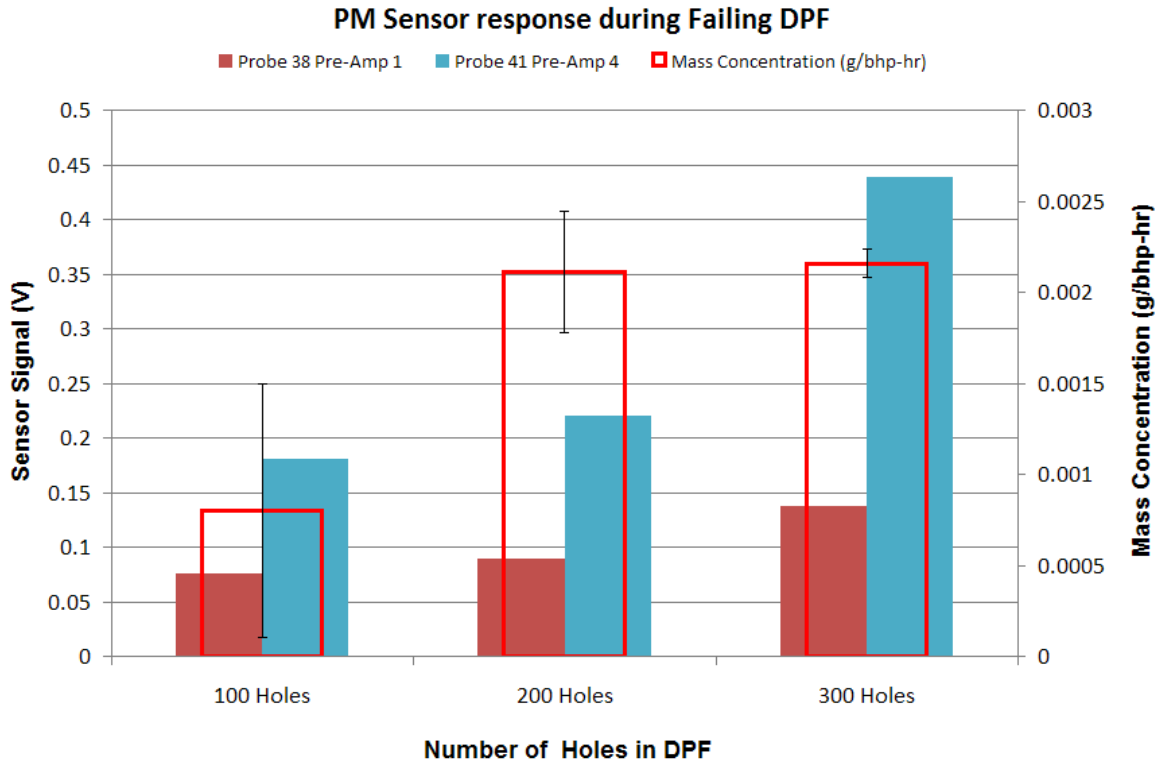


**Figure 4-50. Initial comparison of mass concentration with DPF failure mode**

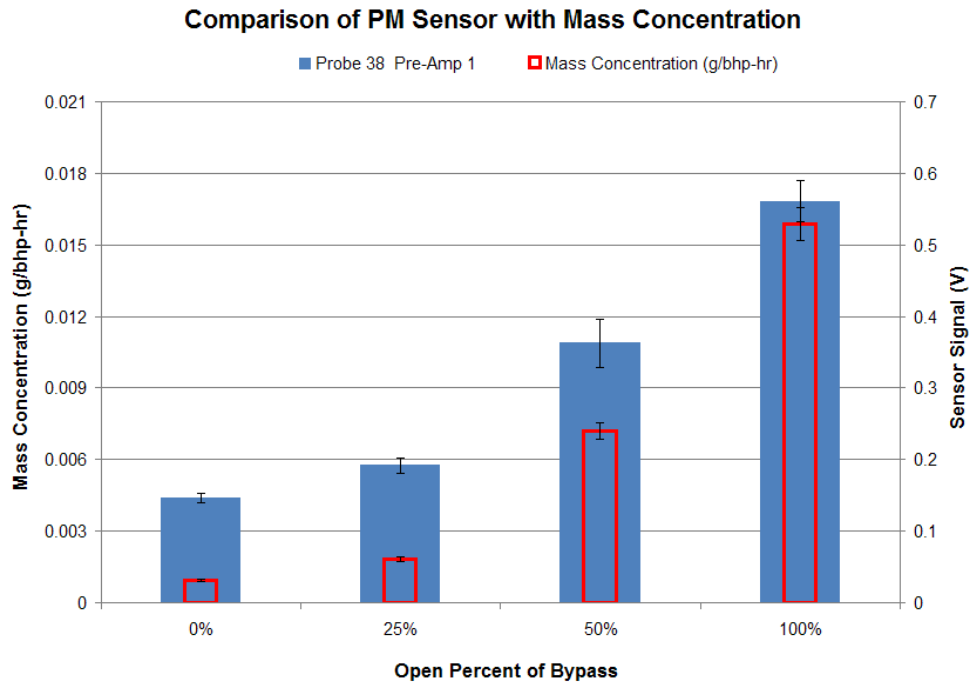


**Figure 4-51. Comparison of PM sensor with bypass opening**

As the DPF failure continued up to 600 holes, testing was continued on the initial engine. The PM sensor response to this increased failure is shown in Figure 4-52, where the corresponding increase in the mass concentration penetrating the DPF is also seen.

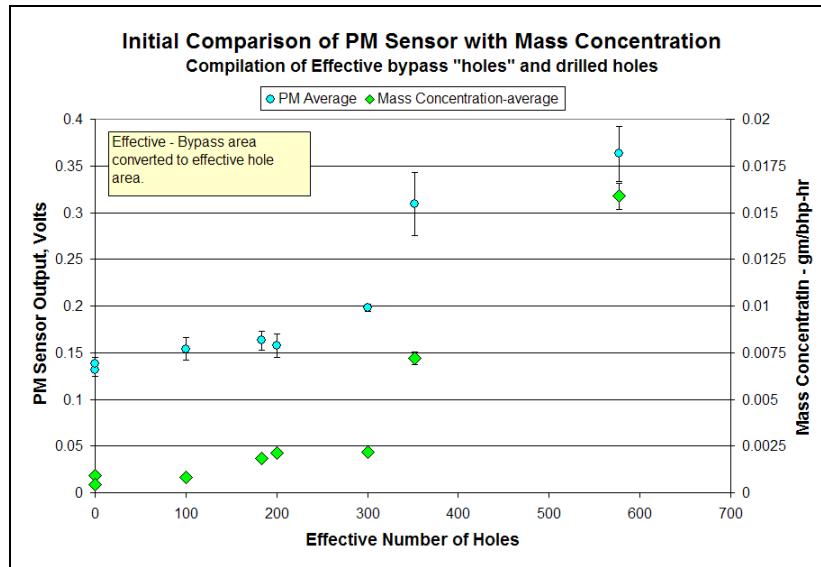


**Figure 4-52. PM sensor response with OBD concentration**

At the stage of the 600 hole failure mode for the DPF, the dynamometer for the Deere engine experienced a catastrophic failure. A second engine and dynamometer were configured to continue the testing, as discussed in section 4.3.1.1. Initial testing with the new configuration appeared to have a drastic effect on the PM sensor's output, as shown in Figure 4-53. With an increasing upstream particle mass concentration, the PM sensor's response appears to have been reduced. Along with this reduction in PM sensor response, the signal-to-noise ratio for the sensors also decreased markedly. The cause in the reduction of the signal noise has two components – the reduction in the signal strength and the increase in the noise levels. The cause of the reduction in the signal strength is not currently understood, and further analysis should be conducted to determine if there are other factors that are contributing this (e.g. changes to the fraction of charged particles). As to the noise increase, other system and sensor factors need to be analyzed (e.g. increased vibration due to the longer exhaust pipe or the potential of increased exhaust pressure pulses on the PM sensor) to determine what other mechanisms may impact the noise than those that were initially considered - see section 4.3.1.2.



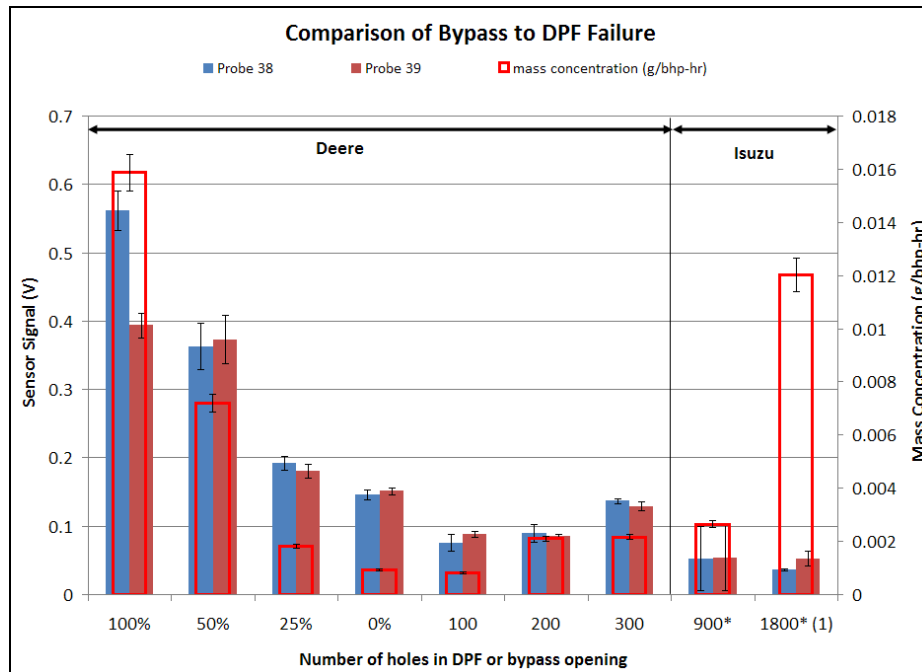


**Figure 4-53. Indication of PM sensor response change using different engine**

#### **4.3.5 Summary of Advanced Frequency Analysis of PM Sensor Data for OBD Diagnostics**

From the results of the experiments conducted on two engines, and the noise issues found during testing on the second engine, additional analysis was conducted to generate a more reliable algorithm for improving the signal obtained from the PM sensor. The test data were analyzed to look for characteristic signatures of the PM sensor output that could be used as a measure of DPF (Diesel Particulate Filter) PM filtration performance and to detect DPF failures in real time.

A number of different methods were explored that included both time-based and frequency-based assessments of the PM sensor output for PM sensor locations upstream and downstream of the DPF; and for the two different engine types that were run. These methods also considered a range of simulated DPF failure levels.

Based on the analysis, two potential algorithms were identified - a time-based and a frequency-based algorithm. In the time-based method, a quantitative determination of when the behavior of the post-DPF sensor approached that of a pre-DPF sensor sufficiently to indicate that the DPF is not functioning would be made. The sensor system would need to only identify when the post-DPF sensor was behaving similar to the pre-DPF sensor. This could be done from the ratio of the slope of the cumulative deviation vs. time, defined as the sum of the absolute value of the voltage deviation from its nominal value.

The frequency-based method is achieved by taking multiple FFTs over a large number of intervals and averaging them. The averages can be compared to each-other over the period of analysis. The advantage of making comparisons using this "spectral energy" approach is that it does not reject any part of the signal and thus does not require pre-knowledge of which frequencies to avoid. This is particularly important when the engine speed changes and would eliminate the need to include the engine speed in the calculations.

Based on the proposed analysis methods, two approaches to using the PM sensor are proposed. One approach would rely on the relative change between the signals obtained upstream and downstream of the DPF. This would require that a threshold of post-DPF-to-pre-DPF sensor signal ratio needs to be established. An OBD fault would be detected, if this threshold ratio is exceeded.

Alternatively, data analysis has indicated that the post-DPF sensor can be differentiated from the pre-DPF sensor by the nature of the respective spectral signal signatures. Integrating the spectral signal signatures can be used to develop a “pre and post DPF fingerprint”, which could also be used to signal an OBD fault.

Further analysis will allow selection between these algorithms and determine further algorithm improvements. A detailed description of the derivation of these analytical methods and the selected final approaches can be found in Section 5.

#### **4.4 Conclusions**

- The electronics designed for the probe proved to function well after the amplification factors were determined. Combined with the initial software for analyzing the signal, the probes were able to detect small mass concentrations during DPF failure modes, down below  $0.01 \text{ g/m}^3$ . The drop in signal when the testing shifted to the second engine is still not thoroughly understood and future analysis with the new signal processing techniques need to be conducted.
- Initial PM sensor evaluation in the post-DPF environment was conducted using a bypass method. The results indicate that the PM sensor can respond at what would be considered a low enough level to be sufficient for OBD detection of DPF faults; namely, proper integration of the sensor with the electronics provided a signal-noise ratio at which the PM sensor could, statistically, differentiate a  $0.010 \text{ g/bhp-hr}$  mass concentration difference.
- Measurements were completed for the PM sensor in the post-DPF environment for multiple failure modes of the DPF and also for bypass measurements on the DPF. The DPF failure modes consisted in drilling an increasing number of holes in the end-cap. Tests on an initial engine indicated PM sensor response matched mass concentration up through the 600 hole mode DPF failure.
- After switching to a second engine, and further failing the DPF, the response of the PM sensors indicated a drastic fall-off in signal. The conclusion from this signal reduction is that there are other frequencies that are adversely impacting the sensor signal. Additional FFT analysis indicates that these signals may have resulted from exhaust structure differences between the two engines.
- There are several variables in the PM sensor response function which are not completely understood at this time, creating a challenge to obtain a consistent and reliable absolute calibration equation and correlation between the measured PM level and the sensor response. As a result, a single sensor located post-DPF solution does not look promising at this time without significantly more basic science and calibration efforts. In addition, the PM sensor is now capable of measurement over extended time periods without mechanical failure. Initial noise pickup of the cable can still be a limiting factor for the signal-noise ratio.

- A two-sensor solution seems more promising and should be pursued. This approach relies on the relative change between the signals obtained upstream and downstream of the DPF. This approach would require that a threshold be established so when the post-DPF-to-pre-DPF sensor ratio exceeds this threshold, an OBD fault would be detected. The basic concept is qualitatively expressed as “when the post-DPF sensor signal can be identified as having exceeded the threshold, and thus is sufficiently similar to the pre-DPF signal, that the DPF has failed in a substantial way.” Alternatively, data analysis has indicated that the post-DPF sensor can be differentiated from the pre-DPF signal by the nature of the spectral- and time-based signals themselves as well as their integrated signals. These differences can be further explored to develop a “fingerprint” that could be recognized as pre- or post-DPF in nature. This may be a more costly approach, but the increase would be primarily with the cost of the sensor itself, as the electronics and signal processing portion of the sensor cost may be similar.
- Two relative pre-DPF to post-DPF algorithms have been identified—a time-based and a frequency-based algorithm. Further analysis will indicate if the calculations need to be “tweaked” or modified to improve their performance. Two sensors could be correlated in such a way that the post-DPF sensor’s output signal can be represented as an electronic ratio or sum difference to the pre-DPF sensor’s signal (or vice-versa), where perhaps they share a common ground or some other electronic coupling. The benefit of this would be to evaluate upstream and downstream sensor responses for the same upstream changes.
- The “discrete voltage” characteristic of the PM sensor could be investigated further to better understand and determine if it is truly beneficial. It may be possible to use discrete voltage filtering to improve the correlation to PM by, for example, using the Cumulative Deviation and excluding voltages which are below a certain “noise” threshold; or using the squared deviation. If it were determined that the discrete characteristics were not advantageous, then adding electrical capacitance may create an electrical smoothing, producing a more continuous signal.
- A more basic understanding of the charge fraction on the exhaust particles is needed to recognize the nature and cause of the propensity for high signals at the integer multiples of the engine cycle frequency. At present this propensity is overcome by the integral methods of the two algorithms, as discussed in section 4.3.5 and section 5 (Appendix).
- In its current configuration, the PM sensor is sensitive to vibration, for which spectral filtering may make sense. The impact of vibration has highlighted issues in how the sensor was fabricated and the modification of signal-noise during the sensor operation.
- At present, a coarse “failure detection” scheme seems promising. This implies that response to a particular sensor output will indicate that a certain OBD threshold level has been achieved. The sensor would not be required to determine lower level mass concentration penetrations through the DPF, i.e. a wide-band sensor response. This is suggested by the fact that the pre-DPF signal changed during the different tests despite all the nominal operating conditions remaining the same. This indicates that day-to-day, fuel-to-fuel, engine-to-engine variations may be significant to the sensor response and underscores the benefits of the relative sensing methods. It is believed that with a nonlinear calibration, a DPF efficiency calculation may be possible. If a threshold value can be established for the ratio of pre-DPF to post-DPF sensors, this value might be associated with the OBD threshold level.

#### 4.4.1 Recommendations and Next Steps

The purpose of this project was to determine if the PM sensor has the potential to detect DPF failures and, if so, what algorithm and sensor configurations might be required. As a result, the most promising programmatic path forward has been identified for the development and use of the sensor as an onboard diagnostic device. Based on this analysis and the examination of the experimental observations made during testing of the sensor, we make the following recommendations for the program going forward:

1. **Use of Relative Sensor Measurement**—Use two sensors installed pre-DPF and post-DPF and a relative measurement algorithm to compare the post-DPF signal to the pre-DPF signal.
2. **Use of a Threshold Level to Trigger**—Use a threshold value to trigger the OBD indicator that the post-DPF sensor signal has come “sufficiently close” to the pre-DPF sensor signal level to indicate a DPF failure. This method could be used to detect filters with a failure level above the OBD threshold level but would not be capable of discerning absolute levels below that threshold level.
3. **Down Select the Best Processing Algorithm**—Two diagnostic pre-DPF to post-DPF algorithms have been identified: *Time-Based Cumulative Deviation* and *Frequency-Based Cumulative Spectral Energy*. These algorithms provide signal conditioning aspects that improve the detection of a mass concentration by the PM sensor. These algorithms can be used with the two-sensor approach to detect a DPF failure. Additional experimental data should be taken to validate these algorithms, determine the relative merit for detecting DPF failure at the level of concern and for selecting the optimum algorithm.
4. **Calibrate Sensor Off-Engine**—After switching to a relative measurement scheme as identified above, it may be possible to develop a **DPF Filtration Efficiency** sensing capability if a nonlinear sensor voltage-to-PM-level calibration is determined. We recommend that initially this calibration level be determined off-engine.

To use two sensors, the output of interest—DPF effectiveness or failure—can be determined through the use of the identified algorithms with the PM sensor signals and the relative comparison of the post-DPF signal to the pre-DPF signal. This approach has the best chance of accommodating the many possible changes in the PM signal which might be encountered. The idea is that both sensors would be exposed to whatever effects are due to the particular engine or operation conditions and allow for a relative comparison between the two sensors, with the assumption that the differences can be associated and isolated to the effects of the DPF. The pre-DPF signal then acts as a “floating reference”

Additional testing should also be conducted on different types and classes of engines. From the differences seen in this project, an understanding of both the relationship between the charge and particle mass as well as the influence of potentially different charging mechanisms of the different engines on the PM sensor response needs to be determined.

The next steps for this sensor system will be to review the external competition for particle mass sensing of DPF failure modes and to look for funding to determine a complete understanding of the charging process in the exhaust and the impact of the DPF on the charge distributions of particles penetrating a failed DPF.

## **4.5 Commercialization**

The goal of the ICAT program “Demonstration of Particulate Matter (PM) Sensor in post-DPF Environment” was to validate the PM sensor performance for OBD threshold compliance and to further the technology readiness level to enable future commercialization. Based upon the findings of the conducted research, summarized in the conclusions section of this report, it appears that the PM sensor technology is not at the present time at a technology readiness level to allow commercialization.

As shown in this report, the post-DPF sensor signal can be qualitatively and quantitatively distinguished from the pre-DPF sensor signal, and thus a relative PM sensor approach holds promise as an OBD sensor solution to detect DPF failures.

## **5. Appendix**

### **5.1.1 *Summary of Advanced Frequency Analysis of PM Sensor Data for OBD Diagnostics***

The objective of this program was to determine if the Honeywell PM sensor can be used to detect DPF failure and to generate a reliable algorithm to implement into an OBD device for this purpose.

To achieve this objective, extensive on-engine testing was conducted at the University of Minnesota generating a large volume of data from two diesel engines: a four-cylinder Deere and a four-cylinder Isuzu engine. These data were analyzed to look for characteristic signatures of the PM sensor output that could be used as a measure of DPF (Diesel Particulate Filter) PM filtration performance and to detect DPF failures in real time.

With this in mind, several methods were explored that included both time-based and frequency-based assessments of the PM sensor output for various PM sensor locations (upstream of DPF, downstream of DPF) and for two different engines, a range of soot Particulate Matter (PM) concentration levels, and a range of simulated DPF failure levels (holes were created in the DPF matrix to simulate degrees of DPF failure).

From this analysis, two preliminary ideas were evaluated that hold promise as potential algorithms/methodologies for using the PM sensor to detect DPF failure within an onboard diagnostic system.

#### **5.1.2 *Test Data Overview***

The experimental data were generated on two engines over a range of engine speeds and loads and for a range of simulated DPF failures. Additionally, data were generated and analyzed for simulated vibration conditions. Only a subset of the data was explored in depth using spectral analysis and close inspection of the time-based data traces.

#### **5.1.3 *PM Signal Overview***

The time-based PM sensor signal was sampled at a rate of 1 sample per millisecond or 1000 samples per second (Hz). Initially, the analysis focused on the data generated on the second of two engines, the Isuzu engine, with two different DPF failure modes: (a) 900 holes and (b) 1800 holes in the DPF end cap and the nominal operating condition of 1550 RPM at 350 and 360 Nm torque (load), respectively.

Two PM sensor locations were examined, one with the PM sensor located upstream of the DPF, which is exposed to the exhaust and PM levels directly out of the engine; and the second PM sensor, the post-DPF sensor, located downstream of the DPF and exposed to the PM levels after the DPF. These locations can be seen in Figure 5-1.

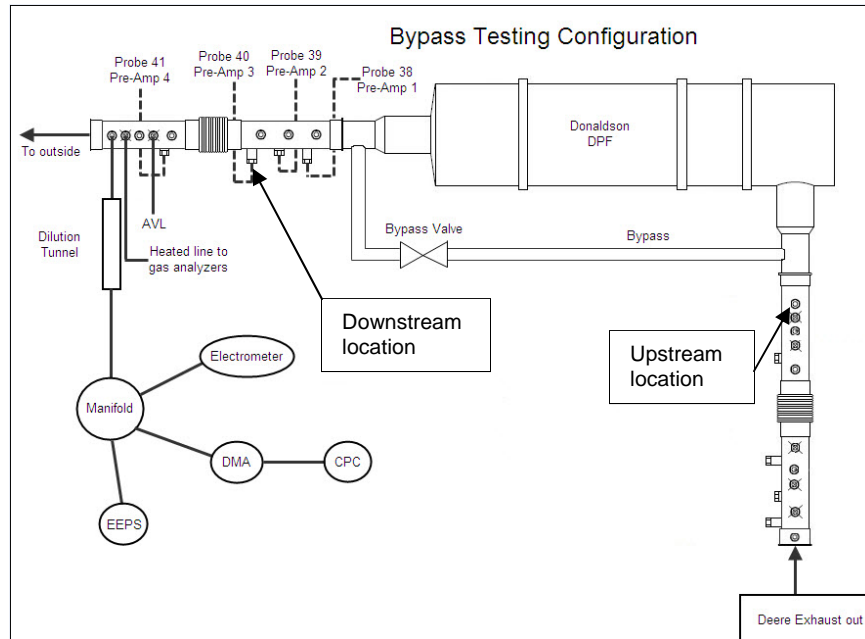


**Figure 5-1. Sensor configuration relative to DPF for Isuzu engine**

The data analysis in this report used roughly 4 sec worth of data at a time ( $2^{12} = 4096$  msec), where the 12<sup>th</sup> power of two data points is ideal for FFT evaluations. Each 4096 set of data points represents a 4-sec block or interval.

#### 5.1.3.1 Downstream/Post-DPF Sensor

**Time Trace Signal**—First, the post-DPF sensor signal when the DPF had 900 holes was examined (see Figure 5-2). For reference, a wave function was synthesized to represent a pure cosine wave with three pure frequencies. The synthetic signal was a wave function (shown as blue dots in the figure) constructed from 3 cosine functions having 1x, 2x, 3x the engine cycle frequency (ECF), which for this case provided an ECF = (1550 rev/min) / (60 sec per min) = 25.833 Hz (2x=51.7 Hz and 3x=77.5 Hz). This function was, by definition, a continuous function of time, but it was “sampled” discretely at the same intervals as the PM sensor signal.

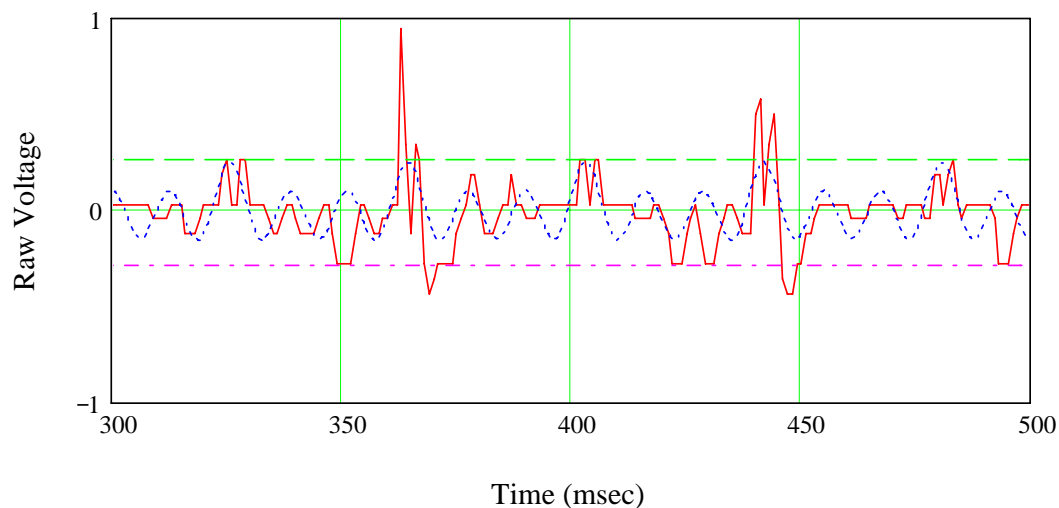


**Figure 5-2. PM signal (ch4 #40) for 900 holes 10-8-09 with 1x, 2x, 3x ECF wave overlay including reference lines at 0.265 (green) and -0.285 (pink).**

The synthetic wave is shifted to line up with the peak at about 370 msec, and due to the 1xECF harmonic in the data, the synthetic signal lines up again at ~410 msec, again at ~440 msec, etc. This helps to see the 1xECF nature of the PM sensor signal. With this wave superimposed, the PM signal (red solid) can be readily seen to have at least this harmonic content—at every engine revolution there is a “burst” of activity. The importance of this can be seen in the frequency analysis in Figure 5-3. It can also be seen that with every other burst being larger in amplitude, a  $\frac{1}{2}$  ECF harmonic is also evident in this time trace. Note that significant frequency amplitude would expect to be seen at twice the engine frequency (2xECF), since this is the frequency of the exhaust gas pulses in a four-cylinder, four-stroke engine. Close inspection of the time trace above confirms that this 2xECF harmonic was indeed evident. From this qualitative review of the time trace above, it can be seen that much of the PM sensor signal has ECF harmonics, and this is important to keep in mind as the different algorithms are reviewed.

To aid in the discussion, “activity” will be defined as a qualitative assessment of the magnitude and frequency of the PM sensor signal when either positive or negative deviation from the “rest state” or nominal is seen. Regular periods of “non-activity” are seen in Figure 5-2 where the signal returns to its nominal value, followed by both positive and negative deviations from this value of varying magnitudes. Thus, “activity” or “energetic” are terms that can be used to identify visually the deviation of the PM voltage from its nominal value, which here is 0.03 volts. Two such deviations are noted in the figure with green horizontal dashed lines at +0.265, which is a positive deviation of +0.235 after subtracting off the 0.03 nominal value, and a pink horizontal dashed line at -0.285. While further investigation is needed, inspection of the current data indicates the existence of common discrete levels of non-nominal voltages.

It is evident from the data, and qualitatively in Figure 5-2, that the activity of the PM sensor signal, especially at low PM levels, has a somewhat “digital” or “gear-toothed” characteristic within the signal of varying duration and deviation. What appears more often than not is a set of common values (which are not easily associated with round-off issues). Indeed, an analysis of the signal reveals that the voltage is both positive and negative and is not normally distributed. There are a few discrete voltages that are frequent with many gaps between them, as can be seen in Figure 5-3. To avoid confusion, the term “probability” will be used for the likelihood or probability of a particular voltage occurring, and the term “frequency” will be used for frequency analysis only.

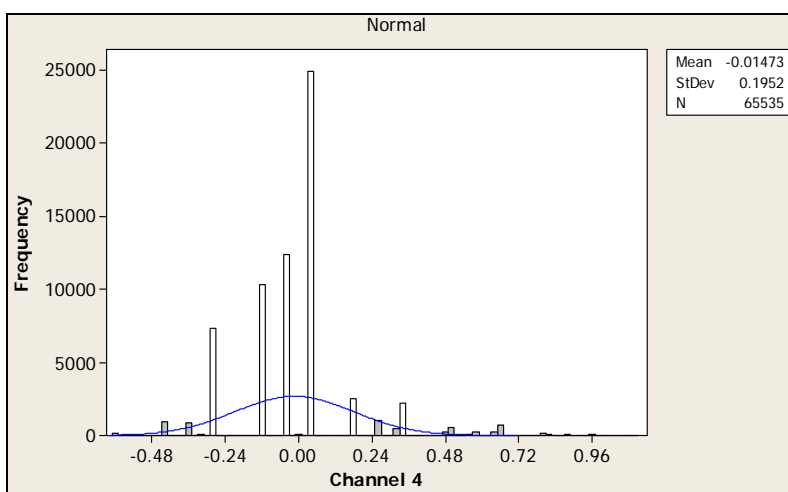


**Figure 5-3. Histogram of the probability (y axis) of a particular voltage from Ch4 – post-DPF sensor 10-8-09 900 holes. Note the “discrete” rather than continuous nature of the probability distribution.**



When the probability distribution between the PM sensor signal and the synthesized cosine signal were compared, this point became clearer as shown in Figure 5-4. Here it can be readily seen that the post-DPF PM sensor signal on the left has “gaps” between discrete voltages, while the continuous signal created by sampling the synthesized cosine function, mentioned above, at the same sampling rate as the data indicates a bimodal distribution without any zero probability gaps in the distribution. The same bins were used for both graphs, and inspection of the actual voltages reveals this distribution was not due to round-off or truncation. From the figure, note that a continuous signal, even when sampled at 1 msec, will produce a “filled” probability function that does not have discernible gaps; while the PM sensor signal clearly does have discernible gaps or voltages that have zero probability.

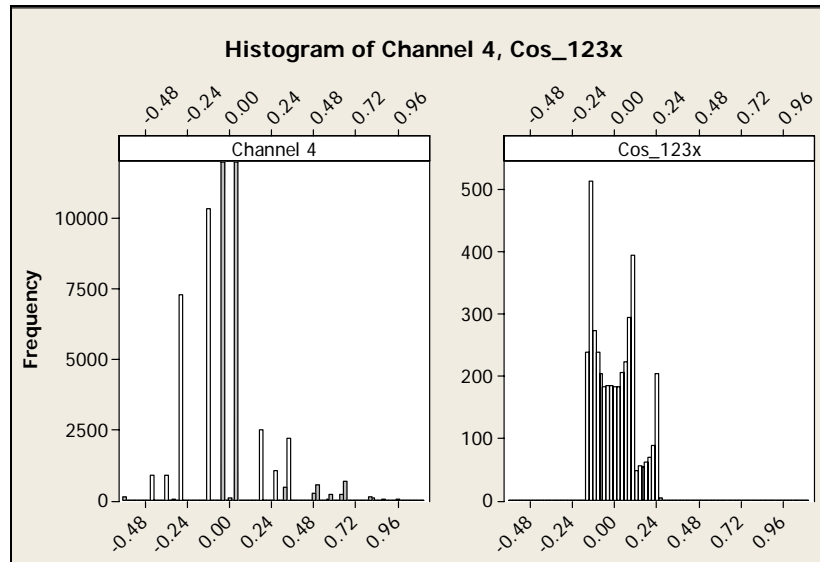


**Figure 5-4. Side-by-side comparison of the post-DPF PM sensor signal and the synthesized cosine function with 1x,2x, 3x ECF wave.**

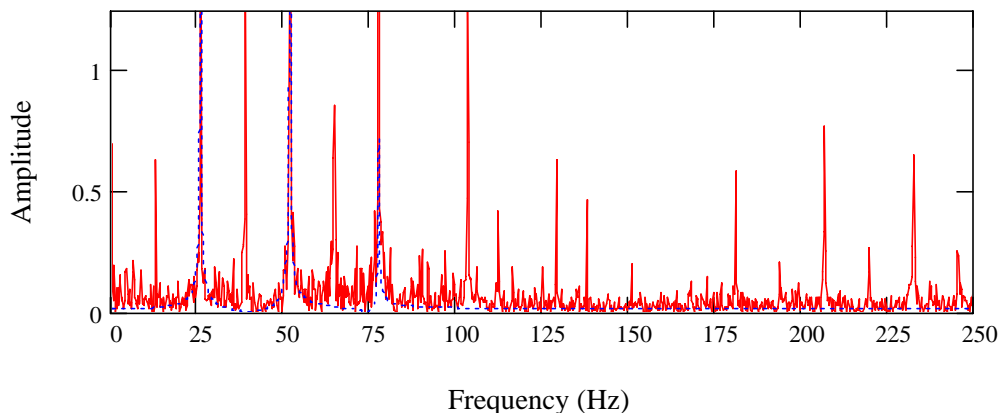


**Figure 5-5. Spectral analysis of the PM sensor signal downstream of the DPF**

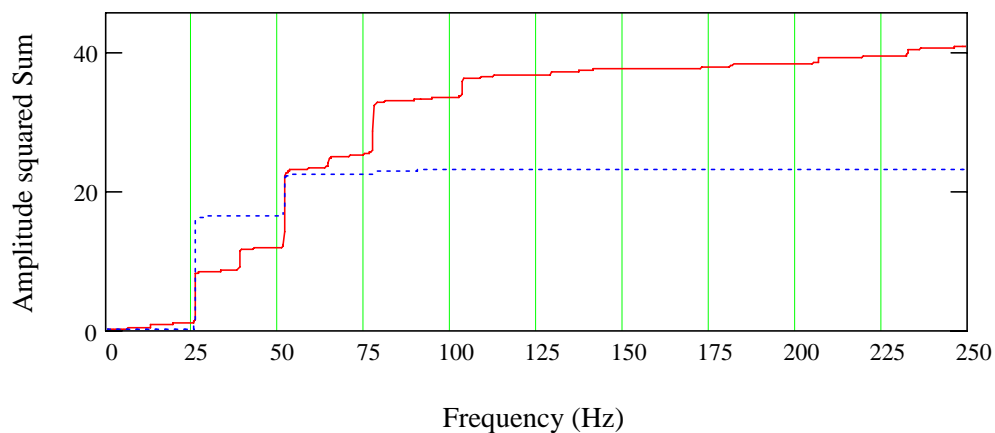
**Harmonic Content and Frequency Analysis**—Next the harmonic content of the PM sensor signal was explored and compared to the reference synthesized cosine signal.

Figure 5-6 shows the integrated FFT spectrum of the signal shown in Figure 5-2. As a check, the reference cosine function was similarly analyzed. With the reference signal superimposed on the spectral distribution, a dashed blue line indicates the primary 1x, 2x, 3x ECF harmonics

and the red line indicates the three key frequencies ( $1x = 25.8$  Hz,  $2x = 51.7$  Hz,  $3x = 77.5$  Hz). The FFT used  $2^{12}$  or 4096 samples, which represents about 4 sec for each interval of 5 to 10 min in the steady state data log file. The Nyquist cut-off frequency for 1-msec sampling time is 500 Hz, and the PM sensor has a low frequency bandpass filter diminishing frequencies above 200 Hz

Note that the PM signal contains high-amplitude harmonics at each of the three multiples of the engine cycle frequency (25, 51.7, 77.5 Hz), as well as at  $\frac{1}{2}$ ,  $1\frac{1}{2}$ , and  $2\frac{1}{2}$  multiples of the ECF. This propensity for the harmonics to be integer and fractional multiples of the engine cycle frequency is an important feature of the PM signal.

An additional way to review the harmonic content of the signal is to take the *cumulative sum of the square of the frequency spectrum* that was shown Figure 5-5. This enables the relative degree of harmonic content at and between the key ECF frequencies to be determined. This “cumulative spectral energy” graph, shown in Figure 5-6, clearly indicates discrete jumps in spectral energy at the ECFs identified earlier. For reference, the synthesized cosine function is included and discrete steps at  $1x$ ,  $2x$ , and  $3x$  ECF are also indicated. The nature of the apparent “staircase” of discrete steps in the red curve indicates that there is not much spectral energy between the ECF steps.



**Figure 5-6. Cumulative spectral energy graph: post-DPF 10-8-09, 900 holes PM sensor (red), synthesized function (blue)**

Keeping post-DPF signal firmly in mind, the pre-DPF signal can be examined, keeping in mind that the pre-DPF signal is from the exhaust at the output from the engine while the post-DPF signal is from the exhaust gas that has passed through the DPF. In this case, the DPF has 900 holes in it to simulate a certain degree of DPF failure. The task is to develop a diagnostic algorithm that can differentiate the post-DPF signal from the pre-DPF signal, quantify this difference, and provide a quantitative indication of the degree to which the post-DPF signal resembles the pre-DPF signal. This discernable and quantifiable difference between post-DPF and pre-DPF signals can potentially be used, at a minimum, to determine whether the DPF has failed and ideally to identify and quantify intermediate degrees of failure that could be tracked for trends. As a secondary goal, such a comparison may provide a metric qualitatively similar to that of DPF efficiency, however this would not be a requirement of a successful algorithm for detecting a more significant and perhaps more sudden failure of the DPF.

**Engine-Out/Pre-DPF Sensor Signal**—The time trace of a sensor (#40) located upstream of the DPF (seen in the lower right of Figure 5-1) is shown in Figure 5-7 with the synthetic wave signal superimposed for reference. In this case, the PM sensor signal is seen qualitatively to be more “energetic” or “active,” by which is meant the sensor signal spends more time at non-nominal

values and the degree of deviation is greater. A similar discrete value behavior is seen in this signal at values similar to the post-DPF signal (positive = 0.235, negative = -0.238, nominal = 0.03). This observation is supported by the voltage probability distribution shown in Figure 5-8. Here a wider distribution is seen than that from the post-DPF signal, specifically at the higher probability of larger negative values, however, the frequency gaps still remain.

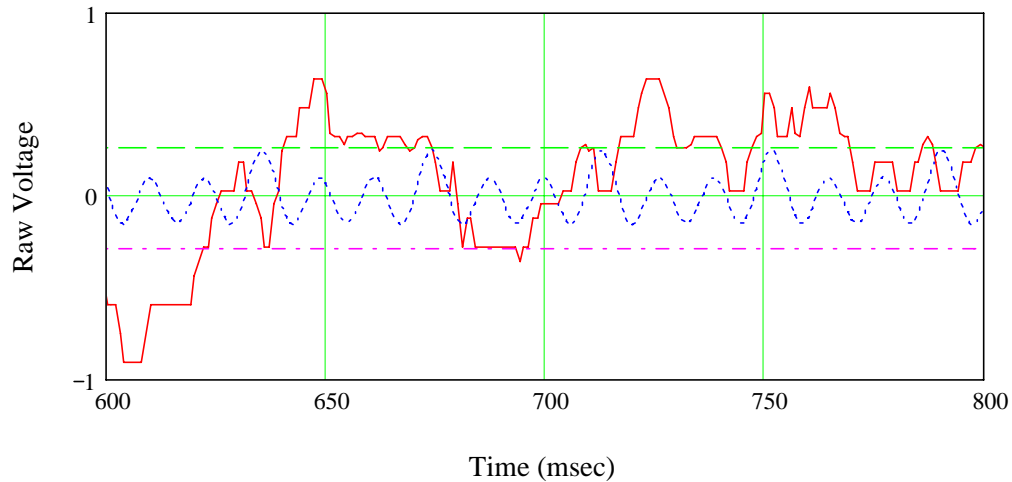


**Figure 5-7. Engine-out PM signal (Ch3 Probe 40) 900 holes**

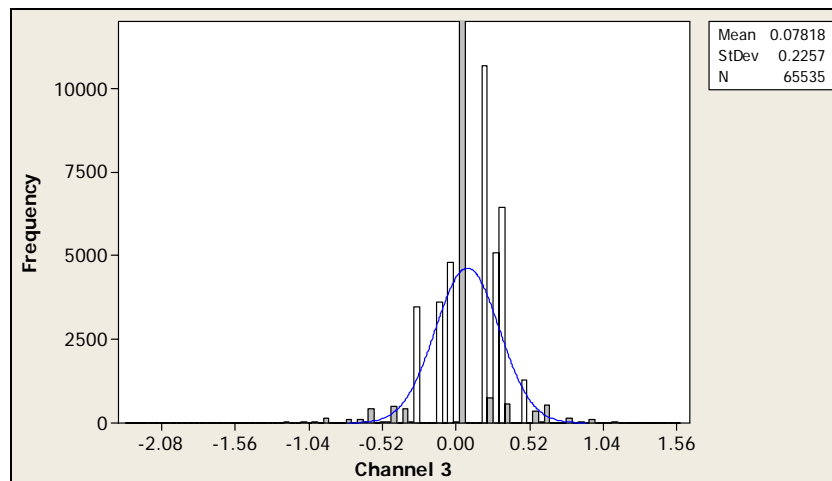


**Figure 5-8. Voltage probability distribution for Ch3 Probe 40 - pre-DPF, 900 holes**

Figure 5-9 shows the spectral response of a PM sensor in the pre-DPF position. The ECF harmonics at 2x and 3x are seen, but no harmonic signal is present at the discrete frequency of 1x ECF (25.8 Hz). In addition, a very different pattern having a large amount of harmonic content below 1x ECF is seen, which is broadband in nature, not having a distinct harmonic. Figure 5-10 underscores this by indicating smoother, more continuous increases in spectral energy and less well defined discrete staircase steps, especially below  $\frac{1}{2}$  ECF ( $\sim 12$  Hz). While not obvious from Figure 5-9, there is a discrete harmonic at the  $\frac{1}{2}$  ECF mark but clearly not one at the 1x mark. Again, the spectral distribution is dominated more by broader bands and less by discrete ECFs. These qualitative differences between the sensor response before and after the DPF will be compared next.

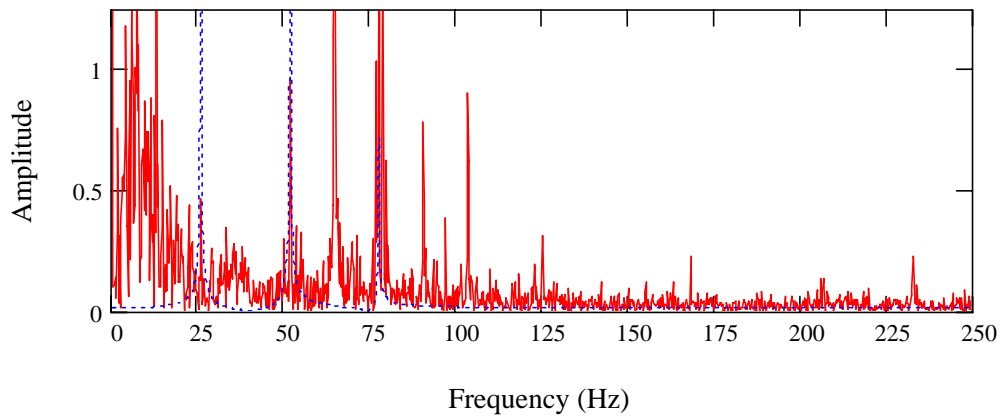


**Figure 5-9. Frequency spectrum pre-DPF, Ch3 Probe 40 900 holes**

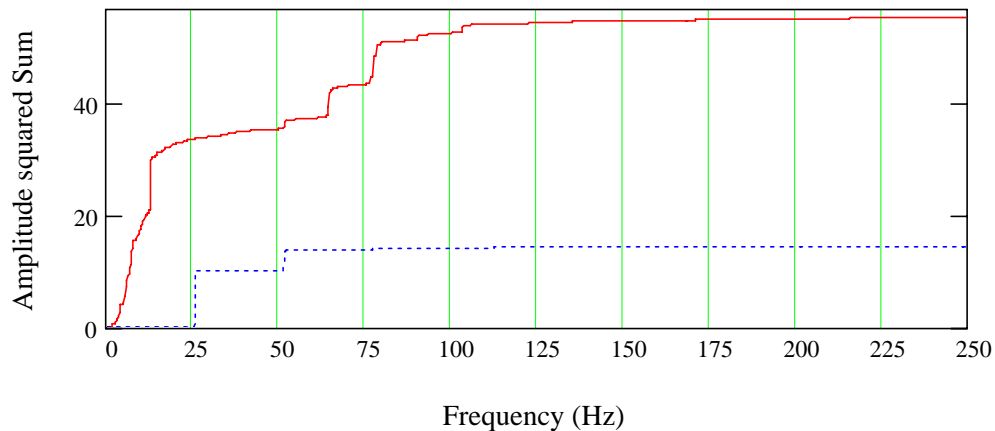


**Figure 5-10. Cumulative Spectral Energy pre-DPF, Ch3 Probe 40 900 holes, 10-8-09**

**Comparing Pre-DPF with Post-DPF PM Sensor Signals**—The first comparison between pre-DPF and post-DPF signals was made by overlaying the two time traces and indicating qualitative differences.

**Time Traces**—Figure 5-11 shows that the pre-DPF signal (red) is not dominated by discrete ECF components but rather exhibits a steady stream of positive and negative deviations with occasional one-sided peaks (one-sided meaning the peak is either positive or negative, but does not rapidly switch from positive to negative in a single event). A deviation may be simply viewed as the absolute magnitude of the difference between the PM sensor voltage and the nominal “inactive” voltage, which in this case is 0.03 volts zero offset.

In contrast, the post-DPF signal (blue) is seen to be dominated by the 1x ECF and  $\frac{1}{2}$ x ECF spikes (a  $\frac{1}{2}$ x signal is just a 1x signal having every other event be a large spike rather than every event) while having more occasional deviations from the nominal value. Also note that the post-DPF peaks generally tend to hit both positive and negative values and have a “spike”-like quality, while the peaks in the pre-DPF curve generally are one-sided deviations. As a final observation, the pre-DPF signal has much more general activity with less pronounced and less frequent spikes. In contrast, the post-DPF signal is fairly weak between the spikes.

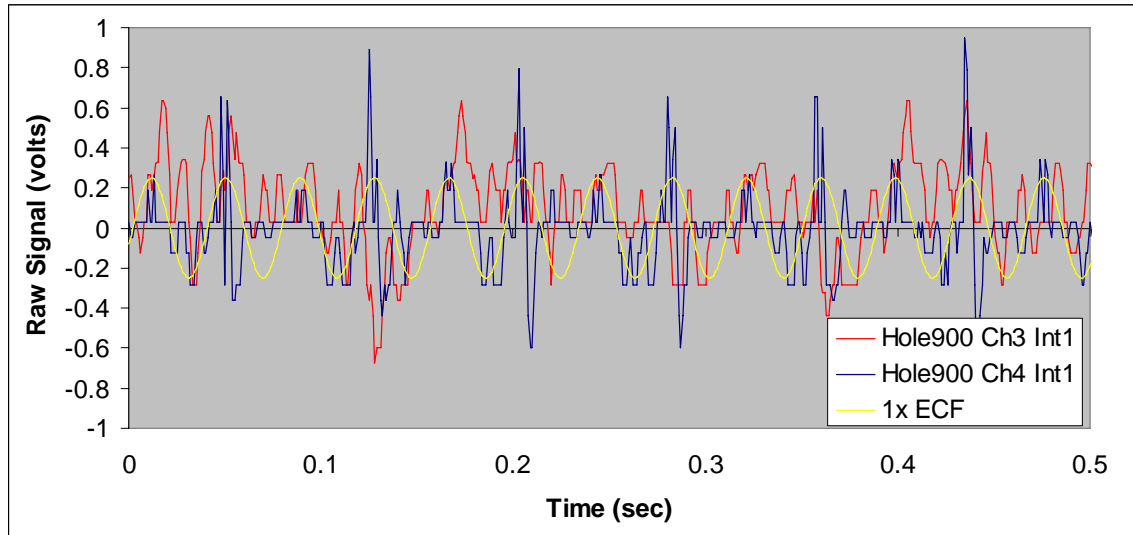


**Figure 5-11. Direct comparison of the pre-DPF (red) Ch3 and post-DPF (blue) Ch4 for 900 holes, 10-8-09. The reference signal with only 1xECF is shown in yellow.**

**Probability Distributions**—The respective probability distributions are compared, in Figure 5-12, with the pre-DPF (Ch3) distribution on the right and post-DPF (Ch4) distributions on the left. The pre-DPF signal has a larger standard deviation. Close inspection reveals the larger range in the distribution of Ch3 with negative values spanning to nearly -2, while negative values for the post-DPF, Ch4, not going much beyond -0.52. These observations are clarified confirmed when the two probability distributions are overlaid, as in Figure 5-13. Here the broader distribution of the pre-DPF signal (red, Ch3) is seen.

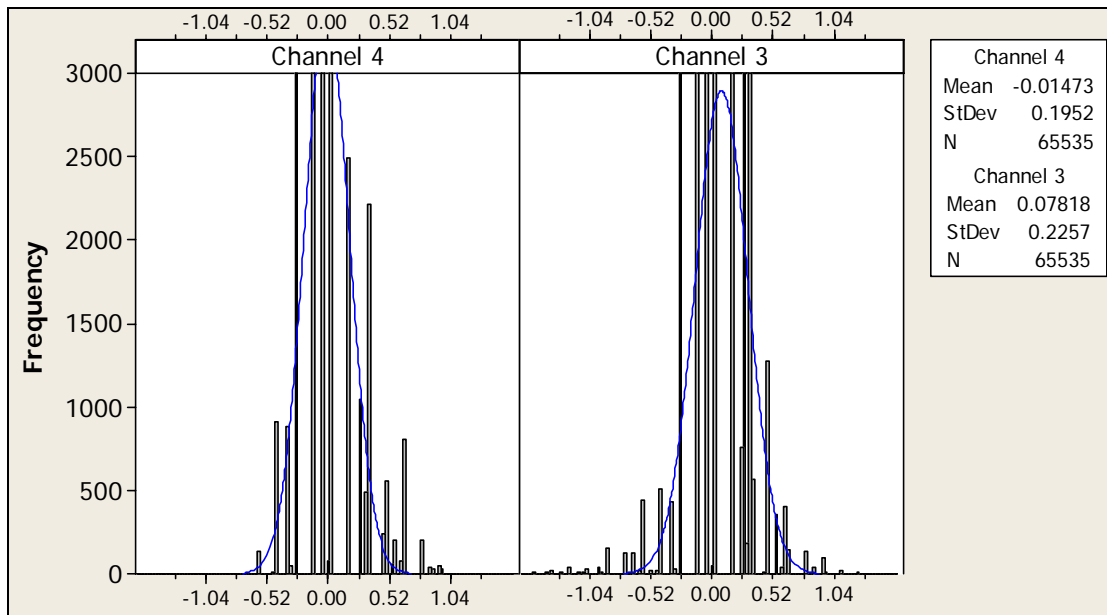


**Figure 5-12. Side-by-side comparison with zoom of Ch4-Probe 405 post-DPF sensor and Ch3-Probe 40 pre-DPF sensor for 900 holes**

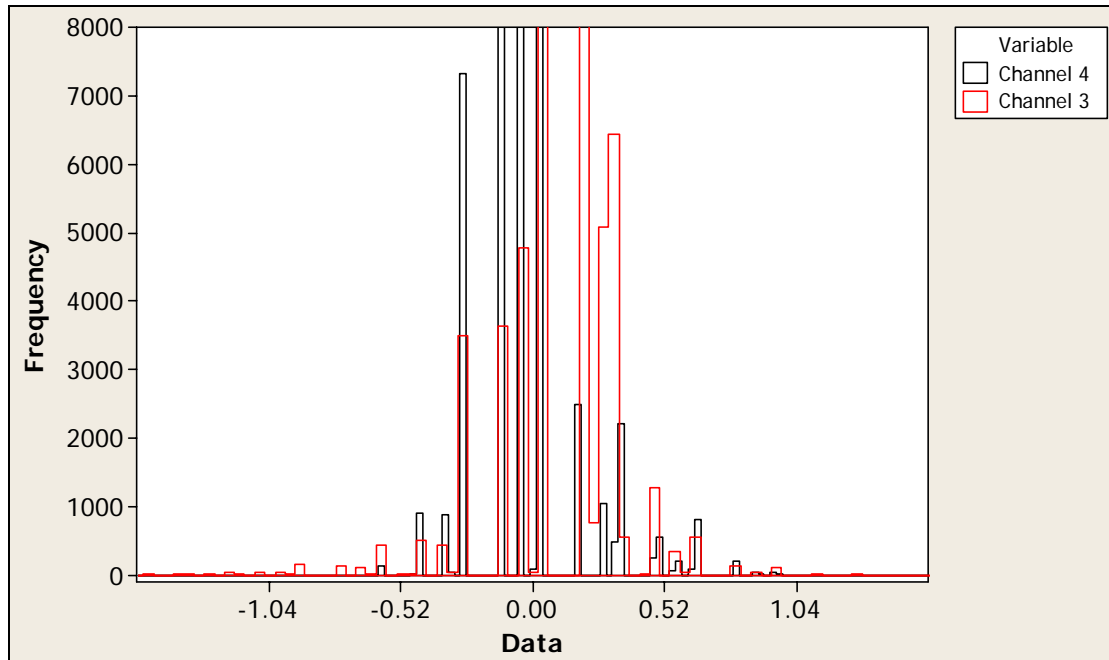


**Figure 5-13. Zoomed in overlay of Ch3 (pre-DPF, red) on Ch4 (post-DPF, black) showing the wider distribution of the pre-DPF sensor and the higher probability of lower deviation (large bars close to zero)**

**Frequency Distributions**—A third method for comparing pre-DPF to post-DPF sensor signals considers taking multiple FFTs over a large number of intervals, collecting them together, and then producing an ensemble (e.g., by frequency) average. The ensemble averages can then be compared to one another.

Figure 5-14 shows two FFTs for Ch4 (post-DPF) and Figure 5-15 shows two for Ch3 (pre-DPF). The averages are plotted together in Figure 5-16., where the differences in the frequency spectra can be clearly seen. Note that large differences between the two spectra are evident for the ECF spikes and between 0 and 1x and 1x and 2x ECF, with perhaps a little deviation between 2x and 3x ECF, and that the differences are largest at low frequencies and diminish as the frequency increases.

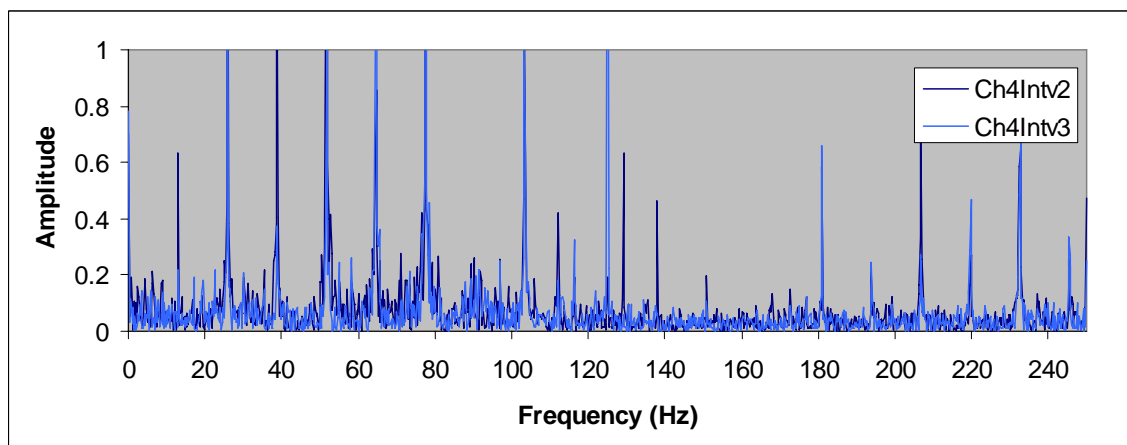


**Figure 5-14. FFT for Ch4 downstream—intervals 2 and 3**

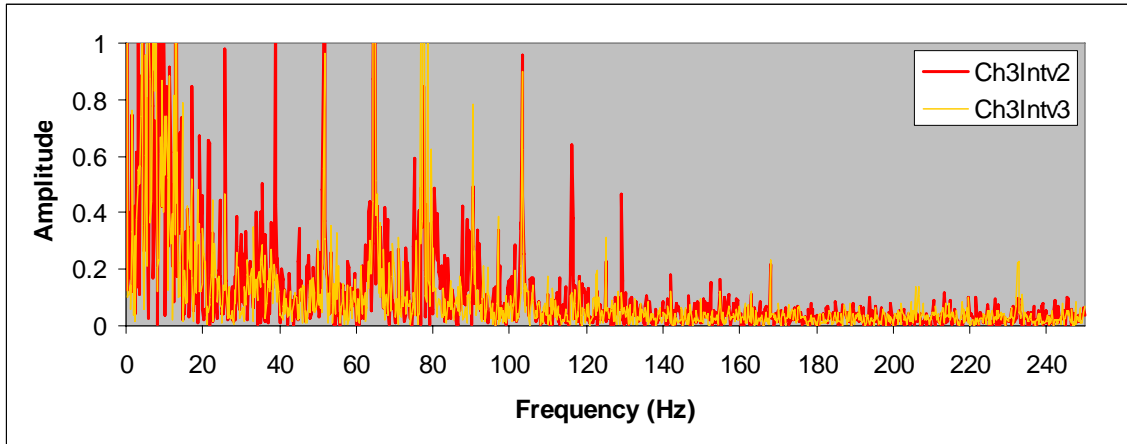


**Figure 5-15. FFT for Ch3 upstream—intervals 2 and 3**

The spectral energy of the averaged FFTs can also be compared directly as in Figure 5-16, where the pre-DPF cumulative spectral energy (red Ch3) can be seen to grow rapidly for frequencies below 1x ECF (<26 Hz), to a maximum value of 43.7. The post-DPF sensor (blue Ch4) is seen to have very little spectral energy below the 1x ECF point, but also grows by discrete steps to a final value of 18.7.

The advantage of making comparisons using the spectral energy approach is that no part of the signal is rejected and pre-knowledge of which frequencies (especially the engine cycle frequency) to avoid is not required. This is particularly important when the engine speed changes and would eliminate the need to include the engine speed in the calculations. Moreover, if the charge from the combustion process is deposited in some part of the exhaust system, this charge may be aperiodically released due to either particle buildup or charge transfer from particle impact. This accumulated charge will then pass the sensor, causing a response quite different from the normal variation in charge.

It can be readily seen that these diagnostics can be applied for the pre-DPF and post-DPF signals and that the two signals can be differentiated. In Figure 5-16, the pre-DPF spectra show a higher broad amplitude band below the first ECF marker at 26 Hz and are consistently higher between the spikes than the post-DPF spectrum.

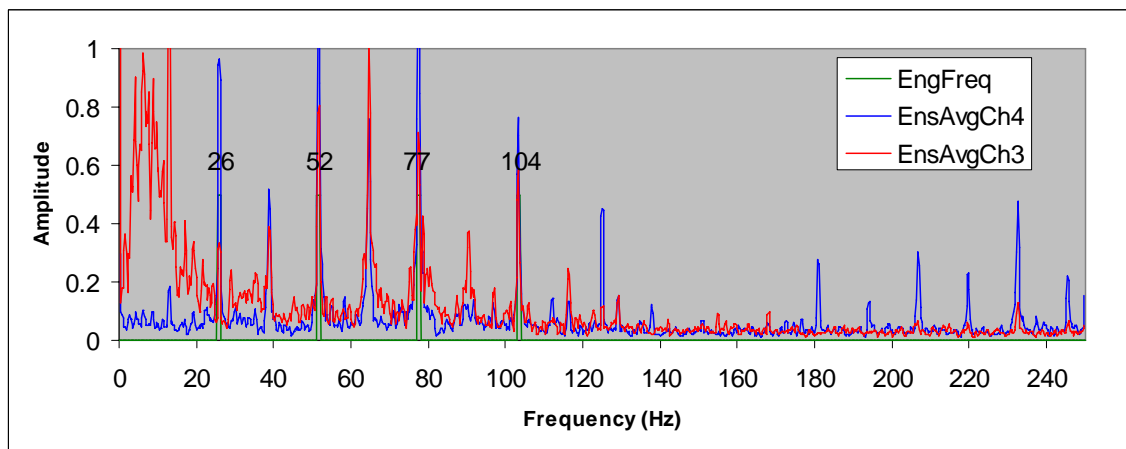


**Figure 5-16. Comparison of ensemble-smoothed FFTs for Ch3 and Ch4 (intervals 2 and 3) with engine cycle frequency and its multiples (green)**

In Figure 5-17, the total cumulative spectral energy from the averages is 43.7 for the pre-DPF sensor, while the post-DPF sensor reaches 18.7.

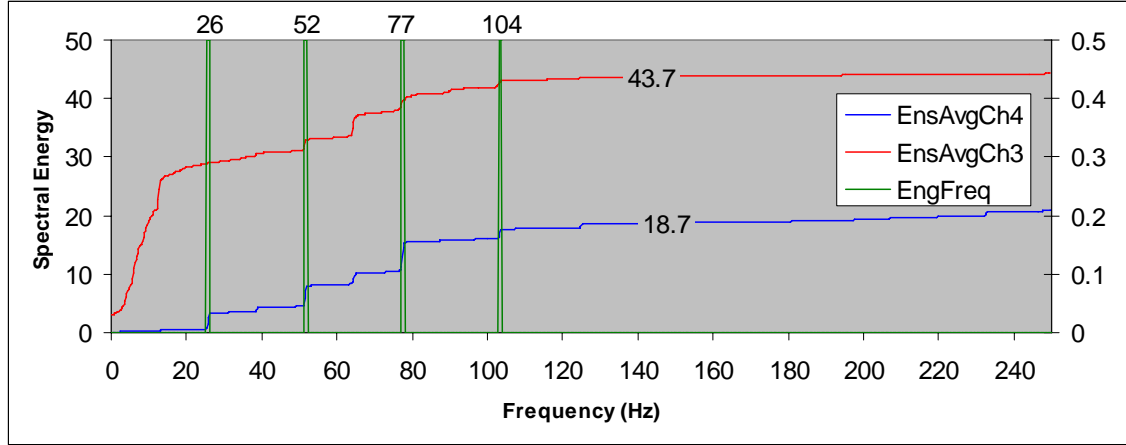


Figure 5-17. Spectral energy for pre-DPF and post-DPF spectra

**Methods for Detecting DPF Failure**—Based upon the observations of the nature of the time traces and the spectral frequency distribution, promising diagnostics for detection of DPF failure were identified.

**Method A: Time-Based Signal Processing – Cumulative Deviation**—In this method, the time domain signal is analyzed to determine when the PM sensor is experiencing a large PM charge. During this period, a higher “activity” is exhibited, as seen in Figure 5-10. This difference in “activity” was confirmed by the probability distributions in Figure 5-11 and Figure 5-12, which indicated that the pre-DPF signal deviated from the nominal for longer periods of time and the deviations were larger than for the post-DPF signal. Moreover, the activity seemed to be both positive and negative. Additionally it was observed that when “at rest,” the PM sensor voltage may not be zero. From these data, a nominal “at rest” value of 0.03 volts has generally been seen. Including the considerations of this observation the diagnostic of “Cumulative Deviation,” was defined.

A suitable expression for the qualitative statement “activity” might be the quantitative formula for the Cumulative Deviation, defined as the sum of the absolute value of the deviation of the voltage from the nominal according to:

$$CumDev = \sum_{k=t-\Delta t}^t [V_k - V_o] \quad (1)$$

where

CumDev = the Cumulative Deviation from the nominal value,  $V_o$   
 $k$  = the data vector storage index  
 $t$  = the time of interest  
 $\Delta t$  = the time window  
 $V_o$  = the nominal voltage (here 0.03 volts)  
 $V_k$  = the stored voltage at the time index  $k$

Note that the equation processes information over a previous time period indicated by the window width  $\Delta t$ . To convert this to a diagnostic, the equation for CumDev was graphed with



respect to time such that the rate of increase in the CumDev represents the degree of activity from the PM sensor. The diagnostic of eq. (1) was computed for Ch4-Probe 405 from the time trace shown in Figure 5-2. The feature of interest for the diagnostic is the slope of this curve, or the rate of climb in absolute deviation with respect to time, as shown in Figure 5-18. The slope is seen to have a value of 125.7 volts deviation per millisecond, as derived from eq. (2).

$$M = \frac{CumDev_t}{t - t_o} = \frac{\sum_{k=t-\Delta t}^t [V_k - V_o]}{t - t_o} \quad (2)$$

When this same diagnostic was applied to the pre-DPF sensor and both sensors plotted on the same graph, it was readily apparent that the two sensors can be differentiated with a degree that could be traced over time. Also, although only approximately 4 sec worth of data is shown, it is clear that the longer the integration time, the larger the differences between the two results. Linear regression provided the slope of the curve in Figure 18, with the dashed blue line representing this fit curve as the slope or rate of increase in the deviation over time.

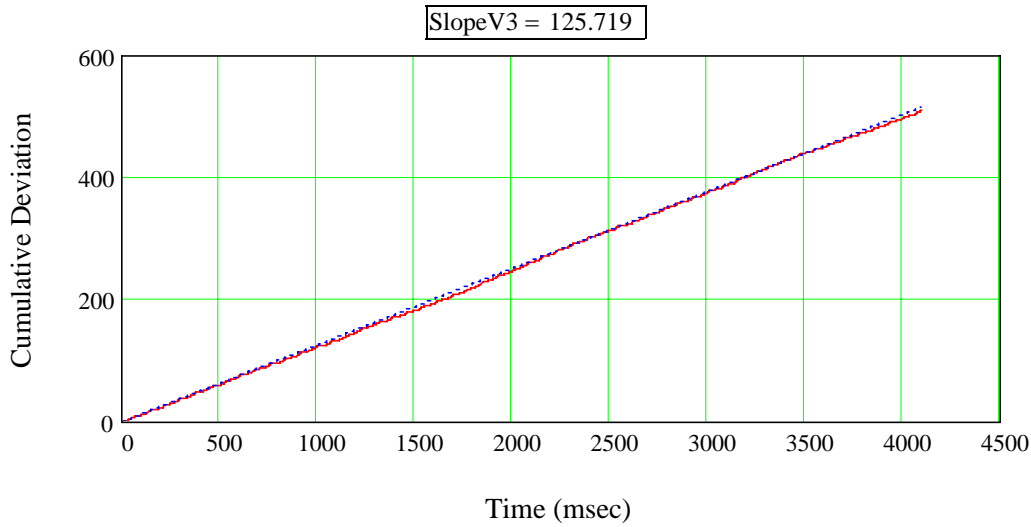


**Figure 5-18. Cumulative Deviation vs. time for the post-DPF sensor—900 holes, Ch3**

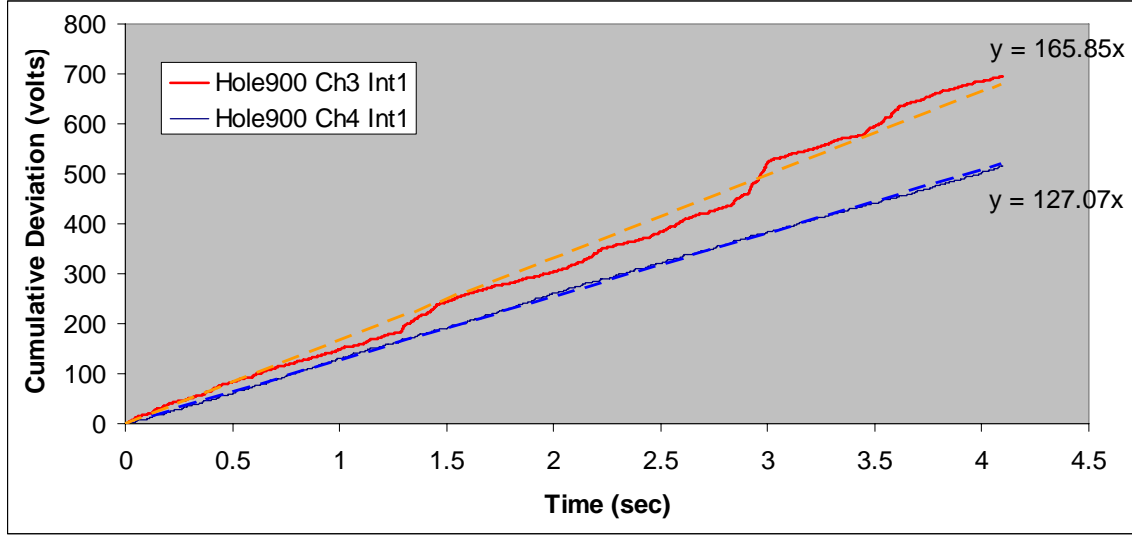


**Figure 5-19. Comparison of Cumulative Deviation for the pre-DPF sensor (red) and the post-DPF sensor (blue)**

To create a diagnostic, the slope  $M$  in eq. (2) can be tracked on a running basis. It is recommended that no less than 2 sec and perhaps at least 4 sec are required to be sure the full cycling of events for the sensor is captured. Even at steady state, seen in the graph above, at 1 sec it would be difficult to differentiate these two trends (red vs. blue). It is interesting to point out that the post-DPF sensor (blue) has a rather well-behaved curve that tracks very closely with the linear regression line, while in contrast the pre-DPF sensor has not only a steeper slope (representing more activity), but also the curve is more erratic with occasional jumps, as seen around 3 sec in the above graph.

To detect DPF failure, a quantitative determination of when the behavior of the post-DPF sensor approached that of the pre-DPF sensor is needed to indicate that the DPF is not functioning. In an OBD context, the sensor system would need to only identify when the post-DPF sensor was behaving sufficiently similar to the pre-DPF sensor. Such a diagnostic might be constructed from the ratio of the slope,  $M$ , of the CumDev vs. time for the post-DPF sensor as a ratio fraction of the pre-DPF sensor according to

$$R_{CumDev} = \frac{M_{post-DPF}}{M_{pre-DPF}} = \frac{CumDev_{post-DPF}}{CumDev_{pre-DPF}} \quad (3)$$

where the appropriate time window,  $t - t_0$ , would be determined from calibration but is recommended to be at least 4 sec.

The OBD algorithm would then signal a failure when the ratio,  $R_{CumDev}$ , of eq. (3) exceeded a pre-set threshold which would be determined by the OEM at calibration according to

$$AlarmState = if(R_{CumDev} > R_{lim}) \quad (4)$$

It should be pointed out that due to the nature of the “activity” discussed earlier, a non-unity power of the deviation of eq. (2) may also make sense. In other words, to amplify the importance of higher deviation values over those of the smaller—and thus provide a larger gap between pre-DPF and post-DPF, the absolute value in eq. (2) could be raised to any power,

such as 2 or 3. When raised to the second power, this becomes similar to an RMS calculation, without taking the square root and being sure to use the deviation from the nominal value.

**Method B: Frequency-Based Signal Processing—Cumulative Spectral Energy**—In the second method, the frequency-based signal is the basis for a DPF failure detection algorithm. As stated earlier, a distinguishably different sensor diagnostic for the post-DPF location under normal conditions needs to be identified and then this diagnostic needs to be tracked. If degradation of the DPF occurs, the change in the post-DPF signal can be then identified and compared to the pre-DPF signal. If these signals are becoming similar then that is a verifiable indication of DPF failure of some significant degree.

This method was inspired by Figure 5-19 and in particular by Figure 5-20, where it can readily be seen that the pre-DPF sensor signature can be easily differentiated from the post-DPF sensor signature. This diagnostic was defined by:

$$SE = \sum_{j=1}^{n \max} (Amp_j)^2, \quad (5)$$

which computes the “Spectral Energy” (SE) as the sum of the square of the amplitudes (Amp) for each individual frequency in the spectrum up to the cut-off frequency defined as nmax.

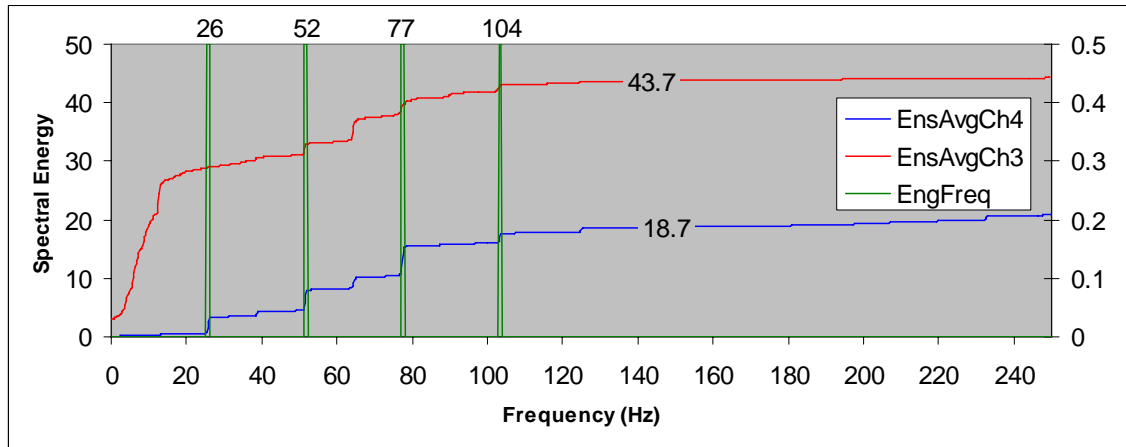


**Figure 5-20. Spectral energy for pre-DPF and post-DPF spectra of the ensemble averages**

One benefit of this method is the inclusion of the energy associated with the ECF harmonics. This energy is much less sensitive to signal-to-noise issues and furthermore does not require the algorithm to identify the specific engine frequencies. Additionally, if filtering of the higher frequencies was desired, the summation is simply terminated at whatever cut-off frequency is desired. For example, 2.9x ECF may be a very good cut-off frequency to allow all the primary activity to be captured while minimizing the risk of having high-frequency “noise” events throw off the cumulative sum unnecessarily. In this case, the pre-DPF sensor has a cumulative spectral energy of 43.7 while the post-DPF sensor has a cumulative spectral energy of 18.7.

As indicated above, a simple ratio of the post-DPF cumulative spectral energy to that of the pre-DPF is sufficient, such as

$$R_{SpecEng} = \frac{SE_{post-DPF}}{SE_{pre-DPF}} \quad (6)$$

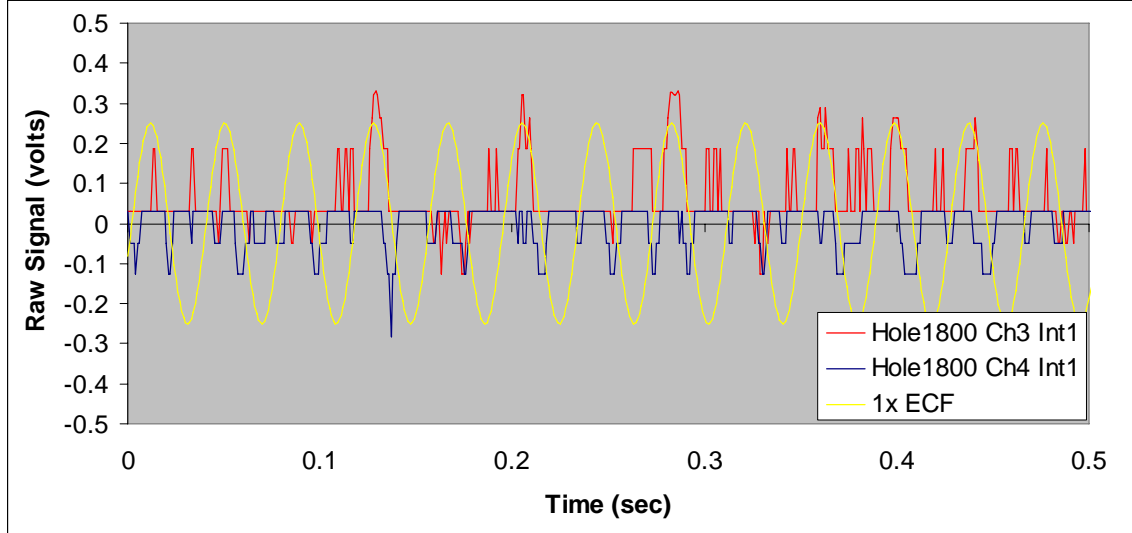
And as mentioned earlier, the alarm state can be triggered according to eq. (4)

**Validation using 1800 hole Failure Tests**—These diagnostics can be applied with success to the other case in this study, such as the data from the 1800 hole failure of the DPF.

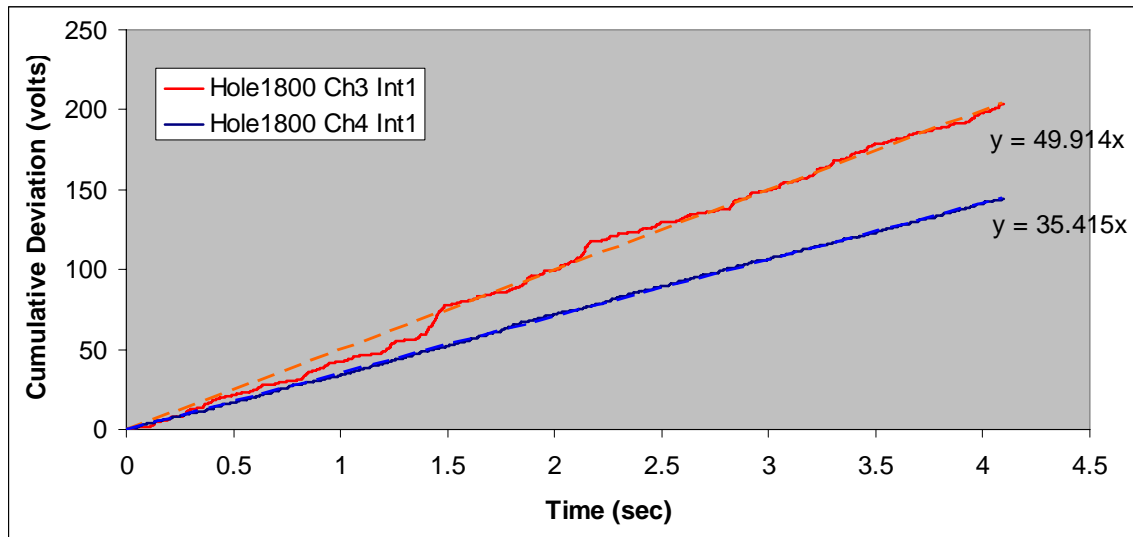
**Time-Based Analysis**—Figure 5-21 and Figure 5-22 show direct comparisons between the pre-DPF and post-DPF sensors in a manner similar to those presented previously for the 900 hole data. A comparison of the time traces, showing both pre-DPF (red-Ch3) and post-DPF (blue-Ch4) is shown in Figure 5-21, along with the 1xECF synthesized function. Again as expected, greater “activity” is seen in the pre-DPF sensor. Interestingly, the post-DPF sensor exhibits only negative deviations. The 1xECF synthesized function (yellow) has a strong overlap with the peaks of the pre-DPF signal (red).

Figure 5-22 shows the direct comparison of the Cumulative Deviation and the computed slopes: 49.914 for Pre-DPF Ch3 and 35.41 for post-DPF Ch4. The post-DPF slope (blue) is smooth while the pre-DPF signal (red) is more chaotic in nature, which is similar to what has been seen previously.

From these two figures, the post-DPF sensor signal is distinguishable from the pre-DPF sensor signal and the slope of the Cumulative Deviation can be used to provide a quantitative determination of the difference between the pre- and post-DPF signals.



**Figure 5-21. For 1800 hole case: time trace of upstream (Ch3 blue) and downstream (Ch4 orange) with synthesized function (yellow)**



**Figure 5-22. For 1800 hole case: Cumulative Deviation pre-DPF slope (red/orange 49.9) is differentiable from post-DPF slope (blue 35.4)**

**Frequency-Based Analysis**—For the spectral analysis, ensemble averaging was employed to see what effect it would have on the diagnostic. If the 4-sec intervals have slightly different spectra, ensemble averaging would help to define a “characteristic” spectra while minimizing outliers. In this case, two back-to-back intervals (Intv2 and intv3) would show essentially the same “characteristic” spectra as the individuals.

Figure 5-23 displays the ensemble averaged spectra superimposed on two individual intervals for the post-DPF sensor, while Figure 5-24 shows the same for the pre-DPF signals.

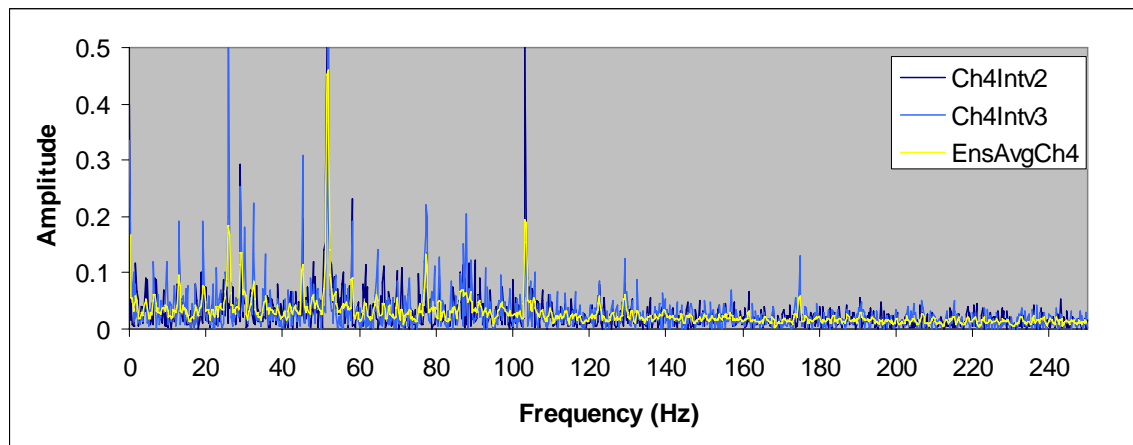


**Figure 5-23. Frequency spectrum for two intervals of the post-DPF sensor trace, each 4 sec**

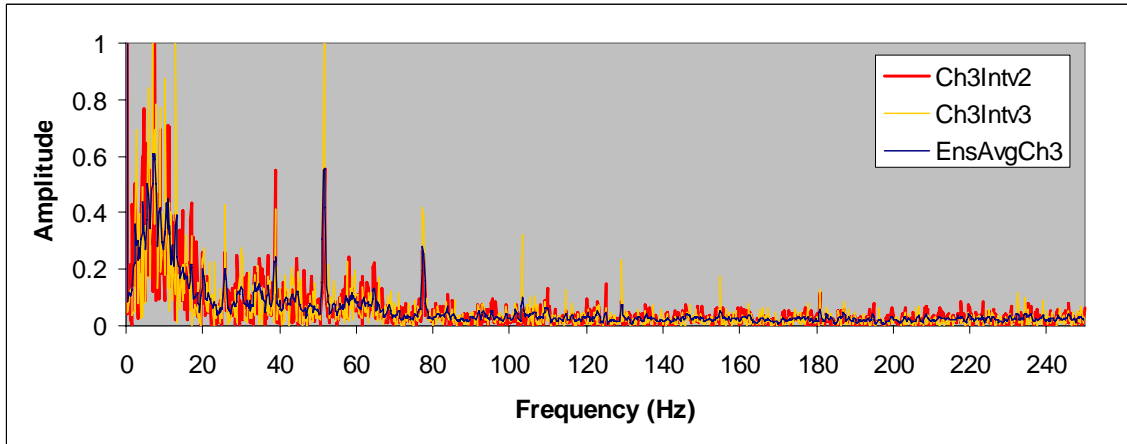


**Figure 5-24. Frequency spectrum for two intervals of the pre-DPF sensor trace, each 4 sec**

Figure 5-25 shows the direct comparison of the ensemble-averaged pre-DPF and post-DPF spectra on the same graph. The consistency with Figure 5-16 can be seen, where both show that the pre-DPF signal has a large amplitude band concentrated below 1xECF. Figure 5-26 shows the cumulative spectral energy, again showing the clear distinction between the pre-DPF (red), which reaches a maximum value of 12.7, having broadband characteristics below 1xECF, and the post-DPF (blue), which reaches a maximum value of 1.7 and has mostly stair-case steps.

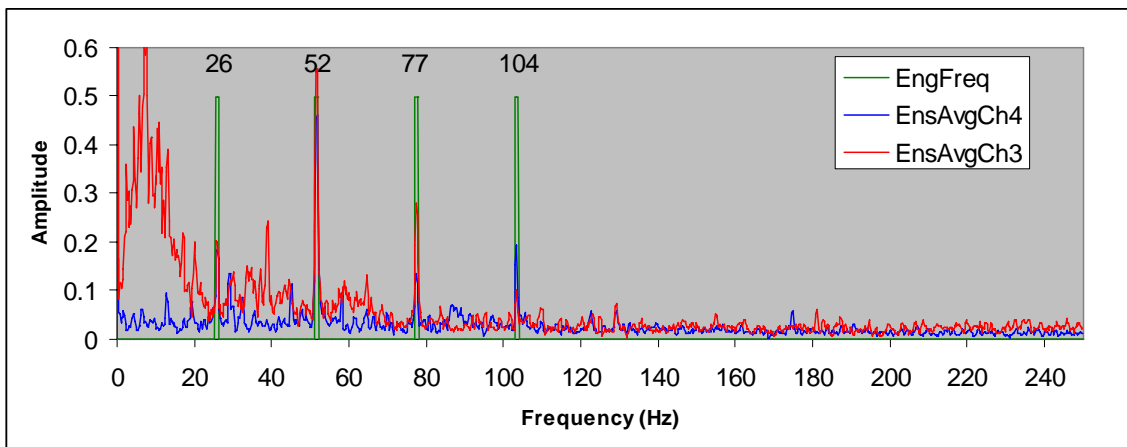


**Figure 5-25. Direct comparison of ensemble-averaged post-DPF (blue) and pre-DPF (red) spectra with synthesized ECF function (green spikes)**

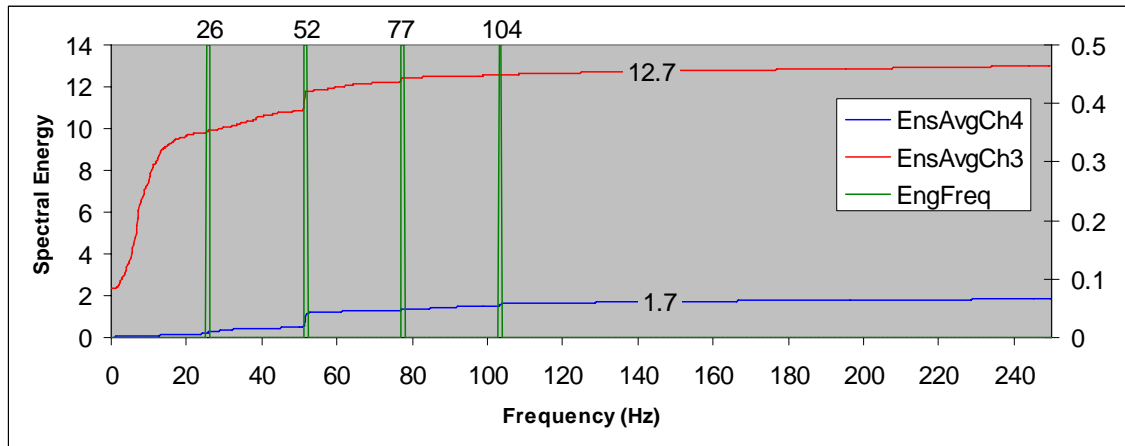


**Figure 5-26. Direct comparison ensemble-averaged post-DPF (blue), pre-DPF (red), and synthesized ECF (green) spectral energy**

**Initial engine testing**—The first engine used was a Deere engine, for which most of the data were obtained. However, as can be seen in Figure 5-27, all the PM sensors are downstream of the DPF, with no pre-DPF sensor online during these tests.

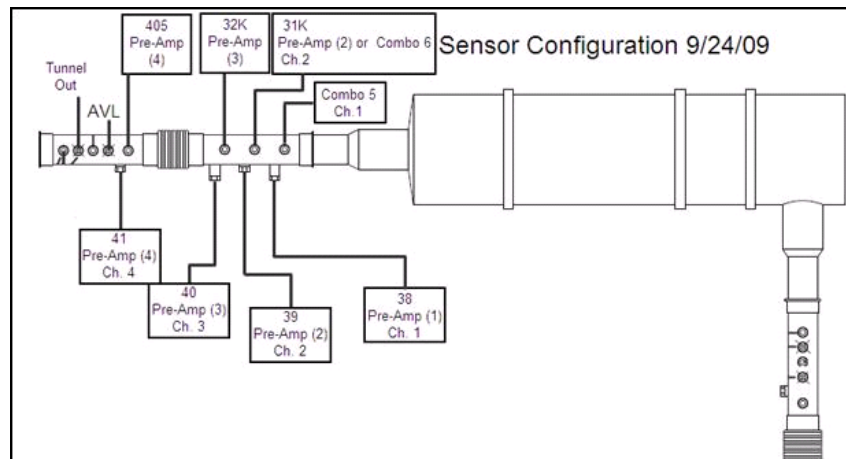


**Figure 5-27. Sensor configuration—Deere Engine 9/24/09 (only post-DPF sensors shown)**

Looking at the time trace of sensor #40 for the operating condition of 1400 RPM and 350 Nm, as shown in Figure 5-28., the characteristic of the PM sensor signal (red) showing its once-per-engine-cycle peaks can be seen. These peaks line up fairly consistently with the synthesized signal (blue).

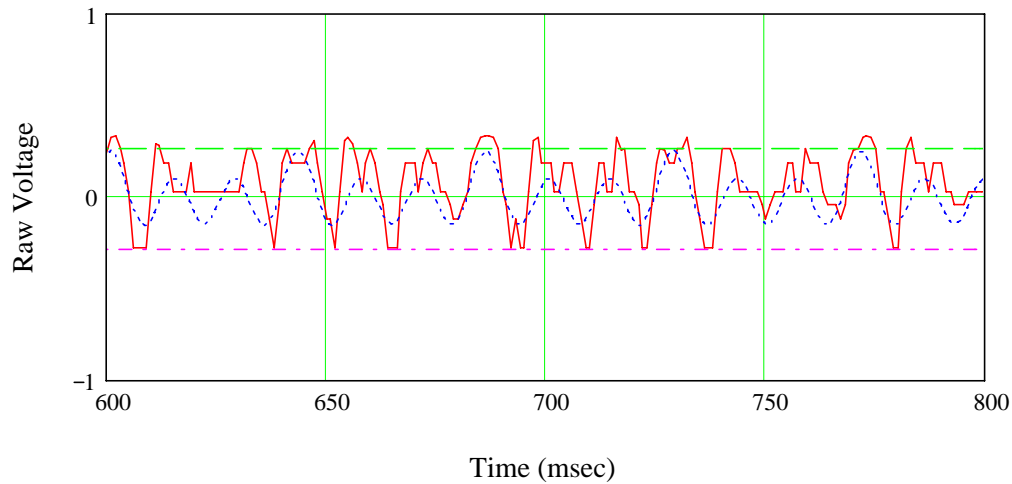


**Figure 5-28. Time trace of sensor #40, for 300 hole DPF failure test**

In Figure 5-28 through Figure 5-32, many of the same or similar characteristics for the Deere engine are seen as was for the Isuzu engine. For example, Figure 5-28 shows the positive/negative oscillations that have a domain positive pulse on the 1x ECF intervals. Here the crests are smoother and broader than on the Isuzu engine. From Figure 5-30, the Cumulative Deviation is seen to have a smooth and steady growth curve, characteristic of the post-DPF signals seen in the Isuzu engine, with a well-defined slope. This slope, 134.43 volts per second, is higher than those slopes seen in the Isuzu engine, despite the fact that the Isuzu cases had more holes drilled in the DPF; this means that the different operation of each engine may produce different soot/charge characteristics.

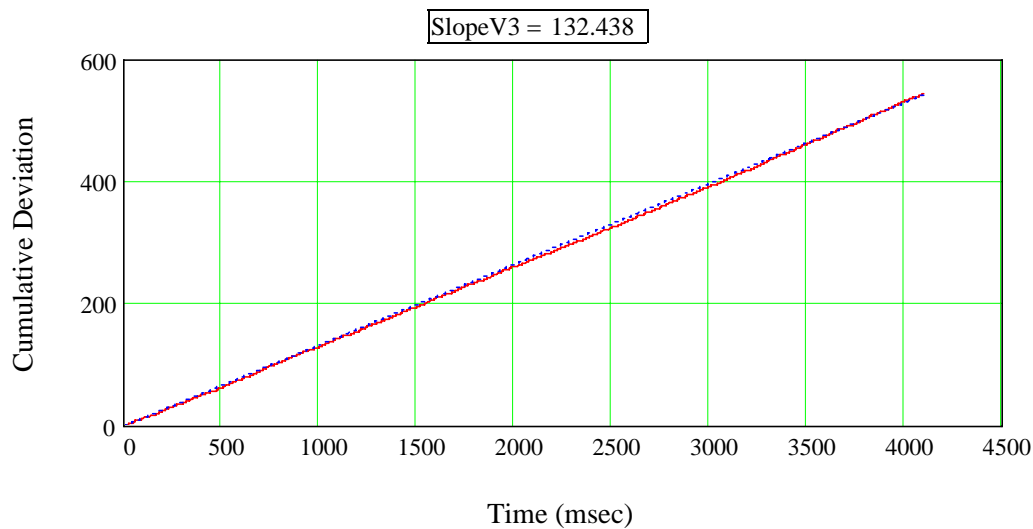


**Figure 5-29. Cumulative deviation showing slope of 132.4 volts per second for sensor #40, for 300 hole DPF failure test**



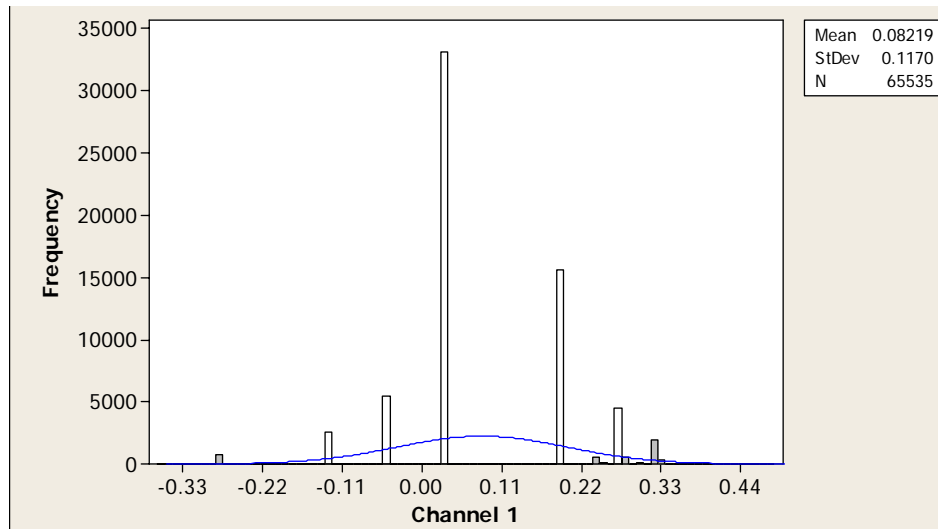


**Figure 5-30. Probability distribution for time trace, sensor #40**

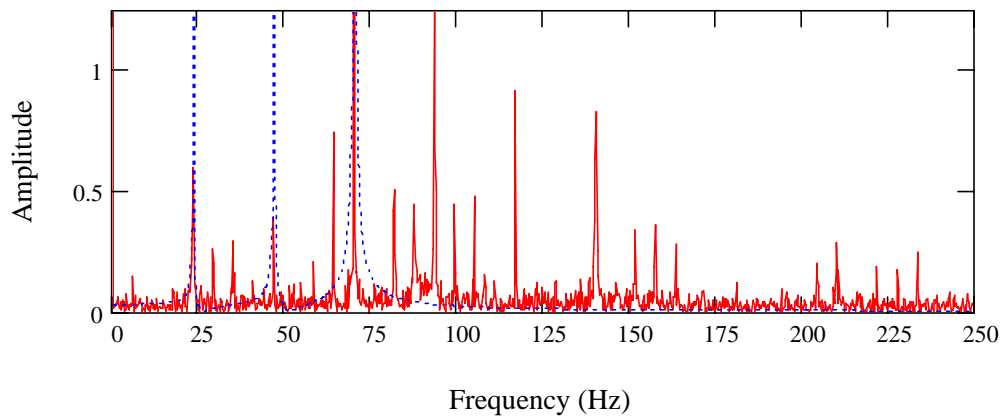


**Figure 5-31. Spectral distribution showing lowest frequency harmonics at 1x, 2x, 3x ECF for sensor #40 for 300 hole DPF failure test**

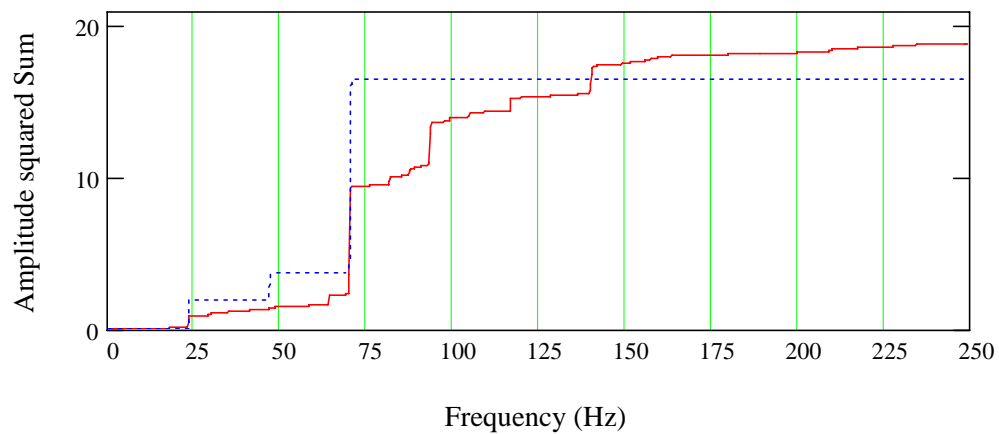


**Figure 5-32. Spectral energy distribution: strong staircase steps evident at 1x, 3x, 4x, 5x, 6x ECF**

From Figure 5-30, it is seen that even though the time trace has a smoother appearance than Figure 5-2; for example, it also has the discrete voltage characteristic similar to the histogram of Figure 5-3.

From Figure 5-31, the spectral distribution again shows the Nx ECF, with a particularly high amplitude harmonics evident at 3x, and 4x ECF, which is also evident in Figure 5-32.

Since not all of the other cases for the Deere engine were analyzed, it is recommended that these cases also be completed to verify the different analysis methods and ultimately select which method might be preferable.

**Correlations to AVL PM Mass**—One objective of this program was to determine if the absolute PM sensor signal can be correlated to a PM mass using a suitable measuring device such as the AVL micro-soot meter. Some success in this area has been reported for the Deere engine, however when the engine was changed to the Isuzu, the relationship between PM charge and PM mass appears to have changed sufficiently to require a new calibration for the Isuzu engine. This indicates that the PM charge to PM mass relationship is engine dependent and underscores the recommendation to move away from absolute/single-sensor correlations to relative/dual-sensor correlations, which may be less sensitive to these engine-to-engine, and potentially fuel-to-fuel, effects. The reason for this is that the pre-DPF sensor identifies the base level and the post-DPF sensor identifies the effects the DPF has on the PM level and presumably a monotonic relationship with the effects on the PM sensor signal. In this sense, the pre-DPF sensor represents a “floating reference.” Consequently, future testing should include PM mass, PM charge, and PM sensor measurements both upstream and downstream of the DPF.

## References and Notes

- <sup>1</sup> Kittelson, D. B., Kadue, P. A., Scherrer, H. C. and Lovrien, R., 1988. *Characterization of Diesel Particles in the Atmosphere*, Final Report, Coordinating Research Council.
- <sup>2</sup> Jung, Heejung and David Kittelson, 2005. Measurement of electrical charge on diesel particles, *Aerosol Science and Technology*, 39: 1129–1135.
- <sup>3</sup> Kittelson, D.B., Collings, N., 1987. Origin of the Response of Electrostatic Particle Probes, SAE 870476.
- <sup>4</sup> US patent 4316360, Apparatus for recycling collected exhaust particles, Liu, Benjamin Y. H. (North Oaks, MN); Kittelson, David B. (Minneapolis, MN); Dolan, Daniel F. (St. Anthony, MN); Pui, David Y. H. (Minneapolis, MN); 1979.
- <sup>5</sup> Ayala, A., B. Olson, B. Cantrell, M. Drayton, and N. Barsic, 2003. Estimation of diffusion losses when sampling diesel aerosol: A quality assurance measure, SAE Technical Paper Series, 2003-01-1896, Warrendale, PA.
- <sup>6</sup> Kittelson, D. B., W.F. Watts, & J.P. Johnson, 2006. On-road and laboratory evaluation of combustion aerosols. Part 1: Summary of diesel engine results, *J. Aerosol Sci.*, 37(8): 913-930.
- <sup>7</sup> Kittelson, D. B., W. F. Watts, J. P. Johnson, J. Schauer, D. R. Lawson, 2006. On-road and laboratory evaluation of combustion aerosols. Part 2: Summary of spark ignition engine results, *J. Aerosol Sci.*, 37(8): 931-949.
- <sup>4</sup> Abdul-Khalek, I., D.B. Kittelson, & F. Brear, 1999. The influence of dilution conditions on diesel exhaust particle size distribution measurements, SAE Technical Paper Series, 1999-01-1142, Warrendale, PA.
- <sup>9</sup> Kittelson, D., W. Watts, & J. Johnson. (2002). Diesel Aerosol Sampling Methodology, CRC E-43 Final Report, pp. 181, NTIS Accession No. PB2003-102418I, available from CRC, Alpharetta, GA. Available at <http://www.crao.com/reports/recentstudies00-02/E-43%20Final%20Report.pdf>.
- <sup>10</sup> National Institute for Occupational Health and Safety (NIOSH) data are available elsewhere <http://www.me.umn.edu/centers/cdr/reports/nioshrealtime.pdf>.
- <sup>11</sup> Wang, X.; Grose, M.; Caldow, R.; Swanson, J.; Watts, W.; Kittelson, D., 2009. Improvement of Engine Exhaust Particle Sizer spectrometer for engine emissions measurement, 28<sup>th</sup> AAAR Conference, Oct 26–30, Minneapolis, Minnesota.
- <sup>12</sup> Wang, X.; Grose, M.; Caldow, R.; Swanson, J.; Watts, W.; Kittelson, D., 2009. Improvement of Engine Exhaust Particle Sizer spectrometer for engine emissions measurement, 28<sup>th</sup> AAAR Conference, Oct 26–30, Minneapolis, Minnesota.
- <sup>13</sup> Park, Kihong, et al., 2003. Relationship between particle mass and mobility for diesel exhaust particles, *Environmental Science and Technology* 37.3: 577-83.
- <sup>14</sup> Graphic taken from Donaldson literature found at [www.donaldson.com/en/exhaust/support/datalibrary/033834.pdf](http://www.donaldson.com/en/exhaust/support/datalibrary/033834.pdf) and modified to indicate failure mode.